CYRIC

ANNUAL REPORT

2010 - 2011

(January 2010 - December 2011)

CYCLOTRON AND RADIOISOTOPE CENTER
TOHOKU UNIVERSITY

CYRIC

ANNUAL REPORT

2010 - 2011

(January 2010 - December 2011)

CYCLOTRON AND RADIOISOTOPE CENTER
TOHOKU UNIVERSITY
http://www.cyric.tohoku.ac.jp/

PREFACE

March 11 2011 a massive earthquake, later named the Great East Japan Earthquake, occurred off the Pacific Coast of Tohoku Region and enormous Tsunami attacked the seashores and caused the indescribable disaster. The Cyclotron and Radioisotope Center (CYRIC) was also hit by the earthquake and got serious damage on two cyclotrons and facilities. Since then, our efforts have been made towards fixing damaged equipment and now we can see a bright goal after struggling for more than one-year restoration. For this reason the present thirty-first CYRIC Annual Report is published as a double issue of 2010/2011.

Research at CYRIC was carried out in the fields of nuclear physics, nuclear chemistry, material sciences, nuclear medicine using PET (oncology, brain study, pharmacology), radiopharmaceutical chemistry, health physics, nuclear instrumentation, nuclear medical engineering (diagnosis and therapy technology), nuclear engineering and elemental analysis using PIXE.

The present earthquake with magnitude 9 has given the critical damages to the two Sendai Cyclotrons and related equipment. The most serious one is the damage of main props supporting the K=110 MeV cyclotron, which has a weight of 250 ton. This causes a serious slanting of the horizontal plane of the cyclotron. Furthermore, the buildings of the cyclotron vault and five target rooms had damages for floors and walls. It needs the re-alignment of the whole part of the beam transport lines as well as cyclotron itself. The followings are the typical lists of heavily damaged equipment;

1) All of the heavy concrete shield doors at the building wall were broken and ran off the rails.
2) Over 25 beam duct connections were broken.
3) The 12 MeV small cyclotron for radioisotope production went a drift 3 meter from fixed position.
4) Many vacuum pumps, chambers, small magnets for beam transport and electric racks were tumbles down. The master plan for recovery has been discussed according to the 1st supplemental budget, and the first operation for recovering will be undertaken from the beginning of July 2011. All of the cyclotron staff hope that they will be come around on the beginning of autumn 2012.

The damage of main props supporting the K=110 MeV cyclotron.

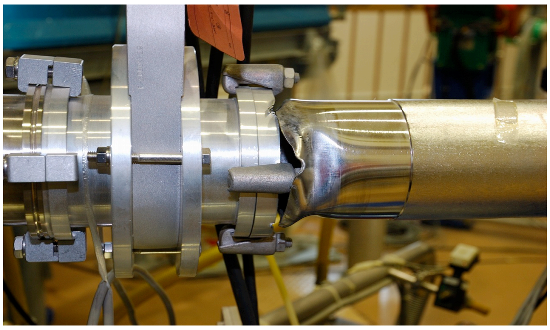

A typical case of broken vacuum ducts of beam lines.

The experimental project to search for the permanent electric dipole moment (EDM) of the electron with the radioactive atom such as the Francium (Fr) is going on to the next phase to install the new beam line to transport the Fr from the TR5 to the TOF, where the EDM will be measured. The newly developed thermal ionizer achieved the 10^6 Fr^+/s production yield with the nuclear fusion reaction using the 100 MeV ^{18}O beam and ^{197}Au target, and high extraction efficiency with 35 %. The double MOT (Magneto-Optical Trap) was developed to accumulate the Fr atoms in the vacuum cell using laser cooling and trapping technique, and the long coherence time sufficient to measure the EDM was realized. All the components for the measurement of the Fr EDM will be ready in 2012.

In the research program on proton therapy, combined treatment between proton irradiation and a platinum-based chemotherapeutic agent has been studied. One of the important considerations in obtaining the optimal enhancement in the combined treatment is the concentration of the agent in the tumor. Therefore, particle-induced X-ray emission (PIXE) analysis has been employed for elemental analysis of the treated tumor. An enhanced therapeutic effect as well as spatial distribution of platinum in the tumor samples were successfully evaluated in NFSa fibrosarcoma tumors in mice. These studies have been published in international journals.

Routine production of PET probes was resumed May 2010 after a nearly one-year break for the restoration work of the cyclotron building. Up to March 11 productions of [^{18}F]FDG (12 preparations), [^{18}F]FRP-170 (1), [^{18}F]FACT (5), [^{11}C]doxepin (28), [^{11}C]raclopride (10), [^{11}C]donepezil (9), [^{11}C]BF-227 (35) and [^{15}O]water (13) for clinical PET studies were regularly carried out. As a heavy shielding door to the HM12 cyclotron room broke down by the earthquake, they could not be continued any more although any practical damages were not found on the all automated modules. However, thanks to kind support from many research PET centers in japan and even from abroad, we could succeed our research and development of new PET probes and synthesis methods. Especially we would like to thank Molecular Imaging Center of National Institute of Radiological Sciences (Director Dr. Yasuhisa Fujibayashi), RIKEN Center for Molecular Imaging Science (Director Dr. Yasuyoshi Watanabe) and Positron Medical Center of Tokyo Metropolitan Institute of Gerontology (Director Dr. Kiichi Ishiwata) for providing cyclotron beam time and experimental spaces.

In 2010, Molecular Imaging Educational Program of Tohoku University was successful. And this year was very fruitful in terms of research. Nearly 20 papers were published from biomedical research activities. Some of them were really important achievements in the field of neurology and neuroscience. Our original tracer ^{11}C-BF-227 was identified to be able to visualize not only beta-amyloid deposition in Alzheimer's disease patients but also prion-amyloid protein deposition and alpha-synuclein deposition in the patients with multiple system atrophy. Finally, we received an announcement that our request for getting a new scanner was accepted by the government.

We succeeded in getting a governmental support for installing a new PET/CT scanner. The new scanner, eminence STARGATE (Shimadzu Co.,Ltd.) was installed in the beginning of 2001 on the first floor of the life-science research building ("Kenkyu-To") instead of the third floor for fear of the predicted "Miyagi Off-shore Earthquake". In reality, however, much bigger "Great East Japan Earthquake" hit our center shortly after the completion of PET/CT scanner installation. Luckily, the confirmed damages to our older PET and new PET/CT scanners were minimal. Suddenly, our 2011 became the year of repairment and recovery, with just a few numbers of PET examinations using ^{18}F-FDG vials delivered by Nihon Medi-Physics Co.,Ltd.

The research program on PIXE analysis has been carried out by using electrostatic accelerator (4.5 MV Dynamitron) at the Fast Neutron Laboratory, Graduate School of Engineering, Tohoku University, under the scientific tip up between CYRIC and FNL. Research studies using submilli-PIXE camera, microbeam analysis system, and Micron-CT had been carried out until the Great East Japan Earthquake. A total of 1200 hours of beam-time was served to this program without serious problems until the earthquake. The Dynamitron accelerator, beam line and other sub-system suffered damages by the earthquake. Almost all of the damages except for microbeam analysis system were temporarily recovered and the research program on PIXE analysis was restarted in

September 2011. Full-scale restoration work will be started from April 2012. A total of 200 hours of beam-time was served to this program in 2011.

The beginners training for safe handling of radiation and radioisotopes was carried out as usual in 2010. A total of 974 staffs and students of Tohoku University took three courses: 1) Radioisotopes and radiation generators (491 trainees), 2) X-ray machines and electron microscope (389), and 3) Synchrotron Radiation (94). The number of trainees in this year was almost the same as that of the previous year (1028). The English classes for each course were practiced for 92 foreign students and scientists. In 2011, the period of the training was restricted under the influence of the Great East Japan Earthquake, and the number of trainees decreased (701): 1) Radioisotopes and radiation generators (319), 2) X-ray machines and electron microscope (334), and 3) Synchrotron Radiation (48). The English classes for each course were practiced for 53 foreign students and scientists.

A novel partitioning process for the treatment of HLLW has been studied experimentally based on column separation technique using macroporous silica-based adsorbents. These adsorbents were prepared by impregnating Calix[4]arene-R14, DtBuCH18C6, MOTDGA/TOA and TODGA into the styrene-divinylbenzene copolymer which was immobilized in porous silica particles (SiO2-P). This proposed partitioning process consists of (1) Cs and Rb which showed high selective adsorption onto Calix[4]arene-R14 molecular are removed by the first separation column packed with Calix[4]arene-R14/SiO2-P adsorbent; (2) Sr and Ba are eluted out by water from the second separation column packed with DtBuCH18C6/SiO2-P adsorbent; (3) Pd is strongly adsorbed by MOTDGA-TOA/SiO2-P adsorbent and eluted off by 0.2 M Tu-0.1 M HNO3 solution from the third separation column packed efficiently; (4) Ru, Rh and Mo can be separated by the fourth separation column packed with TODGA/SiO2-P adsorbent because the no or weak adsorption affinity of them to adsorbent. The experimental results indicated that this process is essentially feasible to separate the long-life and significant fission product elements from HLLW.

Development of semiconductor gamma-ray detectors using thallium bromide (TlBr) crystals was carried out at the Rokkasho branch of CYRIC, which was less affected by the Great East Japan Earthquake. In order to realize large volume gamma-ray detectors, capacitive Frisch grid detectors were fabricated from thick (4.4 mm) TlBr crystals. The thick TlBr detectors exhibited excellent energy resolutions for gamma-rays at room temperature. Digital signal processing techniques were developed for TlBr detectors.

Improvement of detector performance was achieved by applying the digital method to planar TlBr detectors.

The huge Tsunami after the Great East Japan Earthquake attacked Fukushima first nuclear power plant. As the result, 4 nuclear reactors hydrogen-exploded and huge amount of radioactivity was scattered on the eastern Japan. Tohoku University established a task force for the Fukushima first nuclear power plant accidents at our center March 15, 2011 and began the examination of radioactive contamination. The values of space dose rate at several points in Miyagi prefecture are shown in the home page of Tohoku University from March 18, 2011. The space dose rate at Sendai is now 0.07 μSv/h. In response to the requests of Miyagi prefecture, 12 cities and 5 towns, we examined the radioactive contamination in tap water, milk, vegetables, mushrooms and sea water on the basis of nuclide analysis by HPGe detectors. The radioisotopes detected in these samples were ^{131}I, ^{132}I, ^{132}Te, ^{134}Cs and ^{137}Cs. The radioactivity levels of these samples were much lower than the regulation values shown by Japanese government. Moreover, we carried out the decontamination of schoolyards of two Kindergartens and Elementary schools at the south part of Miyagi prefecture.

The schoolyard decontaminated of Kohya Elementary school in Marumori Town.
The space dose rate reduced from 1mSv/h to 0.2 mSv/h

We are most grateful to Tohoku University and to the Ministry of Education, Sports, Culture, Science and Technology for continuous support.

January 2012
Keizo ISHII
Director
Cyclotron and Radioisotope Center, Tohoku University

EDITORS:

Keizo ISHII
Ren IWATA
Hiromichi YAMAZAKI
Yasuhiro SAKEMI
Tsutomu SHINOZUKA
Manabu TASHIRO

WORD PROCESSED BY

Yuko YAMASHITA

CONTENTS

I. NUCLEAR PHYSICS

I. 1. Development of the Laser Cooled Atom Trap for the Parity Non Conservation of Fr ········ *1*
Sakemi Y., Oikawa A., Harada K., Kawamura H., Itoh H., Yoshida H., Hayamizu T., Sato T., Kato T., Ezure S., and Nataraj H.S.

I. 2. Development of High Quality Francium Ion Beam to Search for the Permanent Electron Electric Dipole Moment ········ *4*
Yoshida H., Hayamizu T., Liu S., Oikawa A., Saito M., Aoki T., Ezure S., Furukawa T., Harada K., Hatakeyama A., Hatanaka K., Imai K., Itoh M., Kawamura H., Kato T., Murakami T., Nataraj S. H., Sato T., Shimizu Y., Uchida M., Wakasa T., and Sakemi Y.

I. 3. Development of a Neutralizer for the Search of an Electron EDM ········ *10*
Kawamura H., Aoki T., Ezure S., Furukawa T., Harada K., Hatakeyama A., Hatanaka K., Hayamizu T., Imai K., Itoh M., Kato T., Liu S., Murakami T., Nataraj H. S., Oikawa A., Saito M., Sato T., Shimizu Y., Uchida M., Wakasa T., Yoshida H., and Sakemi Y.

I. 4. Toward Magneto-Optical Trap of Fr Atoms for EDM Search ········ *14*
Harada K., Aoki T., Oikawa A., Hayamizu T., Ezure S., Itoh M., Yoshida H., Kawamura H., Sato T., Kato T., Nataraj H., and Sakemi Y.

I. 5. Development of a New Rubidium Ion Source for the Study of a Francium Neutralizer ········ *18*
Sato T., Ezure S., Furukawa T., Harada K., Hayamizu H., Itoh M., Kato T., Kawamura H., Liu S., Nataraj H. S., Oikawa A., Saito M., Yoshida H., and Sakemi Y.

I. 6. Upgrade of Thermal Ionizer for the Production of High Intensity Francium Beam ········ *22*
Liu S., Yoshida H., Hayamizu T., Saito M., and Sakemi Y.

I. 7. Search for the Bandhead of the Hoyle State + α Cluster Structure in ^{16}O via the ^{12}C(^{16}O,^{16}O*[α+X])^{12}C Reaction ········ *26*
Itoh M., Harada K., Hayamizu T., Kawamura K., Liu S., Nataraj H., Oikawa A., Saito M., Sakemi Y., Sato T., and Yoshida H.

II. NUCLEAR INSTRUMENTATION

II. 1. Development of a Sextupole Ion Beam Guide for Improvement of the RF-IGISOL ········ *29*
Shimada K., Takahashi M., Ueno H., Izumi S., Wakui T., and Shinozuka T.

II. 2. New Electron Cyclotron Resonance Ion Source for Heavy-ions ········ *31*
Wakui T., Shinozuka T., Shimada K., Sakemi Y., Itoh M., Yoshida H., Chiba S., Ohmiya Y., Takahashi N., Takahashi K., Yokogawa S., and Suzuki J.

II. 3. **Performance of the High Intensity Fast Neutron Beam Facility** *33*
Yoshida H., Itoh M., and Sakemi Y.

III. NUCLEAR ENGINEERING

III. 1. **Investigation of an Optimum Clustering Condition for TlBr Detectors** *35*
Tada T., Hitomi K., Xu Y., Kim S.-Y., Yamazaki H., and Ishii K.

III. 2. **Measurement of Electron Drift Mobility in TlBr Crystals** *39*
Hitomi K., Tada T., Xu Y., Kim S.-Y., Yamazaki H., and Ishii K.

IV. NUCLEAR MEDICAL ENGINEERING

IV. 1. **Development of Positron Emission Mammography (PEM) for Commercial Use** *43*
Miyake M., Yamamoto S., Itoh M., Itoh S., Sato H., Kumagai K., Tashiro M., and Baba M.

IV. 2. **A Preliminary Study of Proton Therapy Combined with Cisplatin** *46*
Terakawa A., Ishii K., Matsuyama S., Kikuchi Y., Ito Y., Yasunaga S., Tagawa A., Kawamura T., Takahashi Y., Hatori Y., Hamada N., Fujiki K., Miura Y., Yamazaki H., Funaki Y., Itoh N., Wada S., and Sera K.

V. PIXE AND ENVIRONMENTAL ANALYSIS

V. 1. **PIXE Analysis of a Murine Fibrosarcoma Tumor Treated With a Vascular Disrupting Agent AVE8062** *49*
Terakawa A., Ishii K., Matsuyama S., Kikuchi Y., Yasunaga S., Ito Y., Tagawa A., Kawamura T., Takahashi Y., Sugai H., Hamada N., Fujiki K., Hatori E., Yamazaki H., Funaki Y., Furumoto S., Itoh N., and Wada S.

V. 2. **Application of Micro-PIXE Analysis to Investigate Trace Elements in Deciduous Teeth Enamel** *52*
Igari K., Takahashi A., Ando H., Ishii K., Matsuyama S., Kawamura Y., Ohkura S., Hashimoto Y., Fujikawa M., Itou Y., Fujiki K., Hatori Y., Hamada N., and Yamazaki H.

V. 3. **Microbeam Analysis of Individual Particles in Working Environment** *57*
Matsuyama S., Catella G., Ishii K., Terakawa A., Kikuchi Y., Kawamura Y., Ohkura S., Fujikawa M., Hamada N., Fujiki K., Hatori Y., Ito Y., Yamazaki H., Hashimoto Y., Žitnik M., Pelicon P., and Grlj N.

V. 4. **Recent Application of Tohoku Microbeam System** *62*
Matsuyama S., Ishii K., Yamazaki H., Kikuchi Y., Inomata K., Watanabe Y., Ishizaki A., Oyama R., Kawamura Y., Yamaguchi T., Momose G., Nagakura M., Takahashi M., and Kamiya T.

V. 5. **Improvement of The Performance of Tohoku Microbeam System** *68*
Matsuyama S., Ishii K., Tsuboi S., Hashimoto Y., Kawamura Y., Yamanaka K., Watanabe M., Ohkura S., Fujikawa M., Catella G., Fujiki K., Hatori Y., Hamada N., Fujiwara M., Kikuchi Y., and Yamazaki H.

VI. RADIOCHEMISRTY AND NUCLEAR CHEMISTRY

VI. 1. Development of a Simplified MA Separation Process Using Novel R-BTP Adsorbents – III ······ *75*
Usuda S., Kuraoka E., Li Z., Liu R., Xu Y., Kim S.-Y., Wakui Y., Hayashi H., Yamazaki H., and Ishii K.

VI. 2. Study on Selective Separation and Recovery of Cesium and Strontium from High-level Liquid Waste (HLLW) ······ *82*
Kim S.-Y., Wu Y., Tozawa D., Ito T., Y Xu., Hitomi K., Tada T., Yamazaki H., and Ishii K.

VI. 3. Study on Adsorption Behavior of Trivalent Rare Earths onto a Macroporous Silica-Based TODGA Adsorbent from High Level Liquid Waste ······ *88*
Xu Y., Kuraoka E., Usuda S., Kim S. Y., Hitomi K., Tada T., Yamazaki H., and Ishii K.

VII. RADIOPHARMACEUTICAL CHEMISTRY AND BIOLOGY

VII. 1. Microfluidic Radiofluorination Using Electrochemically Concentrated [^{18}F]Fluoride ······ *93*
Wong R., Iwata R., Furumoto S., Saiki H., Ishikawa Y., and Ozeki E.

VIII. NUCLEAR MEDICINE

VIII. 1. PET Imaging in Cardiac Amyloidosis with [^{11}C]BF-227 ······ *97*
Furukawa K., Ikeda S., Okamura M., Tashiro M., Tomita N., Furumoto S., Iwata R., Yanai K., Kudo Y., and Arai H.

VIII. 2. Neural Basis of Pleasant and Unpleasant Emotions Induced by Social Reputation ······ *100*
Ito A., Fujii T., Ueno A., Koseki Y., Tashiro M., and Mori E.

VIII. 3. Simultaneous Measurement of Regional Cerebral Blood Flow Changes Using [^{15}O]H_2O-PET and Functional Near-Infrared Spectroscopy (fNIRS): A Pilot Study ······ *103*
Tashiro M., Hiraoka K., Watanuki S., Ishikawa Y., Miyake M., Masud MM., Ishikawa A., Inoue Y., and Yanai K.

VIII. 4. Donepezil Binding to Acetylcholinesterase and Response to Donepezil Therapy in Parkinson's Disease Dementia: [5-^{11}C-*methoxy*]Donepezil-PET Study ······ *106*
Hiraoka K., Okamura N., Funaki Y., Hayashi A., Tashiro M., Hisanaga K., Fujii T., A Takeda., Yanai K., Iwata R., and Mori E.

VIII. 5. Medical Imaging and Scientific Visualization ······ *110*
Tashiro M., Narashima T., Hiraoka K., Yanai K., Nagami F.

IX. RADIATION PROTECTION AND TRAINING OF SAFETY HANDLING

IX. 1. Beginners Training for Safe Handling of Radiation and Radioisotopes in Tohoku University *115*
Yamazaki H., Baba M., Miyata T., Ohtomo K., Mayama F., and Yuki H.

IX. 2. Radiation Protection and Management *118*
Yuki H., Miyata T., Ohtomo K., Yamazaki H., Baba M., and Nakae H.

X. PUBLICATIONS *121*

XI. MEMBERS OF COMMITTEE *129*

XII. STAFF *135*

I. 1. Development of the Laser Cooled Atom Trap for the Parity Non Conservation of Fr

Sakemi Y., Oikawa A., Harada K., Kawamura H., Itoh H., Yoshida H.,
Hayamizu T., Sato T., Kato T., Ezure S., and Nataraj H.S.

Cyclotron and Radioisotope Center, Tohoku University

The parity non conservation (PNC) of the nuclear beta decay has been investigated extensively and has lead the construction of the framework for the weak interaction with the V-A (Vector – Axial vector) theory. From the microscopic point of view, the beta decay is the transition between the quarks with the different flavors within the same generation, namely 1st generation of the quark family, with the charged current which means the propagation of the charged gauge boson of the weak interaction, $W^{\pm}$ bosons. This process is occurred by the charge exchange reaction, and can be measured with the standard experimental technique. However, on the other hand, the observation of the effects from the neutral current, which is the propagation of the neutral weak boson Z, has been quite difficult due to the fact that there is no flavor and charge changes. Only the high energy electron and neutrino scattering experiments explored the neutral currents precisely thanks to the large contribution from the high momentum transfer (q) compared with the large mass of the weak boson. To understand the structure of the weak interaction more precisely, to search for the phenomena beyond the standard model, and to investigate the parity violating nuclear force in the nucleus, the experiment to detect the PNC in the small momentum transfer region is very important. The PNC for the neutral atom, therefore, is the powerful tool to explore these important topics related with the neutral current, since the flavor of the lepton and quark is not changed in the atom, and it observes the small q.

At the CYRIC, we plan to measure the PNC for the francium, which is the heaviest alkaline atom and radioactive element with the half life of about 3 min. The physics goal is to extract the parity violating nucleon-nucleon interaction to understand the weak interaction in the strongly interacting nuclear medium through the measurement of the anapole moment, which is the parity odd higher order term in the multipole decomposition of the vector potential. The heaviest alkaline element Fr is selected, since the theoretical calculation suggests that the anapole moment is enhanced with the $A^{2/3}$, where the A is the mass number of the atom. Also the new experimental method to measure the anapole moment is now introduced using the laser cooling technique. Up to now, only two measurements for Cs and Tl were done, and their measurement accuracy is limited due to the short interaction and measurement time, because they use the atomic beam. Then, we will measure the anapole moment with the cooled atom ensemble using the laser cooling/trapping technique to realize the long interaction and detection time.

We are now constructing the high intensity Fr ion source, the beam transport system, the neutralizer, and the magneto-optical trap (MOT), which will be utilized commonly to search for the electric dipole moment of Fr. However, the double MOT configuration and high sensitive photon detection are essential especially for the anapole moment measurement to obtain a subtle signal emitted with the de-excitation from the forbidden state where the parity mixed states are degenerated due to the weak interaction and stark shift effect. The developed MOT is shown in the Fig. 1. The first MOT is used for the collection and buffering of the Fr introduced from the neutralizer. The second MOT is used for the measurement with the long interaction and detection time thanks to the high vacuum. These two MOTs are connected with the narrow tube to achieve the high vacuum in the second MOT using the differential pumping. The vacuum level with 10^{-9} Torr and 10^{-11} Torr were realized in the 1st MOT and 2nd MOT respectively. Instead of the Fr atom, which is produced by the nuclear fusion reaction, the stable atom Rb was used to investigate the performance for the atom trapping. We have succeeded in the double MOT to collect, push, and accumulate the Rb for a long time. Then, we measured the life time of the accumulated Rb atoms in the 2nd MOT as shown in the Fig. 2. The horizontal axis shows the measurement time, and the vertical axis shows the number of the Rb atoms in the MOT, which was estimated from the photon intensity measured by the CCD camera. We could observe the two components of the slopes showing the lifetime of the trapping atom. The first component, which shows the short life time with about 10 sec, means that the atoms are lost due to the collisions between trapped atoms. The second component shows the longer life time with about 40 sec, and it can be interpreted that the atoms are lost due to the collisions between the trapped atoms and background gas, which depends on the vacuum level. The development for the high sensitive photon detector is also in progress.

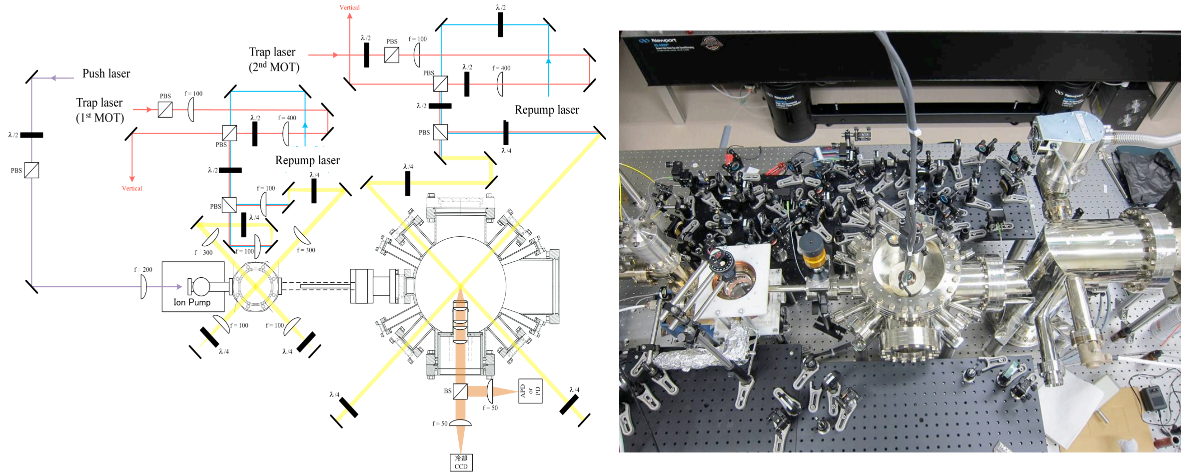

Figure 1. The experimental setup of the double MOT. The left figure shows the configuration of the MOT chambers and laser. The right picture shows the developed experimental apparatus of the double MOT.

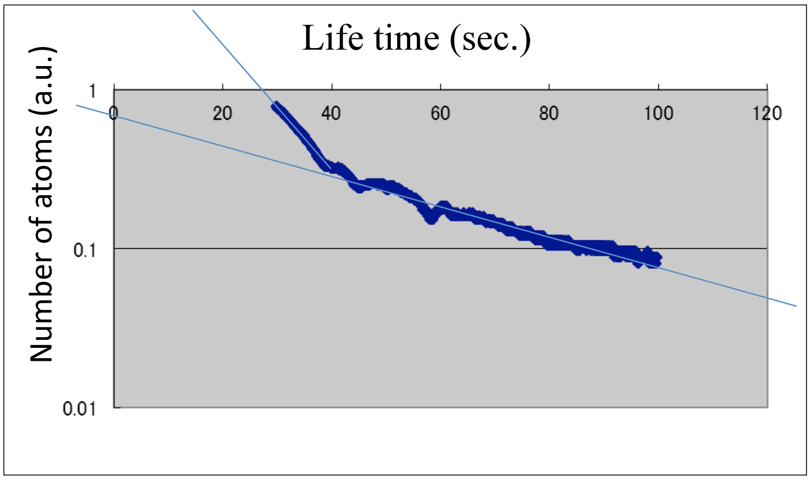

Figure 2. The lifetime of the trapped Rb atom in the 2nd MOT. Two components of the lifetime are observed in the plot.

I. 2. Development of High Quality Francium Ion Beam to Search for the Permanent Electron Electric Dipole Moment

Yoshida H.[1]*, Hayamizu T.*[1]*, Liu S.*[2]*, Oikawa A.*[1]*, Saito M.*[1]*, Aoki T.*[3]*, Ezure S.*[1]*,*
Furukawa T.[4]*, Harada K.*[1]*, Hatakeyama A.*[5]*, Hatanaka K.*[6]*, Imai K.*[7]*,*
Itoh M.[1]*, Kawamura H.*[1]*, Kato T.*[1]*, Murakami T.*[7]*, Nataraj S. H.*[1]*,*
Sato T.[1]*, Shimizu Y.*[8]*, Uchida M.*[9]*, Wakasa T.*[10]*, and Sakemi Y.*[1]

[1]*Cyclotron and Radioisotope Center, Tohoku University*
[2]*Department of Physics, Jilin University*
[3]*Graduate School of Arts and Sciences, University of Tokyo*
[4]*Department of Physics, Tokyo Metropolitan University*
[5]*Department of Applied Physics, Tokyo University of Agriculture and Technology*
[6]*Research Center for Nuclear Physics, Osaka University*
[7]*Department of Physics, Kyoto University*
[8]*Department of Physics, Tohoku University*
[9]*Department of Physics, Tokyo Institute of Technology*
[10]*Department of Physics, Kyusyu University*

Introduction

The non-zero observation of electric dipole moment (EDM) of the elementary particle provides the direct signature of the violation of the time-reversal (T) symmetry. Under the CPT theorem the T-violation means the CP violation. The Standard Model shows that the electron EDM (e-EDM) appeares only in the higher-order diagram with gluon exchange and predicts a quite small value of less than 10^{-38} e cm1), which is many orders of magnitude below the current experimental limit. On the other hand, several theoretical models beyond the Standard Model predict much larger e-EDM values as 10^{-26} ~ 10^{-29} e cm2). This means that e-EDM is a good probe to search for the phenomena beyond the Standard Model.

In paramagnetic atoms an electron EDM results in an atomic EDM enhanced by the factor $\sim Z^3 \alpha^2$ 3), where Z and α are the atomic number and the fine structure constant, respectively , due to the relativistic effects. A heaviest alkali element francium (Fr) has the largest enhancement factor R~895 4). The electron EDM for Fr atom has not yet been measured because Fr is a radioactive element with no stable isotopes, and it is difficult to make a concentrated sample due to a short life time (1~20 min) for the standard experiment.

Then, we are developing a high intensity laser cooled Fr factory at CYRIC, to perform the search for the unstable atom Fr with the online Fr production, cooling and trapping.

Figure 1 shows the overview of the high intensity laser cooled Francium factory. The Fr is produced by a heavy-ion fusion reaction with an oxygen beam and a gold target ($^{18}O+^{197}Au \rightarrow ^{210}Fr+5n$ etc.) with the primary beam energy E~100 MeV just above the coulomb barrier. The feature and details for each apparatus of this factory are reported5,6). In these reports the experiment for Fr production and ion transport system are described.

Experimental Apparatus

For the primary beam of ^{18}O, the new 10 GHz ECR ion source (ECR10) was prepared for higher intensity and heavy nuclide and the beam current of $^{18}O^{5+}$ with 2 electric μA has been achieved. We utilize the beam swinger system to inject oxygen beam into the gold target in Thermal Ionizer downward. The angle of the swinger system is fixed at 45 deg. In the Thermal Ionizer, francium atom produced by fusion reactions are ionized and extracted. To realize more than 10^6 of Fr^+/sec yield, the thermal ionizer was designed to expect over 10% of extraction efficiency and stable heating operation during long term measurement. The features of the thermal ionizer are as follows;

- The Au target is held upper side of rod to prevent the outflow of melted gold.
- The direction of Fr extraction is vertical to the gold surface to be maximum of the extraction yield.
- The thermal ionizer has a focusing lens system just after the extract electrode to achieve a small emittance of Fr ion beam.
- The target and oven temperature can be kept over 110°C, stably by using a radiant heating type tungsten heater.
- Rb atomic beam is used for the development and performance evaluation of each apparatus. Rb is also alkali element atom and Rb ion beam extracted by the thermal ionizer is available to test and improve ion optics and transport parameter without accelerated beam.

The detail of this thermal ionizer and Rb beam was reported7).

To avoid radioactive damage of laser trap detectors, especially optical devices, Fr beam should be transported to trapping area far from the nuclear reaction region. We need not only to transport Fr beam with high transmission rate so far but also to diagnose the Fr beam profile and the number of Fr ion passed. The high vacuum of transportation area is needed for heavy ion beam. This system consists of one electrostatic deflector, three sets of electrostatic Quadrupole triplets and four diagnosis chambers8). Each diagnosis chamber has one semiconductor detector (SSD) for decayed alpha particles from unstable Fr reached a catcher foil after a slit and one ZnS viewer for Rb ion beam profile. The catcher foil is also used for Faraday Cup to measure the current of Rb ion beam.

Experiment and Results

The experiment of Fr production has been performed at CYRIC by using the thermal ionizer and the beam transport and diagnosis system with the accelerated $^{18}O^{+5}$ beam up to 100 MeV. The accelerated oxygen beam was transported on the center of the thermal ionizer where there was the gold target with a size of ϕ12.5 mm diameter and 1mm thickness. Though the beam current was about 2 eμA at the monitor just after the accelerator, the typical beam current injected on the target was estimated at about 250 enA because the parameters of the primary beam transport wasn't optimized and a slit on the primary beam course cut off the beam to avoid activating materials around the thermal ionizer and to clear up problems of optimization of the beam transport parameters.

Figure 2 shows the alpha decaying spectrum obtained by the SSD in the diagnosis chamber directly above the thermal ionizer. The highest peak at the energy 6.54 MeV is to be the alpha decaying energy from ^{210,211}Fr and other peaks are the energies from other produced isotopes ^{208,209}Fr and daughter nucleus from Fr.

We observed the target temperature dependence of the Fr yield as shown in Fig. 3, by monitoring with the thermocouple (W/Re) attached below of the target. It is found that over 970°C which is near the melting point of the gold 1064°C, the yield is increased, drastically. Assuming that the highest peak is almost from ^{210}Fr9), the ^{210}Fr extraction yield rate was estimated from Fr detection and efficiency calculated by Monte-Carlo simulation. The maximum value is about 7×10^5/sec with the primary beam current of about 250 enA. Calculating the total production with the primary beam current, the maximum extraction efficiency of the Fr ion from the thermal ionizer is evaluated at about 40%, which is the highest extraction efficiency of Fr. The primary beam current dependence of Fr production is shown in Fig. 4, thus Fr production rate is almost increased as a linear function of the beam current. The transport efficiency of the Fr beam course from the diagnosis system directly above the thermal ionizer to other diagnosis system after one electrostatics deflector and one quadropole triplet were measured. The maximum efficiency is about 20% even though design values expected was over 90%. This means that the emittance of the Fr ion beam after the thermal ionizer was worse than our assumption.

Next Step and Plan

The current experimental limit of the e-EDM value is less than 1.05×10^{-27} e cm$^{10)}$, therefore the target of the measurement precision of e-EDM is less than 10^{-28}. To achieve our aim, about 10^7/sec of Fr for the injection rate into the Neutralizer is required by roughly estimation. To attain this production rate, we have some planes. One is to increase the current of primary beam by the optimization of beam transport and the development of the extraction of the ECR10 ion source because from our data the Fr production rate might be almost in proportion to the primary beam current. Transport efficiency is already increased about twice and the result of the ECR10 ion source development is expected to increase it by a few times. Therefore, totally about 2 euA of the primary beam current is expected on the target. Another plan is to replace the focusing lens system in the thermal ionizer. The new focusing lens system is already installed and the test experiment was performed11). This lens system has five-element lens, which has five sequential electrodes capable of being applied voltages independently and the high efficiency extraction electrode those shapes are optimized by the simulation software SIMION. In Fig. 5, the experimental result by using Rb beam as same setting of the Fr experiment show that the beam transport efficiency are improved about 90%.

After repairing of the accelerator and primary beam courses of CYRIC from the earthquake disaster, we will perform the experiment by high intense $^{18}O^{+5}$ beam about 2 eμA with upgrade ECR10 ion source, then the $^{210}Fr^{+}$ rate of the entry of the Neutralizer is expected to achieve 10^7/sec.

References

1) Pospelov E. M. and Khriplovich B. I., Sov. J. Nucl. Phys. **53** (1991) 638.
2) Bernreuther W., Suzuki M., Rev. Mod. Phys. **63** (1991) 313.
3) Khriplovich B. I. and Lamoreaux K. S., “CP Violation Without Strangeness”, Springer (1998).
4) Mukherjee Debashis, Sahoo K.B., Nataraj S. H., and Das P.B., Journal of Physical Chemistry **A113** (2009) 12549.
5) Kawamura H. et al., *Proceedings of 5th International Workshop on Fundamental Physics Using Atoms 2011*, edited by N. Sasao (Okayama, Japan, 2011). Sato T. et al., *ibid*. Harada K, et al., *ibid*. Kato T. et al., *ibid*.
6) Kawamura H. et al., in this Report. Sato T. et al., *ibid*. Harada K. et al., *ibid*.

7) Hayamizu T. et al., *Proceedings of 4th International Workshop on Fundamental Physics Using Atoms 2010*, edited by N. Sasao (Osaka, Japan, 2010)

8) Oikawa A. et al., *Proceedings of 4th International Workshop on Fundamental Physics Using Atoms 2010*, edited by N. Sasao (Osaka, Japan, 2010)

9) Stancari G., Veronesi S., Corradi L., Atutov N.S., Calabrese R., Dainelli A., Mariotti E., Moi L., Sanguinetti S. and Tomassetti L., Nucl. Instrum. Meth. **A557** (2006) 390.

10) Hudson J. J., Kara D. M., Smallman J. I., Sauer E. B., Tarbutt R. M., and Hinds A. E., Nature **473** (2011) 493.

11) Liu S. et al., *Proceedings of 5th International Workshop on Fundamental Physics Using Atoms 2011*, edited by N. Sasao (Okayama, Japan, 2011).

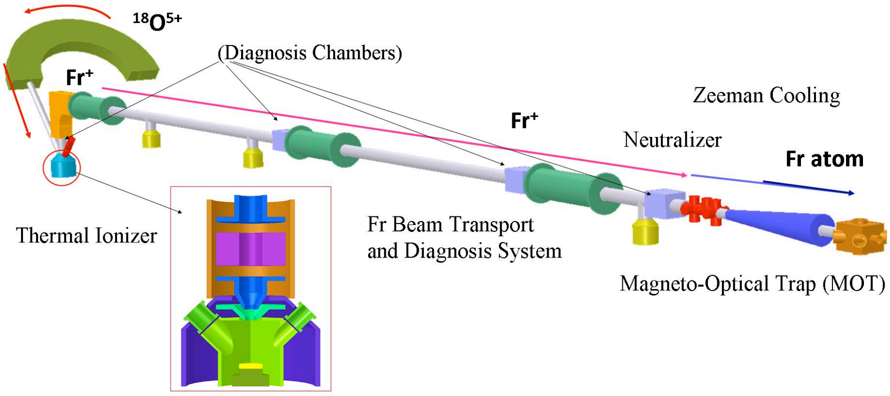

Figure 1. Schematic view of a high intensity laser cooled Francium factory at Cyclotron and Radioisotope Center (CYRIC), Tohoku Univ. The trap and measurement area to measure the EDM for Fr atom trapped by using Magneto-Optical Trap (MOT) after Fr atom slows down through Zeeman slower.

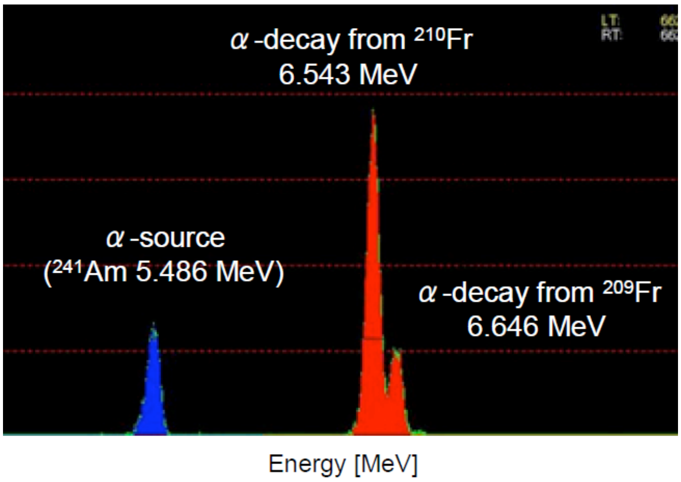

Figure 2. The horizontal axis corresponds to the energy of the alpha particles decaying from ^{208,209}Fr, ^{210,211}Fr and ^{241}Am obtained by the SSD. The vertical axis shows the number of the alpha particles. The left peak at 5.486MeV is the alpha source of ^{241}Am installed in the diagnosis chamber for the energy calibration.

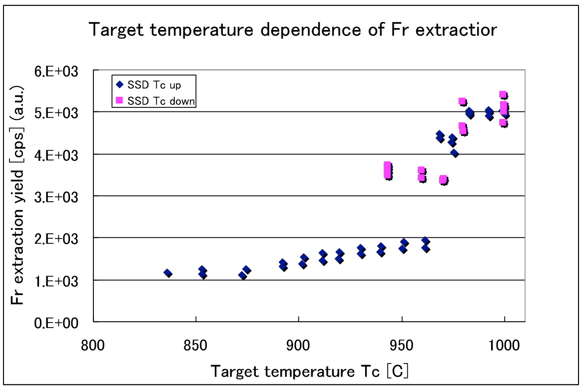

Figure 3. The target temperature dependence of Fr extraction yield: The target temperature is monitored by the thermocouple (W/Re) set near target inside the target rod.

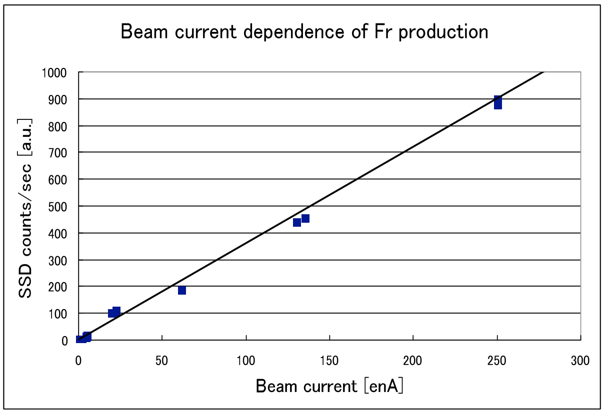

Figure 4. Beam current dependence of Fr detection rate: “SSD counts” is corrected by subtracting background, which are daughter nucleus with long life times decayed from Fr.

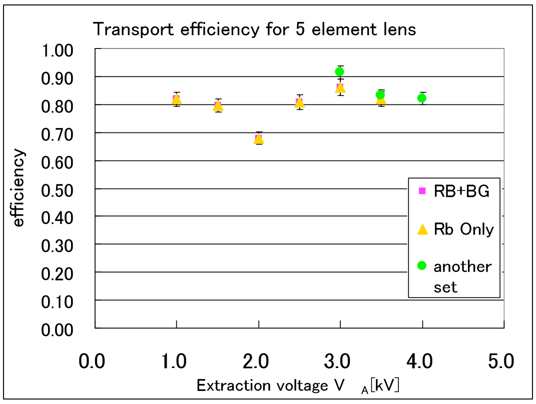

Figure 5. The transport efficiency for new focusing lens system with 5-element lens by using Rb beam: The efficiency is defined as the current ratio of Faraday Cup 2 (FC2), which is located at after the quadropole triplet downstream from the deflector from FC1, which is located just above the thermal ionizer.

I. 3. Development of a Neutralizer for the Search of an Electron EDM

Kawamura H.[1], Aoki T.[2], Ezure S.[1], Furukawa T.[3], Harada K.[1], Hatakeyama A.[4], Hatanaka K.[5], Hayamizu T.[1], Imai K.[6], Itoh M.[1], Kato T.[1], Liu S.[7], Murakami T.[6], Nataraj H. S.[1], Oikawa A.[1], Saito M.[1], Sato T.[1], Shimizu Y.[8], Uchida M.[9], Wakasa T.[10], Yoshida H.[1], and Sakemi Y.[1]

[1]Cyclotron and Radioisotope Center, Tohoku University
[2]Graduate School of Arts and Sciences, University of Tokyo
[3]Department of Physics, Tokyo Metropolitan University
[4]Department of Applied Physics, Tokyo University of Agriculture and Technology
[5]Research Center for Nuclear Physics, Osaka University
[6]Department of Physics, Kyoto University
[7]Department of Physics, Jilin University
[8]Department of Physics, Tohoku University
[9]Department of Physics, Tokyo Institute of Technology
[10]Department of Physics, Kyusyu University

The existence of a non-zero electric dipole moment (EDM) implies the violation of time reversal symmetry. As the time-reversal symmetry violation predicted by the standard model (SM) for the electron EDM is too small to be observed with the current experimental technique, an observation of the EDM indicates new physics beyond the SM. The tiny signal of the electron EDM is enhanced in the heavy atoms such as francium (Fr)[1)], which is an unstable nucleus. We are constructing the laser-cooled Fr factory to search for the electron EDM at the Cyclotron Radioisotope Center (CYRIC) at Tohoku University.

The ^{18}O beam from the AVF cyclotron bombards a gold target in a thermal ionizer, and produces Fr ions by a nuclear fusion reaction. To achieve a high precision measurement, we must perform the EDM experiment in a separate room away from the radiation controlled area to avoid stray neutrons and gamma rays produced in the nuclear reaction, which could damage the electronics. We plan to perform a high-precision EDM measurement using laser cooling and trapping techniques. Therefore, the transported Fr ion is required to be neutralized. The energy of the ion beam during transportation is a few keV. However, the energy of a neutral atom must be less than 1 eV for effective cooling. In our factory, the production of a very slow and fine neutral atomic beam is essential for an efficient optical trap. We have developed two methods of neutralization in order to choose the best method for our experiment.

The neutralization could be achieved using the electron-ion recombination process. The ion beam is neutralized by passing through electron plasma and recombining with an electron. This method has a good track record in the semiconductor industry, for example, to make a neutral gas atom soft-landing on substrate. The electron plasma is produced by a ring filament, developed by Omegatron Co., Ltd.2). In February 2011, the Fr neutralization test using this device was performed at the CYRIC 51-course beam line. The Fr ion produced in the thermal ionizer was transported into the neutralization device, and the neutralized Fr was identified by detecting alpha particles from unstable nuclei. There was a reflector electrode in front of the alpha-particle detector (solid-state detector) to separate stray ions from neutral atoms. Figure 1b shows the alpha-particle count rate as a function of the ring-filament current I_{FN} and the voltage V_{N} applied to form the electron plasma (Fig. 1a). The count rate increased with the increase on I_{FN} and V_{N}. The plasma density would be increased with the increase in these as well. Consequently, it could be considered that the probability of the recombination process was increased by increasing the electron plasma density and the number of Fr neutralized with plasma was increased. In this test experiment, it could be estimated that the maximum neutralization efficiency was around 20%. At the time, the acceleration voltage of the ion beam was 1.0 kV. However, a significant signal of neutralization was not detected when the acceleration voltage was 2.5 kV. This could be due to the ion energy dependence of the recombination-process cross section. The ion beam is required to be decelerated to less than 1 eV for laser cooling. Such a low energy ion beam is easy to spread, however, and the efficient transportation of the ion beam is very difficult. As we could not balance efficient beam transport of ion and adequate deceleration, it is nearly impossible to achieve the slow and fine Fr atom beam using this method.

Another way to achieve neutralization is to use the thermal neutralization. If the beam enters certain heated material, thermal ionization or neutralization would arise depending on the work function of the material. Yttrium has a smaller work function (3.1 eV) than the ionization energy of Fr (4.0 eV), and hence is generally used to neutralize Fr. We employ a method to form a collimated beam of Fr atoms, which is based on the principle of the orthotropic source3). The source consists of an yttrium-neutralizer target and platinum-ionizer oven surrounding the target. Platinum has so large of a work function (5.6 eV) that it can ionize Fr. As a negative voltage is applied to the target, particles ionized on the surface of the oven are attracted to it. The particles are neutralized on the surface of the yttrium, and some of the particles go out through the small aperture of the oven. Thus, we can produce the collimated neutral atom beam. Other particles interrupted by the wall of the oven would be ionized on the platinum, and would be attracted to the yttrium again. Because of such a recirculating process, the ionic beam can be converted into atomic beam, minimizing the loss of Fr. In our factory, the oven must also have a large hole to accept the incident ion beam. To realize an efficient conversion, it is essential to minimize the particles that escape through the hole. Therefore, an additional electrode is placed around the ionizer oven. This electrode applied with positive voltage can confine the ion to the oven. Based on this concept, a device shown in Fig. 2a has been developed. The neutralizer target and the ionizer oven are made by tantalum coated with yttrium and platinum, respectively. So far, the test experiment of rubidium (Rb) conversion has been done for a performance evaluation. The ionization energy of Rb that is a stable element is close to that of Fr. The temperature of the oven is typically 1,000°C, and the voltage applied to the target is -1,000 V. The Rb converted into a neutral atom is ionized on a filament in a detection region and is detected by an electron multiplier. There is a reflector electrode in front of the filament. Figure 2b shows the neutralizer voltage dependence of the detected count rate. The count rate increases with an increase in the applied voltage. It seems that the conversion probability is increased because the ion is more strongly attracted and confined. More detailed studies are required for the optimization of the conversion efficiency. When Fr is fed to this converter, the alpha-particle detection allows us to perform a more reliable measurement of the conversion efficiency.

Concerning the Fr EDM experiment, two methods of the Fr neutralization have been developed: the electron-ion recombination method and the orthotropic source method. According to studies up to now, the latter method would be more appropriate to our experiment. In addition to the neutralization device, the laser cooling devices such as laser lens and Zeeman slower will be developed. We will study the laser cooling of the neutralized atomic beam. This work was partially supported by Science research grant-in-aid (Nos. 21104005 and 23740166) and Tohoku University’s Focused Research Project.

References

1) Mukherjee D., Sahoo B.K., Nataraj H.S., Das B.P., J. Phys. Chem. A **113** (2009) 12549.
2) Omegatron Co., Ltd. http://www.omegatron.co.jp/
3) Dinneen T., Ghiorso A., Gould H., Rev. Sci. Inst. **67** (1996) 752.

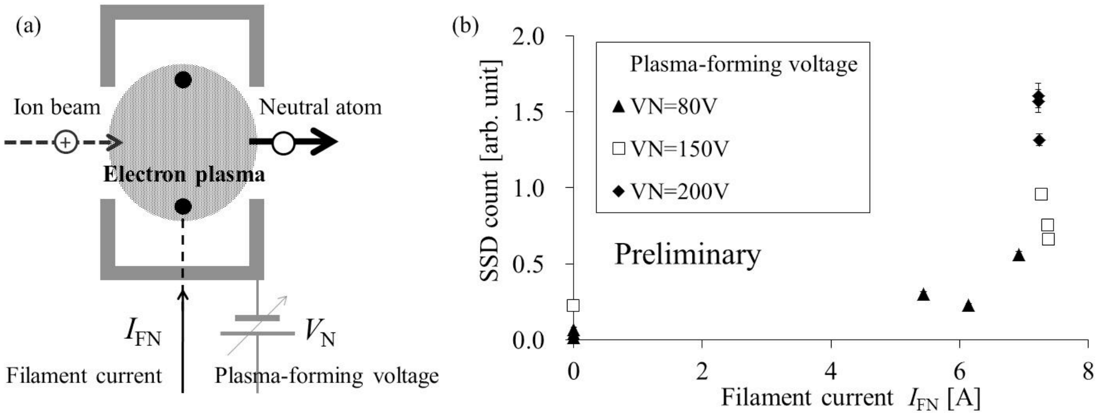

Figure 1. (a) Electron-plasma generator with a ring filament and a plasma-forming electrode. (b) The filament-current dependence of the Fr count rate.

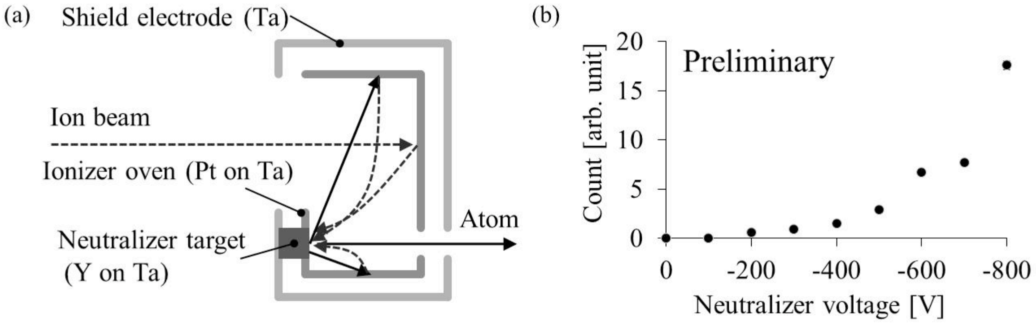

Figure 2. (a) Orthotropic source type ion-to-atom beam converter. (b) The neutralizer-voltage dependence of the Rb count rate.

I. 4. Toward Magneto-Optical Trap of Fr Atoms for EDM Search

Harada K.[1], Aoki T.[2], Oikawa A.[1], Hayamizu T.[1], Ezure S.[1], Itoh M.[1], Yoshida H.[1],
Kawamura H.[1], Sato T.[1], Kato T.[1], Nataraj H.[1], and Sakemi Y.[1]

[1]Cyclotron and Radioisotope Center, Tohoku University
[2]The University of Tokyo

A permanent electric dipole moment (EDM) of the fundamental particles serves as the direct signature of the violation of Time-reversal symmetry (T). The existence of the EDM also suggests a charge-parity (CP) violation on the basis of CPT theorem, and it is important key for understanding the observed matter-antimatter asymmetry in the universe. The Standard Model (SM) predicts the value of 10^{-38} e cm for the electron EDM (e-EDM)1), however this value is extremely small and far below the current detection limit. On the other hand, several theoretical models beyond the SM predict much larger e-EDM values ($10^{-26} \sim 10^{-29}$ e cm)2), which can be observed by current experiments.

The e-EDM measurement using Thallium (Tl) atomic beam is well known as the most precise measurement in the paramagnetic atoms and the upper limit of e-EDM obtained from the experiment is 1.6×10^{-27} e cm 3). The EDM enhancement factor of Tl atom is R = -585. In this experiment, the interaction time between Tl atoms and the external electric field is almost 2.5 ms. Moreover, for thermal beams the significant systematic effect is caused by the motional magnetic field $v \times E/c^2$ that comes from the atoms moving with velocity v through an electric field E. This systematic error mimics the true EDM signal and limits the accuracy of measurement of atomic EDM.

Laser cooling and trapping of atoms such as a Magneto-optical trap (MOT) is useful technique to overcome these problems. The velocity of laser cooled atoms dramatically decreases, and therefore the motion-induced magnetic field is strongly suppressed. In particular, the blue-detuned optical lattice trap caused by optical dipole force suppresses the detrimental effects induced by the atomic collision and the atom-light interaction, which reduces the systematic errors of the EDM signal4).

Additionally, the interaction time is elongated to about 1 s by using laser cooled atoms, which is much longer than that of Tl atomic beam experiment. Moreover, since the atomic ensembles are confined in a small region, it is unsusceptible to the magnetic and electric field inhomogeneities. Thus, there are several advantages of using optically cooled and trapped atoms for the measurement of atomic EDM. Additionally, Francium (Fr) being the heaviest alkali atom has a large enhancement factor, R = 895 5). The EDM experiment using laser cooled Fr atoms promises, to reach sensitivities even with their upper bounds, thus better than that of Tl atomic beam experiment. However, Fr atom poses an experimental challenge as there is no stable isotope of half-life longer than 22 min and it is radioactive.

In this report, we describe the current status of the experimental apparatus for trapping Rb and Fr atoms at Cyclotron and Radioisotope Center (CYRIC), Tohoku University. We have two experimental areas for the experiment at CYRIC; one is a general laser experimental room where the development of laser sources and its frequency stabilization for Rb and Fr MOTs are performed. We also designed the unique MOT chamber to observe the fluorescence of single atoms trapped in MOT, the other is in the radiation controlled area. Here, the preparation of experiment of Fr MOT and EDM measurement are in progress. As the operation of the cyclotron is needed for Fr production, it becomes expensive to use it for optimizing the operation parameters of the apparatus such as the ion source, beam transport system, neutralizer, and optical devices, and hence Rb atom is used.

A trapping laser light generated by external cavity laser diode (ECLD) is tuned to the $5S_{1/2}$ (F=2) → $5P_{3/2}$ (F=3) transition of ^{87}Rb atom at a wavelength of 780 nm and the output is amplified up to 1 W by tapered amplifier (TA) as shown in Fig. 1. The frequency of the light is modulated by an acousto-optic modulator in a double-pass configuration for operating the frequency precisely and it is then input into a polarization maintaining fiber (PMF). The trapping light of a few mW is divided by a polarization beam splitter (PBS) and it is utilized for the frequency stabilization of the laser sources by using frequency modulation spectroscopy method. After passing through the PMF, the light is adjusted to circular polarization and injected into a vacuum chamber in a six-beam counter-propagating MOT configuration. The power of each trapping beam is 5 mW. The axial gradient of the magnetic quadrupole field induced by anti-Helmholtz coils is about 10 G/cm at the center of the chamber. On the other hand, a second ECLD system provides 6 mW of laser light tuned to the $5S_{1/2}$ (F=1) → $5P_{3/2}$ (F=2) for repumping transition. The diameters of both lights are 20 mm.

Our experimental apparatus is based on a double MOT chamber system which is connected by 16 cm long differential pumping tube. The photograph of the MOT apparatus is shown in Fig. 2. The cross section of the tube is kept as 6 mm to maintain the pressure difference between the two chambers. The first MOT chamber is made of 316L stainless steel and the inside is evacuated by an ion pump (IP), a turbo molecular pump (TMP) and a rotary pump (RP). The vacuum pressure of the first MOT chamber is 4.2×10^{-9} torr. We have already achieved the trapping of Rb atoms in the first chamber. Figure 3 shows the Rb atomic cloud trapped in MOT which is obtained by monitoring the fluorescence from the atoms on the charge coupled device camera. The number of atoms is estimated to be about 10^{8}. The vertical and horizontal sizes of the atomic cloud are 3 and 4 mm, respectively. We have also designed the unique MOT chamber as a second MOT chamber, which can be used to observe the fluorescence of single atoms trapped in MOT. The view port of 1 inch diameter to observe atoms is placed at 21 mm from the center of the chamber. In this port, the lens system that consists of four spherical lenses is installed and advantageously used for high resolution imaging of single atoms6). For Rb atom, the fluorescence intensity from an atom in MOT is calculated to be 3.6 fW, which can be detected by an avalanche photo diode. The vacuum system of 2nd MOT chamber consists of a titanium sublimation pump, an IP, a TMP and a RP. The vacuum degree of the 2nd MOT chamber reaches 2.0×10^{-11} torr and it is enough for trapping the single atoms. The experimental result will be reported soon.

On the other hand, a 718 nm laser light generated by Ti:Sapphire laser (MBR110), which is pumped by 532 nm laser (Verdi-V18), is employed for trapping of Fr atoms. The frequency of the laser is tuned to the $7S_{1/2}$ (F=13/2) → $7P_{3/2}$ (F=15/2) D2 transition of ^{210}Fr atoms. Figure 4 shows the output power of the Ti:Sapphire laser as a function of the pump power. The maximum output power of the laser is 3.5 W when the pump laser is 18 W. We also use a repumping laser light with a wavelength of 817 nm generated by ECLD for $7S_{1/2}$ (F=11/2) → $7P_{1/2}$ (F=13/2) D1 transition. The two laser lights are then carried by single mode optical fibers whose length is 150 m to the radiation controlled area where Fr atoms are laser cooled and trapped by MOT. The trapping laser light is also divided by a PBS and is used for the frequency stabilization of laser sources.

We are constructing the MOT apparatus of Fr atoms at the 51 course beam line in the radiation controlled area. In the case of Fr, the number of atoms depends on the efficiencies of production, transportation and neutralization of Fr ions. The probability of getting large number of Fr atoms for being trapped in MOT is less. Therefore, we need the chamber such as the second MOT chamber used for Rb MOT to observe down to single atoms. In future, we would like to observe the fluorescence from single Rb atoms trapped in MOT, and we then utilize this technique for trapping Fr atoms. After optimization of Fr MOT, especially the number of atoms, we will perform EDM measurement using cold Fr atoms in optical lattice.

References

1) Pospelov M.E., Khriplovich I.B., Sov. J. Nucl. Phys. **53** (1991) 638.
2) Bernreuther W., Suzuki M., Rev. Mod. Phys. **63** (1991) 313.
3) Regan B.C., Commins E.D., Schmidt C.J., DeMille D., Phys. Rev. Lett. **88** (2002) 071805.
4) Chin C., Leiber V., Vuletic V., Kerman A.J., Chu S., Phys. Rev. A **63** (2001) 033401.
5) Mukherjee D., Sahoo B.K., Nataraj H.S., Das B.P., J. Phys. Chem. A **113** (2009) 12549.
6) Alt W., Optik **113** (2002) 142.

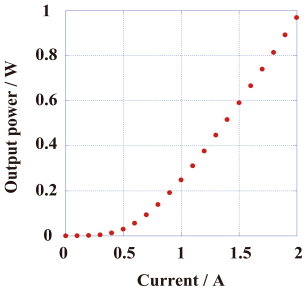

Figure 1. Output power of the trapping light amplified by the TA. The maximum output power is about 1W when the injection current is 2 A.

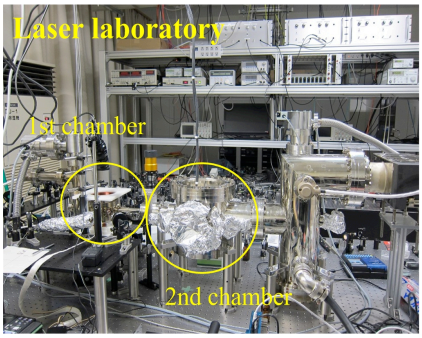

Figure 2. Photograph of the laser laboratory.

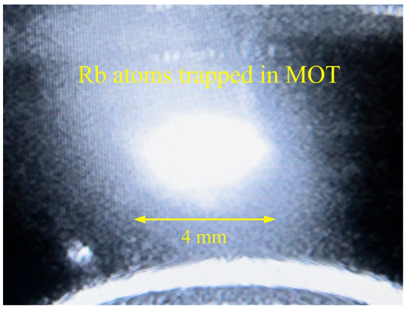

Figure 3. Fluorescence image of Rb atomic cloud trapped by MOT. Vertical size of the atomic cloud is 3 mm, and horizontal is 4 mm.

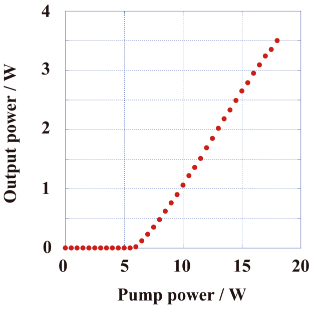

Figure 4. Output power of Ti:Sapphire laser as a function of pump power. The maximum output power of 3.5 W is obtained when the pump power is 18 W.

I. 5. Development of a New Rubidium Ion Source for the Study of a Francium Neutralizer

Sato T.[1], Ezure S.[1], Furukawa T.[2], Harada K.[1], Hayamizu H.[1], Itoh M.[1], Kato T.[1], Kawamura H.[1], Liu S.[1], Nataraj H. S.[1], Oikawa A.[1], Saito M.[1], Yoshida H.[1], and Sakemi Y.[1]

[1]Cyclotron and Radioisotope Center, Tohoku University
[2]Department of Physics, Tokyo Metropolitan University

The existence of a non-zero electric dipole moment (EDM) of an elementary particle is one of the direct signal for CP-violation that means also T-violation under the CPT theorem. The Standard Model (SM) predicts a very small electron-EDM value, $|d_e|<10^{-37}$ $e\cdot$cm. However, the Super Symmetry model, which is one of the candidates beyond the SM, predicts so large value that can be observed by the current experimental techniques. Owing to the small contributions from the SM, an EDM is a quite sensitive probe to search for physics beyond the SM.

In a paramagnetic atom, an e-EDM enhancement factor increases with atomic number Z1). We choose francium (Fr, Z=87) which is the heaviest alkali element and has the enhancement factor~895 2). Our measurement precision of the EDM can be finally reached to $|d_e|\sim10^{-28}$ e$\cdot$cm. This value is around ten times smaller than the current experimental e-EDM limit obtained in Tl experiment with $|d_e|\sim10^{-27}$ e$\cdot$cm 3).

Unfortunately, ^{210}Fr which is used for the EDM search in this project is a radioactive isotope with a half-life of 3.18 min. However, this is sufficiently long to extract, transport and trap the Fr in the magnet-optical trap (MOT) to measure the EDM. Now, we are developing a Fr factory at Cyclotron and Radioisotope Center in Tohoku University.

The fusion reaction ^{18}O+^{197}Au is employed to produce ^{210}Fr isotope. The francium is extracted and transported as an ion. As we need to trap the Fr as neutral atoms in the final stage, the ion beam must be neutralized and must be slowed down to milli-kelvin order. At present the development of a slow atomic beam system which contains a neutralizer, a transverse cooling system and a Zeeman slower is ongoing. Here, we discuss a new

Rubidium (Rb) ion source used for the development of the system.

The Fr can be produced by the nuclear fusion reaction with the primary beam energy just above the Coulomb barrier supplied from the AVF cyclotron with K=100. Therefore, we need to operate the cyclotron, if we use the Fr beam to perform the test experiment for the neutralizer. To minimize the use of the cyclotron, Rb, whose chemical property is very similar to Fr except for its mass number can be utilized. Therefore, the Rb Ion Source was developed for offline test experiments.

The principle of this ion source is based on surface ionization that is described by the Saha-Langmuir equation4). The ratio of the emitted ion and atom from a target depends on the work function of the target material and the ionization potential of the beam. In addition, a high temperature is important for efficient extraction. From these properties, molybdenum (Mo) is chosen for the target. Its work function 4.6 eV is higher than the ionization potential of Rb (4.2 eV) and Fr (4.0 eV). Its melting point 2896 K is high enough to avoid melting.

Rb atoms are supplied from a Rb ampoule by a thermal process, and are ionized on the surface of the heated Mo target by the thermal ionization. A few kV positive voltage is applied to the target, and then Rb ions are extracted by its potential.

The base of this ion source is the prototype of our Fr thermal ionizer5). To improve the beam intensity, two major upgrades were applied1). To keep the temperature of about 1300 K stably for a long time, the oven heater was changed from a cartridge heater to a Mo plate heater2). To achieve a more efficient extraction, the extraction electrode was designed with the optimization of the electric field by a finite-element method simulation using TOSCA software6). The Mo target tilted at 45 degrees was employed and the diameter of the extraction hole was extended from 1 mm to 3 mm. Other electrodes were also modified its position to optimize the extraction electric field. Designed values are the Rb extraction efficiency 10%, the beam emittance 350π mm･mrad and the beam intensity 300 enA when the Mo target temperature is 1300 K, the Rb ampoule temperature is 60 °C and the extraction voltage is 5 kV.

In September 2011, test experiment was performed at TOF room. Figure 1 shows overview of Rb Ion Source. The experimental setup is shown in Fig. 2. A triplet-Q electrode whose length is about 40 cm was connected to focus the Rb ion beam. A zinc-sulfide viewer and Faraday cup next to the triplet-Q were used to detect the beam. A gram of rubidium can be inserted into an ampoule holder and heated to around 50 °C by a ribbon heater. Figure 3 shows an experiment result. The target temperature was kept at 1100 K during about two hours and finally reached about 1300 K. The maximum extraction voltage was 1.5 kV, that was limited by the withstand voltage of a high voltage circuit. The temperature of Rb ampoule followed the target temperature with a little lag. This is due to the heating of the Rb in the ampoule by the radiant heat from the heater surrounding the Mo target. Therefore, the maximum value of the Rb temperature and the beam intensity were recorded after the target temperature maximum. The maximum beam intensity was about 600 *e*nA at 1300 K. This intensity is around ten times larger than Rb ion beam produced by the existing Fr thermal ionizer.

This ion source has worked well over few hundred hours, and can be utilized for the offline developments of the neutralizer, laser cooling, and the MOT that are installed in the Fr beam line without operating accelerator. In the future, we plan the coexistence of Rb Ion Source and the Fr beam line using "mirror reflector". Rb Ion Source will be attached perpendicularly to the Fr beam line. Then, the extracted beam can be deflected to 90 degrees by the mirror reflector, and will be injected into the neutralizer. This gives us a high-intensity Rb test beam without the rearrangement of the beam line. An upgrade of the ion source itself is also planned. Owing to the redesign of the supply of Rb atoms and the chambers, the improvement of the beam intensity and emittance can be prospected. Because of the all improvements, the beam intensity will reach to 1 *e*μA.

References

1) Sandars P.G.H., Phys. Lett. **14** (1965) 194 and Phys. Lett. **22** (1966) 209.
2) Mukherjee D., Sahoo B.K., Nataraj H.S., Das B.P., J. Phys. Chem. A **113** (2009) 12549.
3) Regan B.C., Commins E.D., Schmidt C.J., DeMille D., Phys. Rev. Lett. **88** (2002) 071805.
4) Dresser M.J., J. Appl. Phys. **39** (1968) 338.
5) Hayamizu T., et al,. CYRIC Annual Report 2009 (2010) 12.
6) http://www.vectorfields.com

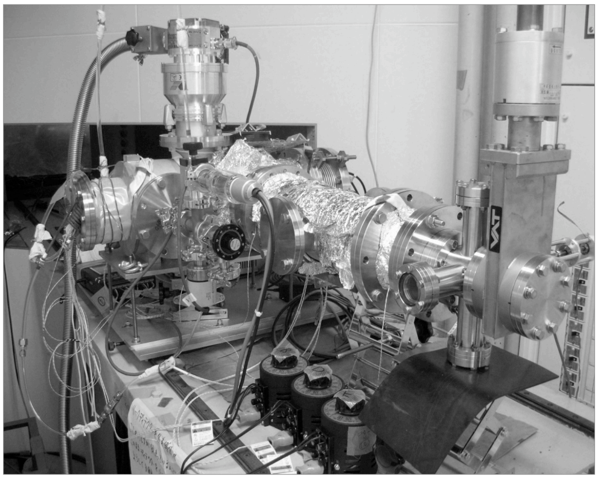

Figure 1. Overview of Rubidium Ion Source.

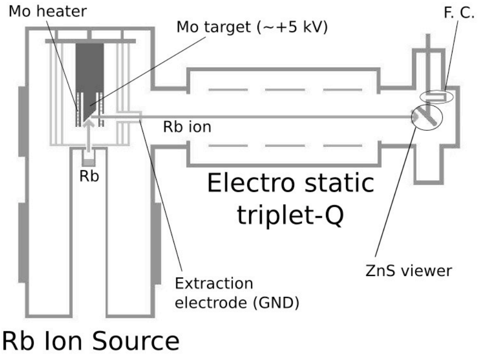

Figure 2. Experimental setup.

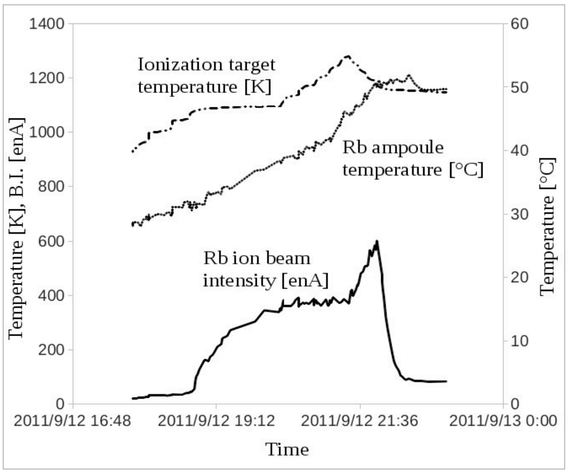

Figure 3. Test experiment result.

I. 6. Upgrade of Thermal Ionizer for the Production of High Intensity Francium Beam

Liu S.[1,2], Yoshida H.[2], Hayamizu T.[2], Saito M.[2], and Sakemi Y.[2]

[1]College of Physics, Jilin University, Changchun-130023, China
[2]Cyclotron and Radioisotope Center, Tohoku University

Introduction

The non-zero permanent electric dipole moment (EDM) of an elementary particle implies simultaneous violation of both parity (P) and time-reversal (T) symmetries and its search is in the forefront of the T-violation experiments. Assuming CPT invariance, T-violation involves an associated CP violation; the latter is the key to explain the observed matter-antimatter asymmetry in the universe.

The magnitude of the electron EDM is predicted to be of the order of 10^{-38} e·cm within the Standard Model of elementary particle physics, which is far below the current experimental reach. However, many extensions of the Standard Model such as for example, supersymmetry, multi-Higgs physics, left-right symmetry etc. predict much larger EDMs, which therefore can be verified with the ongoing and/or the proposed experiments.

Experiment

Francium (Fr) being the heaviest alkali and radioactive atom is a suitable candidate for the research of the electron EDM. Despite Fr being radioactive, we use ^{210}Fr with a half-life of about 3 min for the EDM experiment for the reason that it has large EDM enhancement factor as the latter scales as the cube of the atomic number: $K \sim Z^3\alpha^2$. The relativistic coupled cluster theory predicts the enhancement factor of Fr with 895 at present$^{1)}$. In addition, the energy level structure of Fr is such that it can be easily subjected to laser cooling and trapping.

In our experiment, we produce Fr by the nuclear fusion reaction: $^{18}\mathrm{O}+^{197}\mathrm{Au}\rightarrow^{210}\mathrm{Fr}+5\mathrm{n}$. The ^{18}O beam from AVF cyclotron at CYRIC, Tohoku University with the beam energy of 100 MeV, which is just above the coulomb barrier and chosen so as to maximize the production of Fr, is bombarded on the gold target at an angle of 45°. The target is being heated to a temperature of more than the melting point of the gold 1337K. After the reaction, the produced Fr atoms move to the surface by diffusion. Then the Fr desorbs from the target surface as atoms and ions. After surface ionization in the Thermal Ionizer (TI) the produced Fr^+ ion beam is extracted by the extraction electrode and focused by the two einzel lenses subsequently and transported up to the deflector, which will bend the beam line from vertical to horizontal direction, and transport further to the three sets of quadrupole triplets. At the end of this beam line, we have a neutralizer to neutralize the ions back into atoms. These atoms are slowed down using Zeeman cooling system and further transported to the laser room, where these atoms are cooled to velocities as low as a few μK using Magneto-optical trap and eventually measure the Fr EDM in the optical lattice. Thus, we have obtained 10^6 Fr^+/sec yield$^{2)}$.

To improve the sensitivity of the EDM measurement, one needs to improve both extraction and transportation efficiency of the Fr^+ ion beam to obtain much more Fr production yields. The transverse beam emittance also needs to be improved to prevent further losses; the smaller the emittance better would be the beam quality. The transportation efficiency, the beam profile and the beam emittance depend highly on the geometry of the lens system and the shape of the electric field.

In our experiment, the Fr^+ ion beam is transported up to the length of 11 m from TI to neutralizer, thus a parallel beam is required to maintain high transportation efficiency with small beam size. To achieve this, an electrostatic lens system having five or higher number of lens elements is desirable since only they have afocal zoom. The conditions for "afocal zoom lens" are given in the following equations:

$$M = (V_5/V_1)^{-1/4},\ \frac{V_5}{V_3} = \frac{V_3}{V_1},\ \frac{V_4}{V_3} = \frac{V_2}{V_1} \qquad (1)$$

where M is the magnification and V_1 to V_5 are the voltage potentials applied for the first to the fifth element$^{3)}$.

Lens design and Simulation

Modeling of electrostatic lenses is carried out using the charged particle optics simulation software called SIMION. By replacing the present two einzel lenses with a five-element lens system and modifying the geometry of extraction electrode and lens system, we aim to obtain high extraction and transportation efficiency with small beam emittance and beam size.

One of the most important parameters which affect both beam emittance and beam focal point is the opening angle of target rod. To optimize the electric field distribution around the target rod, we have studied the effect due to variation in the rod angle on beam emittance and focal point. We have varied the opening angle from 73 degree to 85 degree, and at 82 degree we have observed the farthest focal point of ion beam with relatively low beam emittance (Fig. 1 (a)). Thus, we have chosen 82 degree as the new opening angle of target rod. Another important parameter on which both beam emittance and beam diameter depend is the distance between target and extraction electrode. By changing the distance from 14.5 mm to 16.5 mm we have found that between 14.6 and 14.8 mm both the beam emittance and beam diameter have the lowest values (Fig.1 (b)). Considering the fact that during the experiment the gold target melts thereby increasing the distance in the process, we decided to choose 14.6 mm as the distance between target and extraction electrode. The dependence of beam emittance and beam diameter on the distance between target surface and lens system has also been studied. As shown in Fig 1 (c), the beam emittance remains more or less constant where as the beam diameter decreases as the distance increases. Thus we have chosen the middle point-101 mm, which is the beam focal point after extraction electrode to make sure the stability of both beam emittance and beam size.

Results and Conclusion

We have upgraded the TI based on the design mentioned above. We have performed the test experiments with the upgraded TI using stable rubidium beam. We can see that the forms of distribution of the extraction efficiency in simulation shown in Figs. 2 (a) and (c) are very close to the form of distribution of the beam current in experiment, shown in f Figs. 2 (b) and (d). We have improved the transportation efficiency from 50% to more than 80% with the highest value being 91.4%. We presume that this improvement is due to the optimized beam emittance, the simulated value of which had been minimized from 36.1 mm•mrad to 18.3 mm•mrad.

We expect to perform the experiment using Fr beam next and improve the transportation efficiency up to 94% by applying a higher voltage (up to 5 kV) to gold target and oven. The Fr beam intensity will hopefully reach 10^7 Fr^+ /sec with the ^{18}O beam intensity of 2 eμA using the upgraded ECR ion source and with the upgraded TI.

References

1) Mukherjee D., Sahoo B.K., Nataraj H.S., Das B.P., J. Phys. Chem. **A 113** (2009) 12549.
2) Sakemi Y., et al., J. Phys. Conf. Series **302** (2011) 012051.
3) Sise O., Ulu M., Dogan M., Nucl. Instr. and Meth. **A 554** (2005) 114.

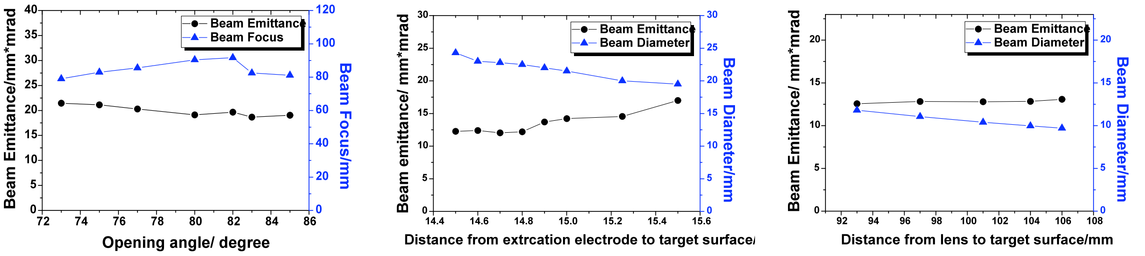

(a) (b) (c)

Figure1. Effect of opening angle change on beam emittance and focal point (a); Dependence of beam emittance and beam diameter on the distance between target surface and extraction electrode to beam emittance and beam diameter (b) and on the distance between target surface and lens system (c).

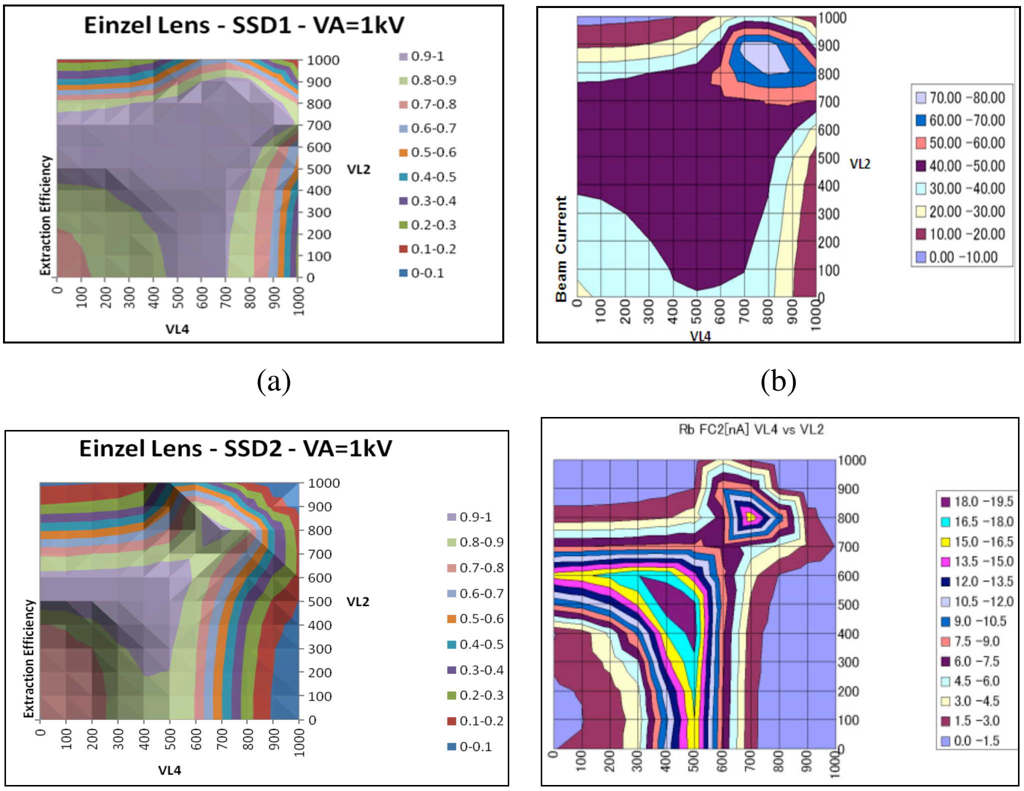

(a) (b)

(c) (d)

Figure 2. Distribution of the extraction efficiency in simulation (a),(c) and beam current in experiment (b),(d) at SSD1 and SSD2 for two einzel lens system with the voltage applied for oven and target VA=1kV. X axis shows the voltage applied for VL4 and Y axis shows the voltage applied for VL2.

I. 7. Search for the Bandhead of the Hoyle State + α Cluster Structure in ^{16}Ovia the ^{12}C(^{16}O,^{16}O*[α+X])^{12}C Reaction

Itoh M., Harada K., Hayamizu T., Kawamura K., Liu S., Nataraj H., Oikawa A., Saito M., Sakemi Y., Sato T., and Yoshida H.

Cyclotron and Radioisotope Center, Tohoku University

The α-particle condensate has gained much attention in light nuclei. The concept of the α-particle condensate was proposed by Tohsaki et al[1]. The 7.65 MeV 0_2^+ state of ^{12}C has been considered to be a candidate for the 3α particle condensate in which all constituent α clusters enter into the lowest S-orbit, and loosely bound. The 7.65 MeV 0_2^+ state of ^{12}C is called Hoyle state which plays an important role of the nucleosynthesis heavier than ^{12}C. However, the 4α particle condensate state in ^{16}O has been not established, yet. According to the α condensate model, the 15.1 MeV 0^+ state is considered to be a candidate of the 4α particle condensate[2]. In the previous experiment, we have measured decay α particles from the 15.1 MeV 0^+ state in ^{16}O via the ^{12}C(^{16}O,^{16}O*[α + X])^{12}C reaction in order to investigate the 4α-particles condensate in the ^{16}O nucleus[3]. Since the wave function of the 4α-particles condensate state in ^{16}O has a large amplitude of the ^{12}C(0_2^+)+α channel, the decay width of the 15.1 MeV 0^+ state to the ^{12}C(0_2^+) + α channel was considered to be large compared to other channels. However, although the decay α particles to the ground state (g.s.) and the first 2+ state of 12C from the 15.1 MeV 0+ state were observed, decay α particles to the 12C(02+) + αchannel were not detected. Due to the Coulomb barrier, the decay to the 12C(02+)+α channel is considered to be suppressed.

Recently, the 15.1 MeV 0+ state is considered to have a character of the superfluidity from the viewpoint of a rotational band with a 12C(02+) + α cluster structure[4]. They claimed the moment of inertia for the 15.1 MeV 0+ state is drastically reduced due to the superfluidity in the 4α condensate state. In addition to the superfluidity of the ^{12}C(0_2^+) + α cluster structure, they also claimed there was a band head 0^+ state at around 16.6 MeV.

However, no 0^+ state have been reported in experimental studies so far. In the experiment of inelastic α scattering at E_α = 386 MeV in RCNP, Osaka University, we obtained the preliminary result for the existence of the 0^+ state at around 16.6 MeV with a width of about 1 MeV. In this study, we measured decay α particles from the around 16.6 MeV region in ^{16}O via the $^{12}C(^{16}O,^{16}O^*[\alpha+X])^{12}C$ reaction in order to search for the band head 0^+ state with a $^{12}C(0_2^+) + \alpha$ cluster structure.

The experiment was performed at the CYRIC 41 course beam line by using a large scattering chamber. The 160 MeV $^{16}O^{5+}$ beam accelerated in the K=110 MeV AVF cyclotron was transported into the large scattering chamber in the experimental room TR-4 and bombarded to the self-supporting carbon target. The experimental setup was same as the previous experiment[5)]. The beam current was typically 10 p nA. The target was the natural carbon foil of the 50.0 μg/cm^2 thick and rotated by 45° against the beam axis in order to keep the enegy loss of the recoil carbon below 400 keV. The recoil ^{12}C was caught in the silicon detectors at 61° (SSD0) and 48.5° (SSD1). For monitoring the beam position, the energy of the recoil ^{12}C from elastic scattering of $^{16}O + ^{12}C$ was measuring at 73.5° during the experiment. If the beam position shifted by 1 mm, the energy of the recoil ^{12}C changed about 600 keV. For a detector of decay α particles, we used the position sensitive detector (PSD) of the 50 mm×50 mm size and 994 μm thick, which is a double-sided silicon strip type and has 16 strips in each side. We measured decay particles in three angles of the PSD at 9°, 17.5°, and 26° to cover decay-α particles from the $^{16}O^* \rightarrow \alpha + ^{12}C(g.s.)$ channel. We also installed two BGO detectors in order to estimate the contribution of the $^{12}C(^{16}O,^{16}O^*[\alpha + X])^{12}C(2^+)$ reaction. However, it was so small that it was neglected in this analysis.

Figure 1(a) shows the kinematic calculation of the recoil 12C energy and angle for the excitation energy of ^{16}O at Ex = 16.5 MeV, which is shown by a bold solid line. The red-hatched region shows the acceptance of SSD0. The crossed area between the kinematic calculation of the recoil ^{12}C and the acceptance of SSD0 corresponds to the SSD0 energy from 8.3 to 9.3 MeV, as shown in Fig. 1(b). Since the width of the 0^+ state obtained in the RCNP experiment is about 1 MeV, cross section of this excitation energy decreases gradually toward the high excitation energy. Figure 2 shows the missing mass spectrum of the reaction obtained by gating this energy region. The missing mass was calculated from the recoil ^{12}C and one of decay particles by assuming the $^{16}O^* \rightarrow ^{12}C+\alpha$ decay. The decays of the $^{12}C(g.s.)+\alpha$ and $^{12}C(2^+)+\alpha$ channels are clearly seen in Fig. 2.

The count ratio between the ground state and the first 2^+ state is about 4:3. In order to estimate the branching ratio between these two channels, we carried out the Monte-Carlo simulation and compared with the count ratio obtained in this experiment. The estimated branching ratio is about 1:1. The ratio of the ^{12}C(2^+) + α channel is larger than the previous reported 15.1 MeV 0^+ state in ^{16}O$^{2)}$. The decay to the ^{12}C(0_2^+) + α channel could not be separated from other decay channels and background. Further investigations are needed.

References

1) Tohsaki A. *et al*, Phys. Rev. Lett. **87** (2001) 192501.
2) Funaki Y. *et al*, Phys. Rev. Lett. 101, (2008) 082502.; Funaki Y. *et al*, Phys. Rev. C **80**, (2001) 064326.
3) Itoh M. *et al*, CYRIC Annual Report 2009 (2009) pp 5.
4) Ohkubo S. and Hirabayashi Y., Phys. Lett. **B 684** (2010) 127.
5) Itoh M. *et al*, Mod. Phys. Lett. **A 25** (2010) 1935.

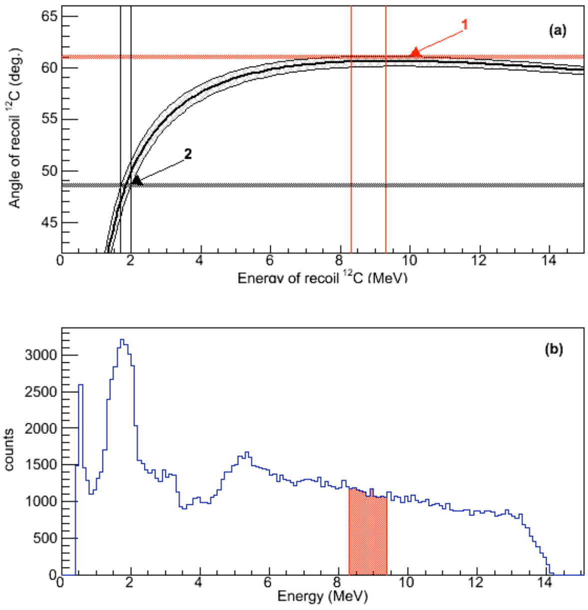

Figure 1. (a) The kinematic calculation of the recoil 12C energy and angle. (b) The energy spectrum obtained in the SSD0 detector. The red-hatched region corresponds to the excitation energy of about 16.5 MeV in ^{16}O.

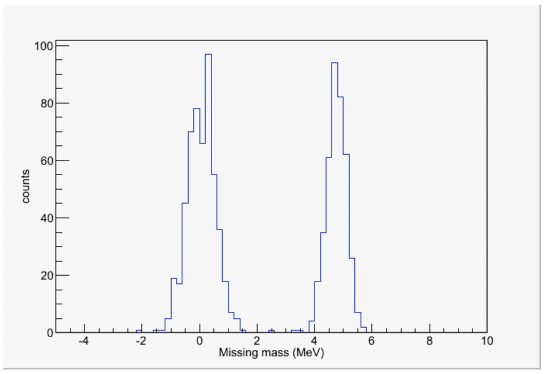

Figure 2. The missing mass spectrum obtained from decay ^{12}C particles. The peak around 0 MeV corresponds to the ^{12}C(g.s.) + α decay channel. That around 4.4 MeV corresponds to the ^{12}C(2^+) + α decay channel. The branching ratio between ^{12}C(g.s.) + α and ^{12}C(2^+) + α channel was estimated to be about 1:1.

II. 1. Development of a Sextupole Ion Beam Guide for Improvement of the RF-IGISOL

Shimada K.[1]*, Takahashi M.*[2]*, Ueno H.*[2]*, Izumi S.*[2]*,*
Wakui T.[1]*, and Shinozuka T.*[1]

[1]*Cyclotoron and Radioisotope Center, Tohoku University*
[2]*Department of Physics, Tohoku University*

A sextupole ion guide (SPIG)1) has been introduced into the radio frequency ion guide isotope separator on-line (RF-IGISOL)2) for reduction of the energy spread of the transported beam and improvement of the efficiency as compared with the skimmer-based technique.

The ion guide technique uses a gas-filled volume to thermalize the reaction products recoiling out of the target. In the case of RF-IGISOL the recoil ions are then collected and transported by the DC and RF electric fields and the gas jet through the exit hole of the cell. A skimmer is used to separate and focus the ions from the gas jet and to inject them in the acceleration stage of the separator. In order to focus the ions through the skimmer, it placed close to the exit hole, and an electric field is applied between the cell and the skimmer electrode. In this field, therefore, the vacuum is poor and the ions collide with the residual gas atoms, which causes the energy spread of the extracted beam. The SPIG is installed between the exit hole and the skimmer for improving the vacuum, and makes a pseudopotential for focusing and trapping the ions during the transport. The pseudopotential formed by RF 2*N*-pole fields is described as a function of the cylindrical coordinate *r* as

$$\Phi = \frac{qN^2}{4m\omega^2}\left(\frac{V_{\mathrm{RF}}}{r_0}\right)^2\left(\frac{r}{r_0}\right)^{2(N-1)},$$

where q, m, ω, V_{R} and r_0 are the ion charge, mass, RF frequency, RF voltage and the inner radius of the beam guide, respectively.

The SPIG consists of 6 rods of 1.0 mm in diameter and 40.0 mm long are mechanically supported and electrically insulated by glass ceramics (photoveel). A diameter of the inner circle of the SPIG is 1.8 mm. A distance between the exit hole of the RF carpet and the SPIG can change from 0 to 6 mm. The rods are supplied with RF voltages between adjacent pairs, that are approximately 100 V at 2 MHz. The geometry of the electrodes is shown in Fig. 1, and a photo of the SPIG assembly is shown in Fig. 2.

Now we are preparing offline and online experiments.

References

1) Xu H.J., Nucl. Instr. and Meth. **A 333** (1993) 274.
2) Miyashita Y., PhD. thesis, Tohoku University (2008).

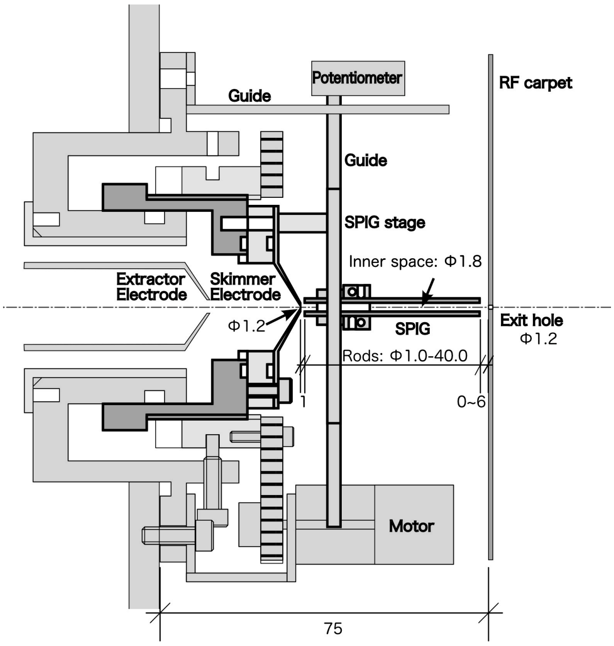

Figure 1. Schematic view of the SPIG.

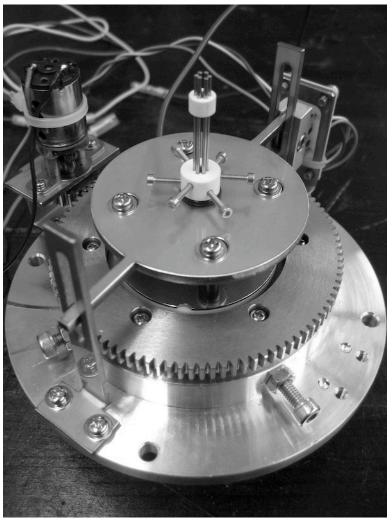

Figure 2. Photo of the SPIG assembly.

II. 2. New Electron Cyclotron Resonance Ion Source for Heavy-ions

Wakui T.[1], Shinozuka T.[1], Shimada K.[1], Sakemi Y.[1], Itoh M.[1], Yoshida H.[1], Chiba S.[2], Ohmiya Y.[2], Takahashi N.[2], Takahashi K.[2], Yokogawa S.[2], and Suzuki J.[2]

[1]Cyclotron and Radioisotope Center, Tohoku University
[2]SHI Accelerator Service

Heavy ions delivered for the 930 cyclotron have been produced using a 14.5 GHz electron cyclotron resonance ion source (ECRIS) made of all-permanent-magnet[1)]. This ion source can produce multi-charged ions of gaseous elements up to argon. Typical beam intensities extracted from the 14.5 GHz ECRIS are 10 eμA for $^{16}O^{5+}$ and 1.5 eμA for $^{40}Ar^{9+}$. Recently, improvements in beam intensity and energy are requested from users. To meet the needs, we have newly installed a 10 GHz ECRIS, which was operated at RIKEN accelerator research facility[2-4)].

The 10 GHz ECRIS has eight solenoid coils for producing axial magnetic field. The currents for the coils can independently be varied to optimize an axial field profile. A plasma chamber is 100 mm in diameter and 520 mm in length. A microwave of 10 GHz is axially introduced into the plasma chamber, which works as a multimode cavity. The maximum microwave power is 1 kW. The extraction voltage is varied around 10 kV according to the injection condition to the 930 cyclotron. Gas mixing can be performed to obtain higher beam intensity for highly charged ions.

The first beam for a user experiment using the 10 GHz ECRIS was $^{16}O^{5+}$ at June, 2010. In Fig. 1, a charge state distribution of ^{16}O obtained at the experiment is shown with the solid line. For comparison, a typical beam current of ^{16}O from the 14.5 GHz ECRIS is also plotted with the dashed line. In these measurements, parameters for the ECRISs were optimized to maximize the beam current of $^{16}O^{5+}$. The beam current of 200 eμA is achieved for $^{16}O^{5+}$ using the 10 GHz ECRIS. The achieved beam current is more than 10 times higher than the current of $^{16}O^{5+}$ from the 14.5 GHz ECRIS.

The beam energy accelerated by a cyclotron is proportional to the square of the charge state of ions. The beam energy can thus be increased by increasing the charge state of ions. As can be seen from Fig. 1, the $^{16}O^{7+}$ beam from the 10 GHz ECRIS is obtained with a current of 10 eμA, which is comparable to the current of $^{16}O^{5+}$ from the 14.5 GHz ECRIS. Hence, the beam energy for ^{16}O can be increased by using the $^{16}O^{7+}$ beam from the 10 GHz ECRIS, without a decrease in beam current.

The 10 GHz ECRIS has been used for 10 experiments with beams of $^{16}O^{5+}$, $^{18}O^{4+}$, $^{18}O^{5+}$ and $^{12}C^{4+}$ in FY2010. For further enhancement of beam intensity, beam energy and variety of ions from the 930 cyclotron, we have some improvement plans including an optimization of gas mixing and introduction of so-called an accel-decel extraction system and of a metallic sample insertion system.

References

1) Yamazaki A., Fujita M., Tanaka E., Shinozuka T., Yokoi T., Ozawa T. and Tanaka H., Rev. Sci. Instrum. **73** (2002) 589.
2) Nakagawa T., Jpn, J. Appl. Phys., **30** (1991) L930.
3) Nakagawa T., Kageyama T., Kase M., Goto A., Yano Y., Jpn. J. Appl. Phys. **31** (1992) L1129.
4) Nakagawa T., Aihara T., Higurashi Y., Kidera M., Kase M., Yano Y., Arai I., Arai H., Imanaka M., Lee S. M., Arzumanyan G., and Shirkov G., Rev. Sci. Instrum. **75** (2004) 1394.

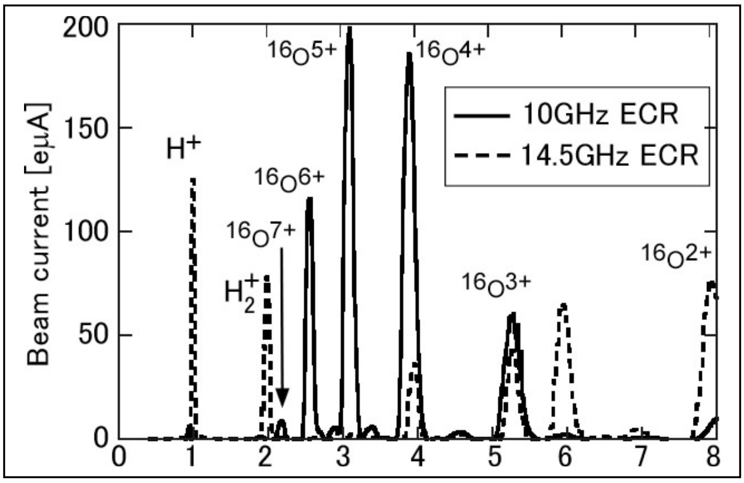

Figure 1. Charge state distributions of ^{16}O.

II. 3. Performance of the High Intensity Fast Neutron Beam Facility

Yoshida H., Itoh M., and Sakemi Y.

Cyclotron and Radioisotope Center, Tohoku University

Recently, demands for the material irradiations by neutron or ion beams have greatly increased and various irradiation studies have been performed at various facilities. These include the studies of radiation damages in the materials to be used in the high radiation environments at the reactor and/or accelerator facilities, such as permanent and electromagnets1), semiconductors and radiation detectors. Also urgent needs exist in the estimation of the radiation-caused soft errors in the integrated circuits of CPU's of the computers, FPGA (Field Programmable Gate Array)2,3) and different kinds of memories such as S-RAM's and D-RAM's4).

At CYRIC, the 32-course beam line has been put in use in a variety of neutron irradiation experiments, and improvements have been continued to achieve high intensity neutron beams. In this report, the present status of the high intensity fast neutron beam facility is described. Figure 1 shows the schematic view of the neutron beam facility. The primary proton beams in the energy range of 20-80 MeV are transported to bombard the water-cooled ^{7}Li production target. The beam penetrating the target is swept out by the 25° clearing magnet, and stopped in the water-cooled beam dump. High intensity primary beams of several μA are available, and by using the $^7\mathrm{Li}(p,n)^7\mathrm{Be}$ reaction, the intensity of quasi-monoenergetic neutron beams of up to a few 10^{10} n/sr/sec/μA are obtainable.

From March 2010 to February 2011, 10 experiments of 18 days in total (beam time of 32 shifts) were performed at this facility. In about 80% of the experiments, proton beam of 70 MeV to yield 65 MeV quasi-monoenergetic neutrons were used. The typical neutron energy spectrum, which was measured with the time-of-flight method by using a liquid scintillation counter is shown in Fig. 2. In this case, the thickness of the lithium target was 7.8 mm and the neutron yield, normalized to the beam current and integrated over the energy range of 60-70 MeV, was about 0.9×10^{10} n/sr/μA/sec. The highest yield achieved was about 3×10^{10} n/sr/sec for the primary proton beam with a current of 3.5 μA. This means that the flux at the sample placed at 1.2 m distance from the lithium target was about 2×10^{6} n/cm^2/sec. The largest amount of the accumulated flux in one experiment was about 5×10^{11} n/cm^2 at the sample placed at 1.2m from the ^{7}Li target for the practical irradiation time of 50 hours.

The irradiation demands for researches in not only property changes of materials but also soft errors mechanism of working devices are now increasing. To supply higher intensity neutron beams and/or neutron beams with smaller spot size needed to confine the irradiation area precisely, and to prepare user friendly interfaces to allow the beam on/off and the system to realize easy sample changes are currently in consideration.

References

1) Tanigaki M. et al., CYRIC Annual Report (2008) 31.
2) Akiyama M. et al., CYRIC Annual Report (2009) 39.
3) Toba T. et al., CYRIC Annual Report (2009) 46.
4) Hayakawa T. et al., CYRIC Annual Report (2009) 52.

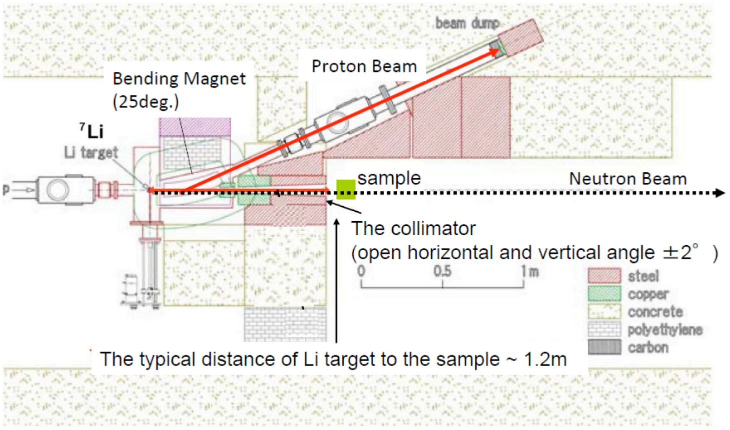

Figure 1. The schematic view of the high intensity neutron beam facility located at the 32-course.

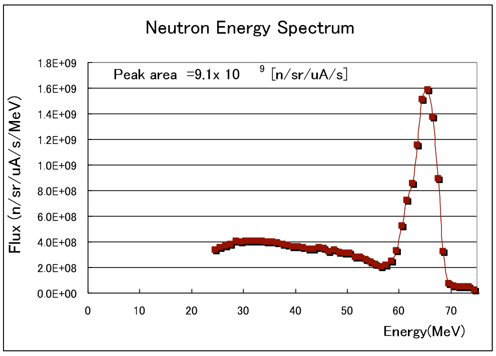

Figure 2. The typical neutron energy spectrum for the primary proton beam of 70 MeV. The obtained energy resolution was about 6 MeV in FWHM, measured by the Time of Flight (TOF) method.

III. 1. Investigation of an Optimum Clustering Condition for TlBr Detectors

Tada T.[1], Hitomi K.[1], Xu Y.[1], Kim S.-Y.[1], Yamazaki H.[1], and Ishii K.[2]

[1]*Cyclotoron and Radioisotope Center, Tohoku University*
[2]*Graduate School of Engineering, Tohoku University*

Introduction

Thallium bromide (TlBr) has been investigated as a promising semiconductor detector for decades since it has wide band gap energy (2.68 eV) and high photon stopping power originating from the high atomic numbers (Tl:81, Br:35) and high density (7.56 g/cm^3). However, considerable charge collection loss is observed in the TlBr detectors due to the poor charge transport properties of holes. Thus the shape of signal waveforms from the detector varies depending on the gamma-ray interaction position and the observed pulse height is no longer proportional to the deposited energy in the detector.

Various methods such as pulse shape discrimination, the depth sensing technique, co-planar grid structures, and the signal digitizing technique have been developed to overcome the problem of charge collection loss[1-7)]. Among these methods, the digitizing technique processes signals from detectors by a software program running on a processor. Therefore, processing of signals is much more flexible than that of other techniques and the electronics required for the digitizing technique are also simple. Recently, we have developed a digital signal processing system for improving performance of TlBr detectors[8,9)]. The clustering method based on the digital processing system has successfully improved energy resolutions of the detectors by correcting the pulse height variation[9)]. In this study, an optimum condition of the clustering process for the TlBr detectors was investigated in order to obtain the best performance from the detectors. The relationship between the number of clusters and the energy resolution of spectra was evaluated and the best cluster number was determined for the TlBr detectors.

TlBr detectors and signal processing method

Planar TlBr detectors were fabricated from a crystal grown by the traveling molten zone (TMZ) method. The starting material for the crystal growth was commercially available TlBr powder with nominal purity of 99.999%. The material was zone-purified with a horizontal zone furnace. After the purification, single zone pass was performed to improve the crystallinity. The grown crystals were cut into wafers with a diamond wire saw. The two surfaces of the wafers were polished mechanically. The wafers with the dimensions of 5×5×0.5 mm^3 were prepared for detector fabrication. Circular electrodes with a diameter of 3 mm were deposited on the polished surfaces by vacuum evaporation of thallium through a shadow mask. Then, aluminum was deposited on the thallium electrodes and thin palladium wires were attached to the electrodes using carbon paste.

The detector was placed in an aluminum box with a BNC connector for connection to a charge-sensitive preamplifier (Clear Pulse 580K). The cathode surface of the detector was irradiated with a ^{137}Cs gamma-ray source. The detector at around 10-20 ºC was operated at 150 V. The preamplifier output waveform was directly digitized by means of a digital oscilloscope (Tektronix DPO3032) with a sampling rate of 100 MS/s and 8 bit resolution. The digitized waveforms were transferred to a personal computer for analysis. The waveforms were classified into clusters based on the shape for the waveforms by using K-mean clustering algorithm. The 10,000 waveforms were used for formation of reference patterns. The number of reference patterns (= the number of clusters) was set to be from 50 to 1,000. The 65,000 waveforms were classified into the clusters by using the reference patterns. The detailed clustering processes were described elsewhere9). The classified waveforms were shaped by a digital version of CR-$(RC)^4$ filter with a shaping time of 2 μs to form an energy spectrum for each cluster. The peak centroid of the spectrum associated with each cluster was aligned to suppress the pulse height variation of the signal waveforms.

Results and discussion

The energy spectrum processed with 100 clusters is shown in Fig. 1. The original spectrum is also shown in the figure for comparison. The full energy peak counts were increased by applying the clustering process. The energy resolution at 662 keV was improved to be 3.1% FWHM. The number of clusters was increased in order to improve the energy resolution further. The energy spectrum processed with 1,000 clusters is shown in Fig. 2. The energy resolution of 0.9% was achieved by simply increasing the number of clusters. The energy resolution as a function of the number of clusters is shown in Fig. 3. As shown in the figure, improvement of the energy resolution is saturated in more than about 500 clusters. The result indicates that the 500 clusters are enough to process signal waveforms from the planar TlBr detector. By employing more than 500 clusters, improvement of energy resolutions is mainly limited by the signal to noise ratio for the signal waveforms originating from the near anode events.

The number of processed waveforms for the number of clusters is show in Fig. 4. The number of processed waveforms decreases sharply in the region of less than 500 clusters. This can be explained by the fact that the number of waveforms in each cluster decreases by the classification of waveforms. On the other hand, a gradual decrease of the number of processed waveforms is observed in the region of more than 500 clusters. The result indicates that the decrease of the number of waveforms in each cluster is suppressed by providing the enough number of clusters for processing signal waveforms from the TlBr detector. The result is consistent with the relationship between the energy resolution and the number of clusters mentioned above.

Conclusion

An optimum condition of the clustering process was investigated for planar TlBr detectors in order to obtain the best performance from the detector. The energy resolution of the full energy peak of 662 keV was measured for energy spectra obtained with from 50 to 1,000 clusters. The energy resolution was almost constant (about 1%) for more than 500 clusters. The result indicated that the 500 clusters were enough for processing signal waveforms from the planar TlBr detectors. The best energy resolution of 0.9% FWHM was achieved with 1,000 clusters. By processing signal waveforms with the enough number of clusters (=more than 500 clusters), improvement of the energy resolution was mainly limited by the signal to noise ratio for the waveforms originating from the near anode events.

References

1) Redus R., Squillante M.R., Lund J., Nucl. Instr. and Meth. **A380** (1996) 312.
2) Jordanov V. T., Panatazis J. A., Huber A., Nucl. Instr. and Meth. **A380** (1996) 353.
3) Richter M., Siffer P., Nucl. Instr. and Meth. **A322** (1992) 529.
4) Luke P.N., Appl. Phys. Lett. **65** (1994) 2884.
5) He Z., Vigil R.D., Nucl. Instr. and Meth. **A492** (2002) 387.
6) Hitomi K., et. al., Nucl. Instr. and Meth. **A607** (2009) 112.

7) Takahashi H., Fukuda D., Kurahashi T., Iguchi T., Nakazawa M., Nucl. Instr. and Meth. **A380** (1996) 381.

8) Tada T., Hitomi K., Tanaka T., Wu Y., Kim S., Yamazaki H., Ishii K., Nucl. Instr. and Meth. **A638** (2011) 92.

9) Tada T., Hitomi K., Wu Y., Kim S., Yamazaki H., Ishii K., Nucl. Instr. and Meth. **A659** (2011) 242.

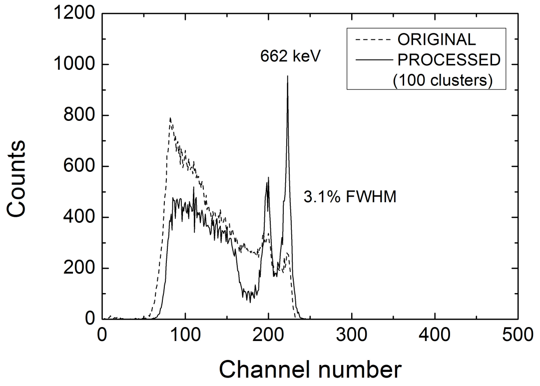

Figure 1. Original and processed energy spectra measured for a 0.5 mm thick TlBr detector with a ^{137}Cs gamma-ray source.

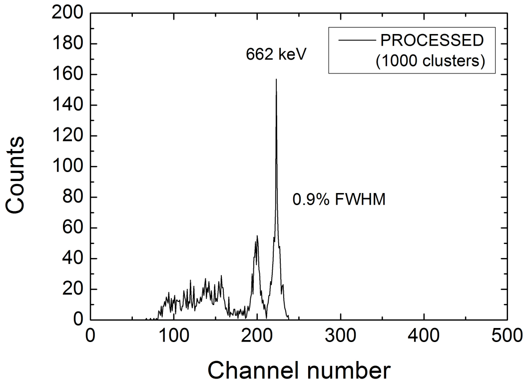

Figure 2. ^{137}Cs energy spectra processed by the clustering method with 1,000 clusters.

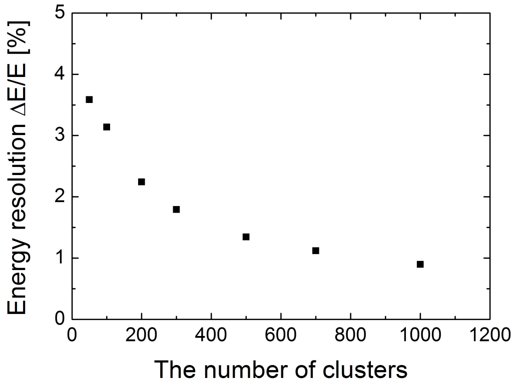

Figure 3. Energy resolution ΔE/E as a function of the number of clusters. ^{137}Cs photo-peak was used for the evaluation of resolutions.

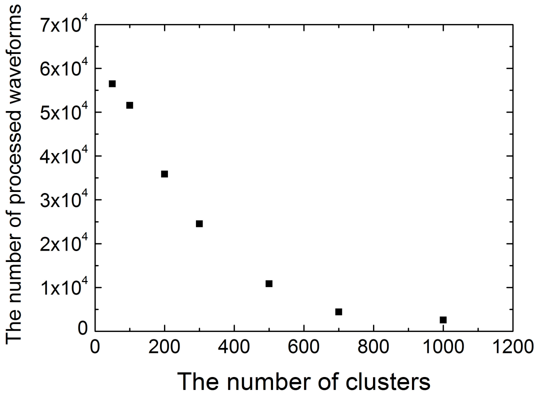

Figure 4. The number of processed waveforms as a function of the number of clusters.

III. 2. Measurement of Electron Drift Mobility in TlBr Crystals

Hitomi K.[1], Tada T.[1], Xu Y.[1], Kim S.-Y. [1], Yamazaki H.[1], and Ishii K.[2]

[1]*Cyclotoron and Radioisotope Center, Tohoku University*
[2]*Graduate School of Engineering, Tohoku University*

Thallium bromide (TlBr) is a compound semiconductor promising for fabrication of efficient radiation detectors with high energy resolutions at room temperature. TlBr crystals exhibit high photon stopping power originating from its high atomic numbers (Tl: 81, Br: 35) and high density (7.56 g/cm^3). The wide bandgap energy (2.68 eV) results in the high resistivity of TlBr crystals (~10^{10} Ω·cm) at room temperature, enabling the device to operate with low noise. TlBr melts congruently at the melting point of 460 °C and has no destructive phase transition between the solidification and room temperature. Hence, purification and crystal growth of TlBr can be performed simply from the melt. Due to its attractive physical properties, semiconductor detectors fabricated from TlBr crystals were studied by numerous researchers[1-8)].

One of the most important physical properties for semiconductor radiation detector material is the drift mobility (μ) which determines the charge collection efficiency and the pulse rise time of the device. In a conventional method for measuring drift mobility in semiconductor detectors, planar detectors are irradiated with alpha particles or low energy X-rays creating electron-hole pairs near the incident surface in order to make electrons or holes drift across the entire detector thickness. Then, the carrier drift time is measured from the pulse waveform obtained from the output of the preamplifier connected to the planar device. The drift mobility can be derived from the equation:

$$\mu = \frac{d}{E \cdot t_{drift}}, \tag{1}$$

where d is the detector thickness, E is the electric field inside the device and t_{drift} is the carrier drift time. The conventional method is susceptible to error although the measurement is easy to implement. The values of drift mobility measured using alpha particles can be affected strongly by the surface condition of the detector. Low energy X-rays produces small number of electron-hole pairs in the device, resulting in low signal to noise ratio for the mobility measurement.

In order to overcome the problems mentioned above, the direct measurement method was developed and implemented to CdZnTe devices9). In the method, the device is irradiated with the high energy gamma-rays (662 keV) and the gamma-ray interaction position is determined by the depth sensing technique10). The carrier drift time is then measured from the pulse waveform originating from the near cathode event selected based on the depth of interaction information.

In this study, the direct measurement method was applied to TlBr Frisch collar detectors in order to measure the electron drift mobility. The crystal growth, detector fabrication and mobility measurement are described in this paper.

Commercially available TlBr powder with purity of 99.999% was employed for the crystal growth. Further purification of the starting material was performed by the zone refining method. After the purification, TlBr crystals were grown by the traveling molten zone method.

Frisch collar detectors were fabricated from the grown crystals. Bar-shaped crystals with the dimensions of 2 mm×2 mm×4.4 mm were cut from the grown TlBr ingot using a diamond wire saw. The 2 mm×2 mm surfaces were polished mechanically in order to remove the damaged surface layers originating from the cutting process. Planar electrodes were formed on the 2 mm×2 mm surfaces by vacuum evaporation of Tl. Applying Tl electrodes to TlBr detectors is effective for suppressing the polarization phenomena at room temperature11). Since Tl is susceptible to oxidation, Al was evaporated onto the Tl electrodes to form an overcoat. The side surfaces of the bar-shaped crystal were wrapped with Teflon tape. A Frisch collar electrode was constructed by wrapping Al foil around the side surfaces. The Frisch collar covered the entire side surfaces of the device. Figure 1 shows the fabricated TlBr planar detector and TlBr Frisch collar detector. The device was mounted on a substrate and thin Pd wires were attached to the electrodes (cathode, anode and Frisch collar) with conductive adhesive. Frisch collar detectors operate as a single polarity charge sensing device, in which the induced charge on the anode depends mainly on the collection of electrons and scarcely affected by the hole movement. The Frisch collar detector design was applied to CdZnTe and the detectors exhibited excellent spectroscopic performance12).

Performance of the TlBr Frisch collar detectors was evaluated at room temperature. The TlBr Frisch collar detector was placed in a shield box. The cathode and the anode were connected to charge-sensitive preamplifiers (CLEAR PULSE 580 K). The Frisch collar electrode and the cathode were maintained at ground potential. Positive bias voltage of 500 V was applied to the anode. The cathode was irradiated with a ^{137}Cs calibration source. The output signals from the preamplifiers were fed into shaping amplifiers (CANBERRA 2025 for the cathode and ORTEC 673 for the anode). The shaping times for the cathode and the anode were 6 μs. The peak amplitude for the cathode and anode pulses was analyzed by a multi-channel ADC board. The data were analyzed on a PC event by event to obtain pulse high spectra as a function of the cathode to anode signal ratio. The gamma-ray interaction depth is determined by taking the cathode to anode signal ratio in single polarity charge sensing devices10). The cathode to anode signal ratios were grouped into 21 bins in the measurements.

Figure 2 shows ^{137}Cs spectra obtained from a 2 mm×2 mm×4.4 mm TlBr Frisch collar detector. The acquisition time was 2 hours in real time. The anode spectrum exhibited an energy resolution of 2.9% FWHM at 662 keV. The Tl X-ray escape peak and the backscatter peak are discernible in the spectrum. The K X-rays of Ba from the ^{137}Cs source were detected by the detector, which confirmed that the electrons created by the Ba K X-rays near the cathode surface traversed the entire detector length, implying less electron trapping in the crystal.

Measurement of electron drift mobility in the TlBr Frisch collar detector was performed by measuring the preamplifier output waveforms for the near cathode event as shown in Fig. 3. The carrier drift time was measured to be 16 μs in the waveforms. Using the equation (1), the electron drift mobility was estimated to be 24.2 $cm^2/V \cdot s$. The obtained mobility value is consistent with the reported data13).

References

1) Hitomi K., Murayama T., Shoji T., Suehiro T., Hiratate Y., Nucl. Instr. and Meth. **A428** (1999) 372.
2) Hitomi K., Onodera T., Shoji T., Nucl. Instr. and Meth. **A579** (2007) 153.
3) Shah K.S., Lund J.C., Olschner F., Moy L., Squillante M.R., IEEE Trans. Nucl. Sci. **36** (1989) 199.
4) Gostilo V., Owens A., Bavdaz M., Lisjutin I., Peacock A., Sipila H., Zatoloka S., Nucl. Instr. and Meth. **A509** (2003) 47.
5) Owens A., Bavdaz M., Brammertz G., Gostilo V., Haack N., Kozorezov A., Lisjutin I., Peacock A., Zatoloka S., Nucl. Instr. and Meth. **A497** (2003) 359.
6) Kozlov V., Kemell M., Vehkamäki M., Leskelä M., Nucl. Instr. and Meth. **A576** (2007) 10.

7) Churilov A.V., Ciampi G., Kim H., Cirignano L.J., Higgins W.M., Olschner F., Shah K.S., IEEE Trans. Nucl. Sci. **56** (2009) 1875.
8) Kim H., Churilov A., Ciampi G., Cirignano L., Higgins W., Kim S., O'Dougherty P., Olschner F., Shah K., Nucl. Instr. and Meth. **A629** (2011) 192.
9) He Z., Knoll G.F., Wehe D.K., Nucl. Instr. and Meth. **A411** (1998) 114.
10) He Z., Knoll G.F., Wehe D.K., Rojeski R., Mastrangelo C.H., Hammig M., Barrett C., Uritani A., Nucl. Instr. and Meth. **A380** (1996) 228.
11) Hitomi K., Shoji T., Niizeki Y., Nucl. Instr. and Meth. **A585** (2008) 102.
12) McNeil W.J., McGregor D.S., Bolotnikov A.E., Wright G.W., James R.B., Appl. Phys. Lett. **84** (2004) 1988.
13) Hitomi K., Matsumoto M., Muroi O., Shoji T., Hiratate Y., J. Cryst. Grow. **225** (2001) 129.

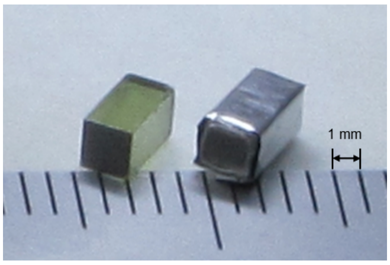

Figure 1. A TlBr planar detector (left) and a TlBr Frisch collar detector (right). The dimensions of the crystals were 2 mm×2 mm ×4.4 mm.

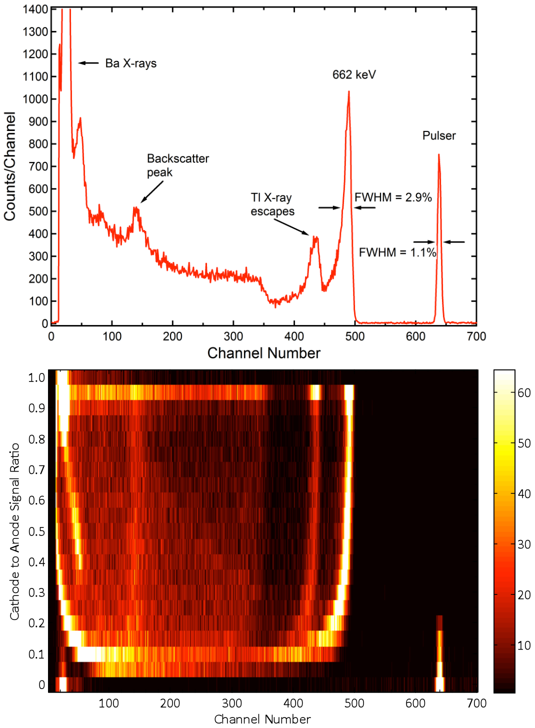

Figure 2. ^{137}Cs spectrum obtained from the anode of a 2 mm×2 mm×4.4 mm TlBr Frisch collar detector (top) and the relationship between the anode pulse height and the cathode to anode signal ratio (bottom).

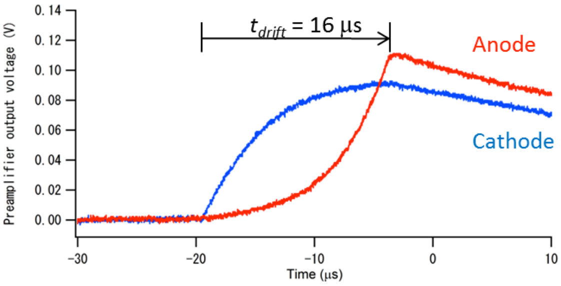

Figure 3. Pulse waveforms obtained from the anode and cathode of a TlBr Frisch collar detector. The gamma-ray interaction position was near the cathode surface.

IV. 1. Development of Positron Emission Mammography (PEM) for Commercial Use

Miyake M.[1], Yamamoto S.[2], Itoh M.[1,3], Itoh S.[4], Sato H.[4], Kumagai K.[1],
Tashiro M.[1], and Baba M.[3]

[1]*Cyclotron and Radioisotope Center, Tohoku University*
[2]*Department of Electrical Engineering, Kobe City College of Technology*
[3]*Sendai Medical Imaging Clinic*
[4]*Furukawa Industrial Machinery Systems Co., Ltd.*

Introduction

Breast cancer is one of the leading causes of morbidity among Japanese women. The disease can be treated relatively easily if detected early because it can be easily identified and grows on the surface of the body. So we developed positron emission mammography (PEM) specialized for breast cancer diagnosis.

Here, we introduce the basic features of this scanner during its development, describing the gantry, detector unit, and measurement system. The resulting PEM scanner that was eventually commercialized in 2010 is much smaller than conventional PET scanners, and its reduced size affords advantages of improved spatial resolution and lower costs.

Large area PEM detector unit

We developed a large area PEM detector unit (156×208 mm^2) consisting of four 140.8×44 mm^2 inorganic scintillator crystals arrays and four 1×3 FP-PMTs, stored in an aluminum case shielded from light (Fig. 1). Two PEM detector units were used for the PEM scanner and were set up in parallel.

Prototype PEM scanner

The prototype PEM scanner shown in Fig. 2 consists of a gantry, chair, and an electronics cabinet. The gantry has two detector units and a moving mechanism. The electronics cabinet contains analogue to digital converters, pulse discrimination circuits, coincidence circuits, high voltage and low voltage power supply, and a PC with an interface. The pulse discrimination circuits and coincidence circuits are both field-programmable gate array circuits. The PC stores the scanned raw data and reconstructs the raw data to images.

Commercial PEM scanner

The prototype scanner was subsequently commercialized in 2010 and is shown in Fig. 3. The gantry was downsized and redesigned for clinical use, to be comfortable for both patients and operators. The main electronics circuit was the same as that used in the prototype scanner. The power supply and electronics wiring were improved for noise reduction, and the electronics cabinet was downsized. A scanner is currently installed in Sendai Medical Imaging Clinic and is being used for clinical examinations.

Acknowledgement

The prototype PEM scanner development project was supported by a grant from the Regional Research and Development Resources Utilization Program of the Japan Science and Technology Agency (JST), and the commercial PEM scanner development project was supported by a grant from the Innovation Promotion Project of the New Energy and Industrial Technology Development Organization (NEDO).

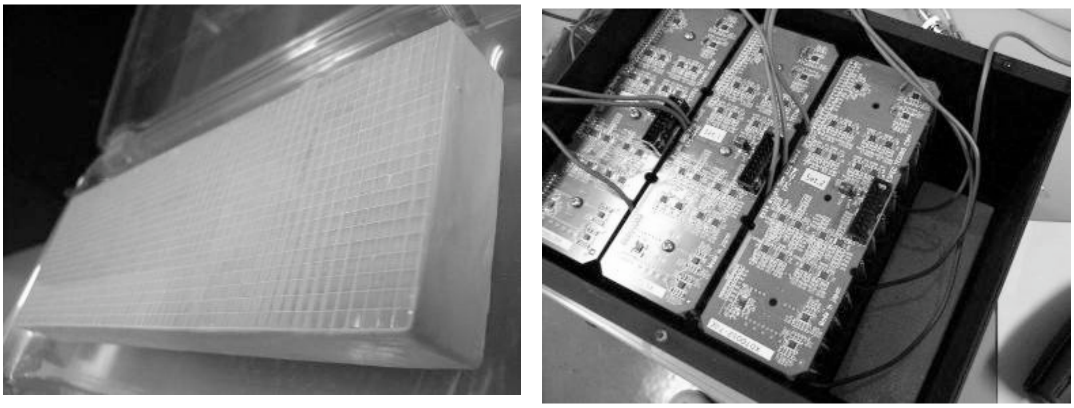

Figure 1. Inorganic scintillator crystal arrays. The size of the crystal is 2.2×2.2×15 mm^3 and that of the arrays is 140.8×44 mm^2 (left). Opened cover of the PEM detector unit shows an aluminum case, an inorganic scintillator crystal array and electronic circuits for FP-PMTs (right).

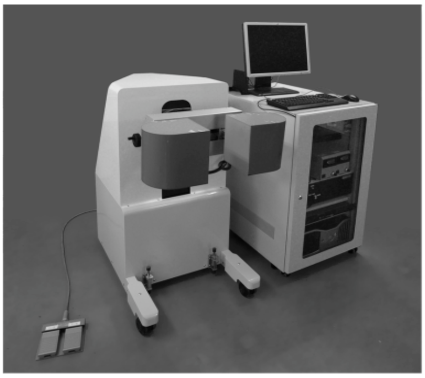

Figure 2. The prototype PEM system. Gantry (left) and electronics cabinet (right). There are two detector units in front of the gantry. The electronics circuits, power supply, and PC are contained in the electronics cabinet.

Figure 3. The commercial PEM scanner. Set up in the breast scan mode.

IV. 2. A Preliminary Study of Proton Therapy Combined with Cisplatin

Terakawa A.[1,2], Ishii K.[1,2], Matsuyama S.[1], Kikuchi Y.[1], Ito Y.[1], Yasunaga S.[1],
Tagawa A.[1], Kawamura T.[1], Takahashi Y.[1], Hatori Y.[1], Hamada N.[1], Fujiki K.[1], Miura Y.[1],
Yamazaki H.[3], Funaki Y.[3], Itoh N.[4], Wada S.[4], and Sera K.[5]

[1]*Department of Quantum Science and Energy Engineering, Tohoku University*
[2]*Graduate School of Biomedical Engineering, Tohoku University*
[3]*Cyclotron and Radioisotope Center, Tohoku University*
[4]*School of Veterinary Medicine and Animal Sciences, Kitasato University*
[5]*Cyclotron Center, Iwate Medical University*

A proton beam is expected to have small radiation effects on normal tissue in comparison to a photon beam because of its superior dose distribution, the so-called Bragg peak while a clinical proton beam generating a spread-out Bragg peak have about the same biological effects on tumor cells as an X-ray. Thus, sensitization in proton therapy may provide significant therapeutic advantages over conventional radiotherapy.

The chemotherapeutic agent Cisplatin (cis-diamminedichloro-platinum(II) : CDDP) not only inhibits tumor growth but also give rise to therapeutic enhancement when combined with radiotherapy1). The aims of this study were to evaluate therapeutic enhancement for proton therapy combined with CDDP administration in a murine solid tumor model, and to investigate platinum concentration in the treated tumor by means of conventional and submilli PIXE analyses to study a relationship between the CDDP uptake and the enhanced anti-tumor effects caused by the combined treatment. In this report, preliminary results of the CDDP-combined proton therapy and the PIXE analysis of the treated tumors are described.

The experiment was performed using a proton therapy system2) at Cyclotron and Radioisotope Center (CYRIC), Tohoku University. NFSa fibrosarcoma cells (5.0×10^6) were transplanted into both hind legs of C3H/He male mice aged 10-12 weeks old. When tumor sizes reached a mean diameter of about 10 mm, CDDP was administered intraperitoneally to the mice at a single dose of 10 mg/kg. For proton therapy alone, the tumors in the right hind legs received local proton irradiation without CDDP administration as a single dose of 15 or 30 Gy at a dose rate of 4 Gy/min using an irradiation field 20 mm in diameter and a 20 mm SOBP. When CDDP and proton therapy were combined, the tumors in the right hind legs were also irradiated locally with a single dose of 30 Gy 1 hour after CDDP administration. The tumor diameters were measured after the treatments using a small animal CT-scanner (Clairvivo® CT, SIMAZU Co. Ltd., Japan) or Vernier calipers.

The conventional PIXE analysis of the tumor tissue were performed using a PIXE analysis system[3] at Nishina Memorial Cyclotron Center (NMCC), Japan Radioisotope Association. The tumors were excised from the mice 6 hours after each treatment and frozen in powdered dry ice. Sample preparation was done by means of a chemical ashing method. The tumor samples were dissolved with nitric acid using a microwave oven. Indium solution (1000 ppm) was added to the samples as an internal standard element. The samples were irradiated using a 2.9 MeV proton beam from an AVF cyclotron at NMCC. Two Si(Li) detectors were used to measure low and high X-ray energy regions separately. A sheet of mylar 500 μm thickness was used as an absorber in the high X-ray energy measurement.

Platinum distribution in the tumor tissue was investigated by means of submilli PIXE analysis at Tohoku University. We obtained tissue sections by cutting the frozen tumors in a cryostat (-20°C), and mounted them on 4 mm thick polycarbonate films. Thickness of the section was 250 μm. The samples were stored at -80°C until the PIXE analyses. Elemental maps of the samples were obtained from beam scanning with a 3-MeV proton pencil beam. The spot size of the proton beam was about 0.5 mm (FWHM). Details of the submilli camera system have been described elsewhere[4].

Tumor volumes were calculated according to $V=(6/p)abc$, where a, b and c are three orthogonal diameters of the tumor. Figure 1 shows time course of tumor volumes after each single treatment. It is found that proton therapy combined with CDDP treatment showed the therapeutic enhancement significantly. The effect of the combined treatment on tumor growth delay may be additive. The conventional PIXE analysis of the tumor sample by the internal standard method resulted in the platinum concentration of 2.6±0.3 ppm. The submilli PIXE results showed that the platinum distribution in the tumor section appears to be almost uniform (Fig. 2), suggesting that CDDP reached hypoxic cell region as well as oxygenated cells in the tumor.

In conclusion, the significant therapeutic enhancement was observed in proton therapy combined with CDDP treatment on the basis of the murine NFSa fibrosarcoma model. The conventional PIXE analysis using the internal standard method showed that the platinum concentration in the tumor inducing the therapeutic enhancement was 2.6±0.3 ppm. The submilli PIXE analysis of the tumor sections has revealed that CDDP distribution may be almost uniform in the tumor.

This work was partially supported by Grants-in-Aid of the Ministry of Education, Culture, Science, Sports and Technology, Japan (Scientific Research (B) Nos. 17300169 and 20300174 (A. Terakawa), and Exploratory Research No. 19650128 (A. Terakawa)), and by the Molecular Imaging Program of Tohoku University.

References

1) Bartelink Harry., et al., Radiotherapy and Oncology, **6** (1986) 61.
2) Terakawa A., et al., The proceedings of the 16th Pacific Basin nuclear Conference (16PBNC), Aomori, Japan, Oct. 13-18, 2008 paper ID : P161378.
3) Sera K., et. al., Int. J. of PIXE, **2** (3) (1992) 325.
4) Matsuyama S., et al., Int. J. of PIXE, **8** (2&3) (1998) 209.

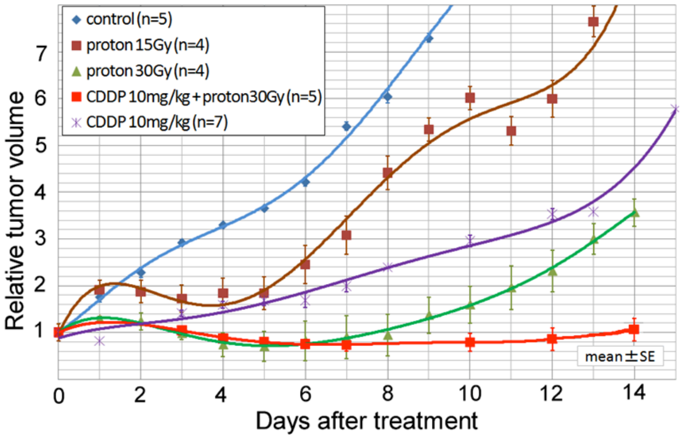

Figure 1. Time course of the tumor volumes of proton therapy alone , CDDP treatment alone and the combined treatment.

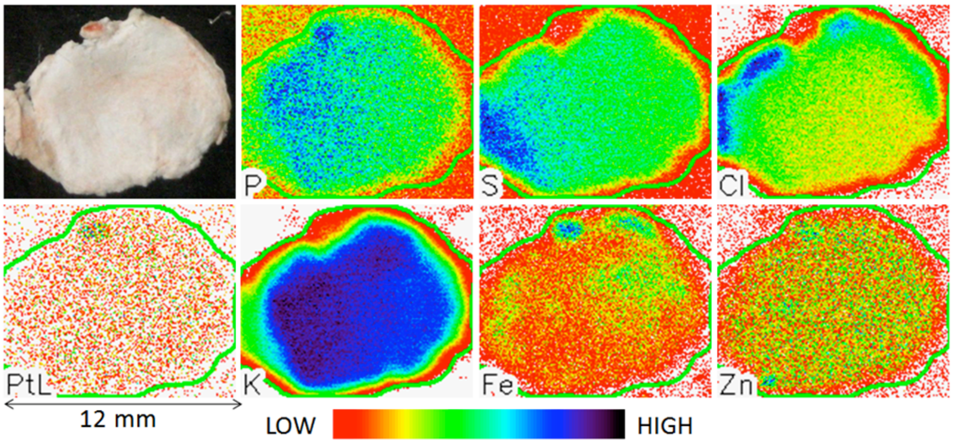

Figure 2. Elemental maps obtained from the submilli PIXE of the tissue section of the CDDP-treated tumor (10 mg/kg).

V. 1. PIXE Analysis of a Murine Fibrosarcoma Tumor Treated With a Vascular Disrupting Agent AVE8062

Terakawa A.[1,2], Ishii K.[1,2], Matsuyama S.[2], Kikuchi Y.[2], Yasunaga S.[2], Ito Y.[2], Tagawa A.[2], Kawamura T.[2], Takahashi Y.[2], Sugai H.[2], Hamada N.[2], Fujiki K.[2], Hatori E.[2], Yamazaki H.[3], Funaki Y.[3,4], Furumoto S.[3,4], Itoh N.[5], and Wada S.[5]

[1]Graduate School of Biomedical Engineering, Tohoku University
[2]Department of Quantum Science and Energy Engineering, Tohoku University
[3]Cyclotron and Radioisotope Center, Tohoku University
[4]Tohoku University Graduate School of Medicine
[5]School of Veterinary Medicine and Animal Sciences, Kitasato University

We have studied therapeutic effects of proton therapy combined with a vascular disrupting agent AVE8062[1,2)] using a murine fibrosarcoma (NFSa) tomor. Although AVE8062 treatment causes rapid tumor blood flow interruption leading to extensive necrosis in the tumor tissue, the cells at the tumor periphery survive the treatment and cause tumor regrowth. As a result, the tumor receiving AVE8062 administration consists of inner necrotic-cell and outer viable-cell regions. Thus, spatial distributions of elements in the AVE8062-treated tumor are expected to be different from those in an untreated tumor. The aim of this study was to evaluate spatial distributions of principal elements in a solid tumor treated with AVE8062 on the basis of particle-induced x-ray emission (PIXE) analysis using a submillimeter-sized beam (submilli PIXE).

NFSa fibrosarcoma cells[3)] (5×10^6/50 mL) were transplanted into hind limbs of C3H/HeSlc male mice aged 11-14 weeks old. When tumor diameters reached around 10 mm, AVE8062 dissolved in 0.9% saline at a concentration of 5 mg/mL was injected i.p. at a single dose of 40 mg/kg to the mice. The mice were sacrificed by cervical dislocation 24 hours after AVE8062 administration, and the tumors were excised and immediately frozen with powdered dry ice. The tumors were stored at −80°C until sample preparation.

In order to evaluate the spatial distributions of principal elements in the tumor tissue treated with AVE8062 using the submilli PIXE analysis, we obtained tissue section samples by cutting the frozen tumors in a cryostat (-20°C) (MICROM HM 500) and mounted them on 4 μm-thick prolene films attached on target holders. We used thick tissue sections to obtain statistically improved elemental maps. When cutting the frozen tumor, we determined thickness of the tissue section so that the X-ray yield rates of heavier elements such as Fe and Zn was maximized. As a result, the thickness of the tissue section was 250 μm. The tissue sections were dried and stored at -80°C until the PIXE analysis was performed.

A 3-MeV proton beam was provided from a single-ended Dynamitron accelerator. The tissue section samples in dry state were irradiated in air by a beam scanning technique using two dipole magnets. The proton beam was delivered to the target through a 12.5 mm Kapton window. The beam spot size was about 0.5 mm (FWHM) and the beam intensity was 2nA on target. Energies of X-rays from the samples were measured using a Si(Li) detector (10 mm^2 active area) with a 7.5 mm Be window for low energy measurements and a Si(Li) detector (60 mm^2 active area) with a 12.5 mm Be window for high energy measurements. The detectors for low-energy and high-energy X-ray measurements were located at -135° and 135°, respectively, with respect to the beam direction. In addition, the high energy detector was mounted with a sheet of 700 mm thick Mylar film to remove low energy X-rays. Elemental maps of principal elements in the tissue section were obtained from the least-squares fitting analysis of energy spectra using the quantitative PIXE imaging and analysis software GeoPIXE II4). Details of the submilli-PIXE system used in this work have been described in ref. 5.

We could evaluate the distributions of phosphorus, sulfur, potassium, calcium, iron and zinc in the tumor samples, as shown in Figs. 1 and 2. When compared to the results of the control tumor, it was found that AVE8062 treatment made significant differences in their spatial distributions between the untreated and treated tumors as is the case in the cross-sectional images. Although the principal elements appear to be distributed uniformly in the tissue section of the control tumor, potassium, calcium and sulfur concentrations can be seen at the periphery of the treated tumor. The analysis is currently in progress.

This work was supported by Grants-in-Aid for Scientific Research (B) Nos. 17300169 (A. Terakawa) and 20300174 (A. Terakawa), and by Exploratory Research No. 19650128 (A. Terakawa) of the Ministry of Education, Culture, Science, Sports and Technology.

References

1) Ohsumi K. et al., *J. Med. Chem.* **41** (1998) 3022.
2) Ohsumi K. et al, *Anti-Cancer Drug Design* **14** (1999) 539.
3) Jibu Tatsuo, et al., *Clin. Exp., Metastasis*, **11** (1993) 306.
4) Ryan C. G., et al., *Nucl. Instr. and Meth.* **B 188** (2002) 18.
5) Matsuyama S., *Int. journal of PIXE* **8** (1998) 209.

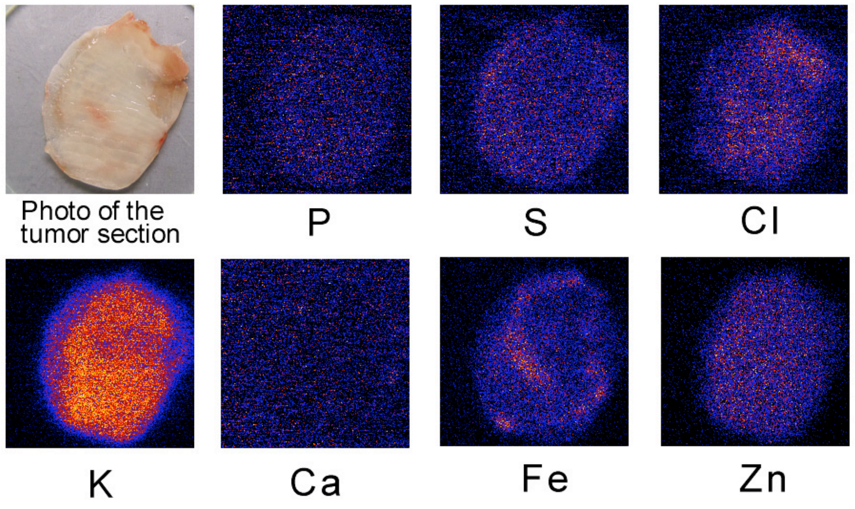

Figure 1. Distributions of principal elements in the tissue section of the untreated NFSa tumor evaluated from in-air submilli-PIXE analysis.

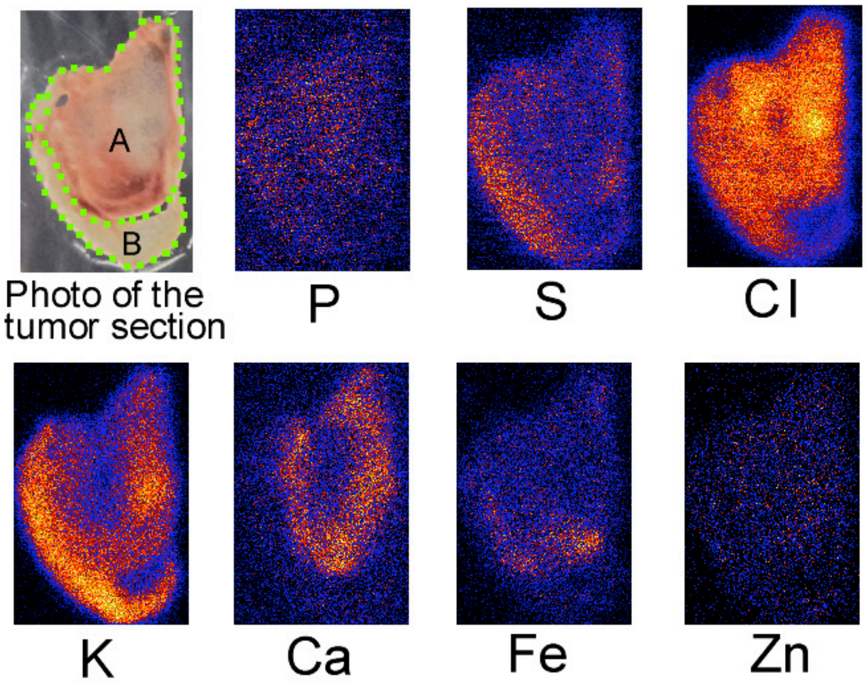

Figure 2. Distributions of principal elements in the tissue section of the AVE8062-treated NFSa tumor evaluated from submilli-PIXE analysis. The photograph of the section also indicates tissue regions (inner region (A) and peripheral region (B)) used as samples for conventional PIXE analysis.

V. 2. Application of Micro-PIXE Analysis to Investigate Trace Elements in Deciduous Teeth Enamel

Igari K.[1]*, Takahashi A.*[1]*, Ando H.*[1]*, Ishii K.*[2]*, Matsuyama S.*[2]*, Kawamura Y.*[2]*, Ohkura S.*[2]*,*
Hashimoto Y.[2]*, Fujikawa M.*[2]*, Itou Y.*[2]*, Fujiki K.*[2]*, Hatori Y.*[2]*,*
Hamada N.[2]*, and Yamazaki H.*[3]

[1]*Dental Clinic for the Disabled, Tohoku University Hospital Dental Center,*
[2]*Department of Quantum Science and Energy Engineering, Tohoku University,*
[3]*Cyclotron and Radioisotope Center, Tohoku University*

Introduction

In Japan, it has been reported that the mean birth weight is decreasing gradually and the babies with low birth weight are increasing during recent two decades1). These phenomena are related to maternal low dietary intake and/or cigarette smoking. There is a possibility that deficiency and/or excess of major elements and trace elements in fetus have occurred resulting from exposure to low dietary and cigarette smoking.

Deciduous tooth enamel commences calcification at the end of the first trimester in utero and continues to develop up to a year after birth. The neonatal line which is found in all deciduous teeth represents the time of birth and the border line between prenatal enamel and postnatal enamel. Mature enamel contains no active cells and its chemical composition reflects the status of metabolism of trace elements during formation period. Therefore, deciduous tooth enamel is a suitable indicator of trace element exposure in utero.

In previous studies, flame atomic absorption spectroscopy, inductively coupled plasma emission and mass spectrometry were often used to measure trace element concentration2,3). These analytical methods need bulk techniques in which whole teeth or some portion of enamel is digested in a suitable mineral acid. Because enamel tissue is destroyed in this technique, we cannot know the time-based elemental distribution profiles. However, in micro-PIXE analysis, tooth enamel samples are used without destruction, multiple trace elements concentration are measured at the same time, and the distribution of trace elements and their magnitudes can be seen on color maps of scanning area. In this study, trace elemental intake during pre- and post-natal development were measured on deciduous tooth enamel sections using micro-PIXE analysis.

Material and methods

Two deciduous canines from one healthy Japanese child were used for this study. These teeth were caries free and extracted at the age of eight years because of pre-shedding mobility. Each tooth crown was embedded in dental resin, and sectioned in the labio-lingual plane that passed through the cusp tip. The 100 μm thick un-decalcified section was cut from the one half-tooth section. The location of neonatal line was confirmed in the each thin section using an optical microscope. The sample for micro-PIXE analysis was prepared as an enamel section including both pre- and post-natal enamel which identified by neonatal line. The surface of section was coated with carbon.

Analysis of samples was carried out with the microbeam analysis system at Tohoku University[4,5)]. Two X-ray detectors for high energy and low energy were used. Sample was set the enamel surface parallel to the direction of microbeam to reduce edge effect. A Mylar filter (600 μm thick) was attached in front of the high energy X-ray detector to reduce pile-up events. The beam scanning area was set to 0.4×0.4 ~ 1×1 mm^2, and the beam spot size of 2×2 μm^2. Averaged beam current was ca. 150 pA. Measurement time was around 1 hour. The elemental maps were obtained using the GeoPIXE software[6)]. For correct calculation, the major composition and density of the layer must be set. The layer is presumed to be hydroxyapatite ($Ca_5(PO_4)_3(OH)$) of 100 μm thickness, with a density of 3.15 g/cm^3[7)].

Ethics approval for this study was obtained from the Ethics Committee of Tohoku University Graduate School of Dentistry.

Results of analyses

Neonatal line (NNL) was identified on enamel section (Fig. 1). In Fig. 1, the enamel lying under the neonatal line was considered to be postnatal enamel and the upper part to be prenatal enamel. The embedding material layer is shown out of tooth sample.

Typical X-ray spectra measured by the detectors for low and high energies are shown in Fig. 2. Besides calcium (Ca) and phosphorus (P) which were main contents of enamel, sodium (Na), magnesium (Mg), chlorine (Cl), zinc (Zn), and strontium (Sr) were detected. The elemental maps obtained by scanning this section are shown in Fig. 3. X-ray maps of Na and Sr were uniform over an area of the tooth sample. Ca, P, Mg, Cl and Zn showed different distribution between enamel and dentin. Elemental concentrations of Ca and P were higher in enamel than in dentin. On the other hand, elemental concentration of Mg in dentin was slightly higher than in enamel. The concentrations of these three elements were uniform within each tissue (enamel and dentin). Whereas, distribution profiles of Cl and Zn were specific and showed higher concentration in surface enamel. Accumulation of Zn was observed in the most outer layer of enamel. Unfortunately, no elements showed different profiles of X-ray maps between prenatal enamel and postnatal enamel.

Discussion

Thirty-five trace elements have been reported to be present in sound enamel of permanent teeth with wide range8). Twelve elements (Ca, Cu, Mg, Zn, Sr, Al, Ba, Pb, U, Ce, La and Pr) have been found in the deciduous teeth from Ugandan and UK children2). Shashikiran et al.3) showed the presence of 18 elements (F, Sr, K, Al, Si, Ni, B, Fe, Cu, Mn, Co, Cr, Zn, Mg, Se, Pb, Mo and V) in sound and carious enamel of primary and permanent teeth. All of elements detected in this study have been already found in sound deciduous enamel. Lead (Pb) which was found in the teeth from Ugandan and UK children2) (1.21ppm and 1.33ppm, respectively), from Indian children3) (<0.1ppm), and from Mexican children9) was under detection limit in the enamel section from Japanese child in this study. The detection limit was ca. 9ppm in this study. The sensitivity of Pb in the present measurement was lower than that in the other measurements used in the previous studies. However, Pb concentrations shown in those studies were not measured in prenatal or postnatal enamel but in whole tooth crown or enamel powder.

There are few studies described about the distribution of trace elements in enamel. In this study, we obtained the specific distribution profiles of some elements by micro-PIXE analysis. The distribution of Zn, showed the accumulation in enamel surface area. This result was different from the result of Kang's study10) using LA-ICP-MS in which zones of enhanced Zn intensities was seen along the neonatal line. Some elements including Pb have been demonstrated high levels in surface enamel area. However, it is needed to be considered that some events occurring at enamel surface, like oral exposure, de/remineralization, and chemical adsorption/absorption, complicates enamel chemistry in surface enamel area. Zn is considered to be one of important elements for estimating the environment in utero.

The location of neonatal line identified on the optical microscope image was useful to identify the location of neonatal line on the corresponding distribution map. Unexpectedly, the change of distribution profile around neonatal line was not obvious on all elemental concentration maps. The child in this study was healthy and had no special event around birth time. Therefore, the difference between prenatal enamel and postnatal enamel might not be detected.

Conclusions

This study showed the presence of 5 trace elements (Na, Mg, Cl, Zn, and Sr) in the sound enamel including pre- and post-natal enamel of deciduous teeth. Furthermore, we could obtain the distribution maps of these elements with specific profiles. Although no elements detected the difference of distribution profiles between prenatal enamel and postnatal enamel in this sample from healthy child, it was suggested that this analytical methods using micro-PIXE would be able to estimate the trace elements in prenatal and postnatal enamel, respectively.

Acknowledgement

This study was supported by Grant-in Aid for Scientific Research (21610002).

The authors would like to acknowledge the assistance of Fujisawa M. for maintenance and operation of the Dynamitron accelerator.

References

1) Gluckman P.D., Seng C.Y., Fukuoka H., Beedle A.S., Hanson M.A., Lancet **369** (2007) 1081.
2) Brown C.J., Chenery S.R.N., Smith B., Mason C., Tomkins A., Roberts G.J., Sserunjogi L., Tiberindwa J.V., Arch. Oral Biol. **49** (2004) 705.
3) Shashikiran N.D., Subba R.V.V., Hiremath M.C., Indian J. Dent. Res. **18** (2007) 157.
4) Matsuyama S., Ishii K., Yamazaki H., Barbotteau Y., Amartivan Ts., IzukawaD., Hotta K., Mizuma K., Abe S., Oishi Y., Rodriguez M., Suzuki A., Sakamoto R., Fujisawa M., Kamiya T., OikawaM., Arakawa K., Imaseki H., Matsumoto N., Int. J. of PIXE **14** (1&2) (2004) 1.
5) Matsuyama S., Ishii K., Abe S., Ohtsu H., Yamazaki H., Kikuchi Y., Amartaivan Ts., Inomata K., Watanabe Y., Ishizaki A., Barbotteau Y., Suzuki A., Yamaguchi T., Momose G., Imaseki H., Int. J. of PIXE **15** (1&2) (2005) 41.
6) Mayer M., SIMNRA Users's Guide, Technical Report IPP 9/113, MPI Plasmaphy.
7) Bird M.J. et al., J. Dent. Res. **19** (1940) 413.
8) Losee F.L., Cutress T.W., Brown R., Caries Res. **8** (1974) 123
9) Kang D., Amarasiriwardena D., Goodman A.H., Anal. Bioanal. Chem. **378** (2004) 1608.
10) Gomes V.E., Rosario de Sousa M.L., Barbosa J.F., Krug F.J., Pereira M.C., Cury J.A., Sci. Total Environ. **320** (2004) 25.

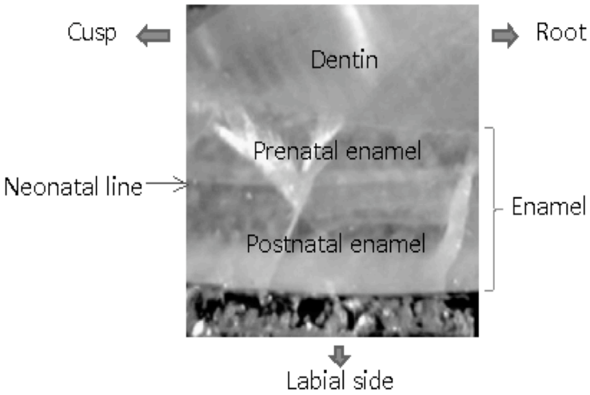

Figure 1.　Enamel section.

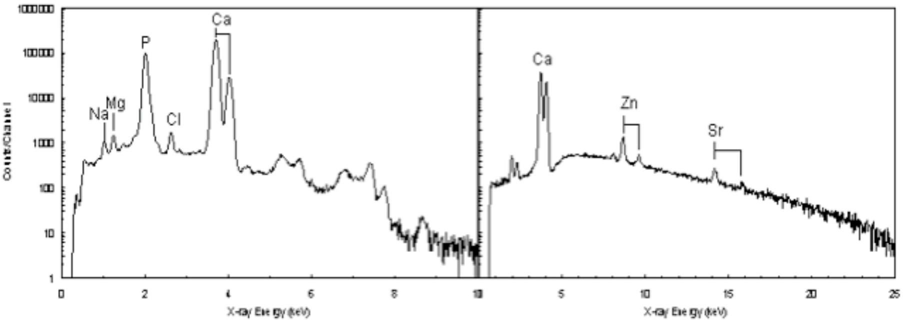

Figure 2.　Typical X-ray Spectra Measured by the Detectors for Low and High Energies.

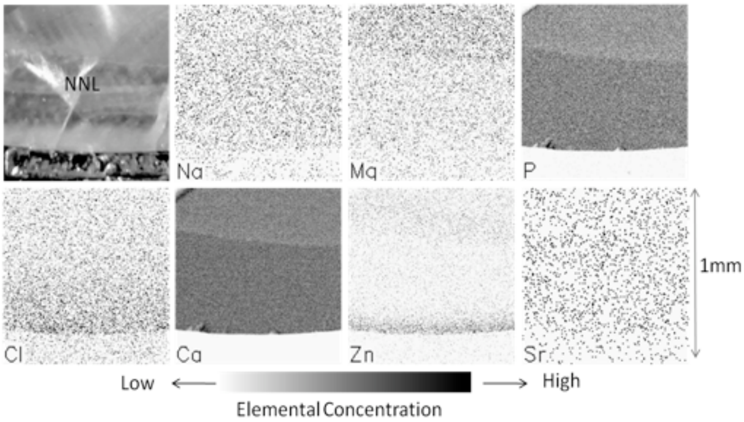

Figure 3.　Elemental maps of the elements.

V. 3. Microbeam Analysis of Individual Particles in Working Environment

Matsuyama S.[1], Catella G.[1], Ishii K.[1], Terakawa A.[1], Kikuchi Y.[1], Kawamura Y.[1], Ohkura S.[1], Fujikawa M.[1], Hamada N.[1], Fujiki K.[1], Hatori Y.[1], Ito Y.[1]. Yamazaki H.[2], Hashimoto Y.[2], Žitnik M.[3], Pelicon P.[3], and Grlj N.[3]

[1]Department of Quantum Science and Energy Engineering, Tohoku University
[2]Cyclotron Radioisotope Center, Tohoku University
[3]Jožef Stefan Institute Jamova 39, SI-1000 Ljubljana, Slovenia

Introduction

Atmospheric aerosols affect large impact on environment and human health and many studies are carrying out[1,2)]. Human beings living in developed countries spend from 80 to 90% of their time in buildings. Therefore indoor aerosols at house and in working environment can have a large impact on human health and aerosol monitoring in working environment is very important for human health. Especially, in machine workshops and laboratories, where specific materials and chemicals are processed, toxic aerosols may be released into air. Therefore, an aerosol monitoring in working environments is one of the essential prerequisites for an efficient health protection system for the employees.

Aerosol particles are characterized by various physical and chemical factors. The elemental analysis of atmospheric aerosols is very important too, since distribution of different elements reflects the sources and their generating processes. Aerosol sampling on thin films and a subsequent PIXE elemental analysis is one of the most effective combinations for studying atmospheric aerosols[1)]. Such an approach is advantageous for aerosol monitoring purposes because the elemental concentrations can be studied with a reasonable time resolution[3,4)]. However, in bulk analysis, the elemental concentrations are averaged over many individual particles which have different origins. Therefore, individual particle analysis is superior to bulk analysis for obtaining source-related information and for understanding the aerosol formation mechanisms[5,6)]. In the previous study, the aerosols collected by a cascade impactor set in the machine workshop of Jožef Stefan Institute were characterized by a bulk PIXE analysis and a multimodal microanalysis with microscopic scanning[7]. While we could provide an efficient aerosol monitoring capability, the source identification was not performed completely. This study deals with in-doors aerosols that were collected in the machine workshop of Jožef Stefan Institute. The samples were reanalyzed by a microbeam analysis system at Tohoku University with a superior resolution and source identification was carried out.

Sampling and analysis

Aerosol particles were collected inside the machine workshop of Jožef Stefan Institute, Slovenia using a nine-stage cascade impactor (Model 1-1L; PIXE international Co. LTD). The machine workshop has three rooms: workshop room, preparation room and carpentry room, as described in the previous paper[7]. A non-stop sampling in the workshop room with the cascade impactor was conducted during two time intervals corresponding to weekdays (working regime, February 13-15, 2008) and weekend (non-working regime, February 15-18). The averaged air flow rate was 1.2±0.1 *l*/min and the aerosol particles were captured on a 2 μm thick Mylar film

The sample analysis was carried out with the microbeam analysis system at Tohoku University. Technical details of the system were presented in previous papers[5,8,9]. For multimodal analysis, two X-ray detectors for PIXE analysis and two charged particle detectors for RBS and off-axis STIM were mounted to observe the sample simultaneously. A simultaneous set of PIXE / RBS / off-axis STIM spectra was accumulated upon irradiation of the sample by a 3 MeV proton beam with the 1×1 μm^2 beam spot size and 50-100 pA beam current. The beam scanning area was set to between 40×40 to 100×100 μm^2 for individual particle analysis, Elemental maps were obtained by GeoPIXEII software[10]. After generating the elemental maps, individual particles were selected from these maps and corresponding PIXE, RBS, and off-axis STIM spectra were extracted and analyzed. Concentrations of carbon, oxygen, and hydrogen were derived from peak yields of extracted RBS and off-axis STIM spectra. Samples collected on stages 2 and 3 in non-working regime were analyzed.

Results

In the previous measurement, congregation of the particles, wider scanning area of 200×200 μm and low counting statistics restricted individual particle analysis[7]. By measuring the area where there are less particles accumulated and using a smaller scanning area, the individual particles could be identified and the distribution of particle specific elements could be determined. In non-working regime, elemental concentrations of Zn, Ba, and Pb were more than ten times higher than in working regime, which was related the restoration of an old white painted wooden door7). In total, 49 particles were analyzed for the non-working regime. Carbon and oxygen are major components of these particles. Forty six particles out of 49 particles could be grouped in three main categories: Ba-rich, Pb-rich and Ca+Fe rich particles, as shown in Fig. 1. During particle collection by the cascade impactor, a time-resolved sampling using the 2D time step sampler was also carried out. The 2D time step sampler data displayed a strong correlation between Ba, Pb and Zn, meaning that these particles certainly have the same origin, and the corresponding analysis will be published in a separate paper. However, the individual particles show no correlation between these three elements. On the contrary, the sets of particles containing Ba and Pb are rather complimentary. Zinc is equally distributed between Ba-rich particles and Pb-rich particles. Figure 2 shows correlations among Ba, Zn and S. These elements are well correlated and it is estimated that the signal is produced by a mixture of $BaSO_4$ and ZnS. Amounts of S are more than those obtained from stoichiometric ratio, which is explained by the mixture. In fact, the combination of $BaSO_4$ and ZnS is used as white pigment for paints and is called lithopone. Apparently, these elements are related to restoration of the door.

Figure 3 shows the correlation among Pb, Cl and O. High concentrations in Cl and its correlation to lead indicate that lead is also present under the form of Patteson’s white lead $PbCl_2$. No clear correlation between Pb and O can be drawn from the graph of Pb in function of O, as organic matter is present in significantly large quantities. Whereas Pb, Zn and Ba are usually found in smaller particles, the removal of the old paint layer also explains that these elements are contained in larger particles, as they were here generated by grinding, and not by nucleation.

Although the results are not shown due to the lack of space, Ca and P are well correlated for the particles that contain high weight percentages in phosphor. Atomic ratio of Ca:P is 1.7. While the high amount of organic matter makes it impossible to determine the compounds, the compound might be $Ca_3(PO_4)_2$.

Conclusions

In-doors aerosols collected in the machine workshop of Jožef Stefan Institute were reanalyzed by a microbeam analysis system a Tohoku University. By measuring smaller sample area with low particle density, the individual particles could be identified. In total, 49 particles were analyzed on sample collected during the non-working regime. Looking at the correlation pattern of different elements in individual particles, the source of aerosol particles could be identified. The detected Ba-Pb-Zn correlation is related to a removal of an old paint layer by grinding, contained under the chemical state of Patteson's white lead $PbCl_2$, and the mixture of $BaSO_4$ and ZnS, known as the pigment called Lithopone. We demonstrated the capability of individual particle analysis to identify the source of these particles. Thus individual particle analysis is applicable to find the aerosol source.

Acknowledgments

This study was supported by JSPS and MHEST under the Japan-Slovenia Research Cooperative Program. The authors would like to acknowledge the assistance of Fujisawa M. for maintenance and operation of Dynamitron accelerator. The authors would like to thank Mrs. Nagaya T. and Komatsu K., for their assistance in constructing the microbeam and target system.

References

1) Johansson S. A. E., Campbell J. L., PIXE:A Novel Technique for Elemental Analysis, John Wiley and Sons (1988).
2) Kasahara M., Park J. H. and Yamamoto K., Nucl. Instr. and Meth. **B109/110** (1996) 471.
3) Prati P., Zucchiatti A., Lucarelli F., and Mandò P. A., Atmospheric Environment **34** (2000) 3149.
4) Formenti P., Annegarnand H. J., Piketh S. J., Nucl. Instr. and Meth., **B136-138** (1998) 948.
5) Matsuyama S., Ishii K., Yamazaki H., Kikuchi Y., Amartaivan Ts., Abe S., Inomata K., Watanabe Y., Ishizaki A., Oyama R., Kawamura Y., Suzuki A., Momose G., Yamaguchi T., and Imaseki H., Int. J. of PIXE, **15** (3&4) (2005) 257.
6) Matsuyama S., Ishii K., Yamazaki H., Kikuchi Y., Kawamura Y., Oyama R., Yamanaka K., Yamamoto T., Watanabe M., Tsuboi S., and Arao K., X-ray Spectrometry, **37** (2008) 151.
7) Matsuyama S., Ishii K., Yamazaki H., Kikuchi Y., Amartaivan Ts., Abe S., Inomata K., Watanabe Y., Ishizaki A., Oyama R., Kawamura Y., Suzuki A., Momose G., Yamaguchi T., and Imaseki H., Int. J. of PIXE, **18** (3&4) (2008) 199.
8) Matsuyama S., Ishii K., Yamazaki H., Barbotteau Y., Amartivan Ts., Izukawa D., Hotta Mizuma K. K., Abe S., Oishi Y., Rodriguez M., Suzuki A., Sakamoto R., Fujisawa M., Kamiya T., Oikawa M., Arakawa K., Imaseki H., Matsumoto N., Int. J. of PIXE, **14** (1&2) (2004) 1.
9) Matsuyama S., Ishii K., Yamazaki H., Kamiya T. et.al., Nucl. Instr. and Meth., **B260** (2007) 55.
10) Ryan C. G., E.Van Achterbergh, Yeats C.J. et.al., Nucl. Instr. and Meth., **B188** (2002) 18.

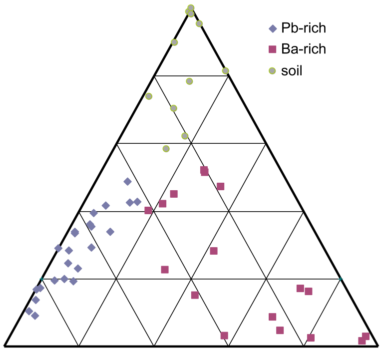

Figure 1. Ternary diagram of the three main groups.

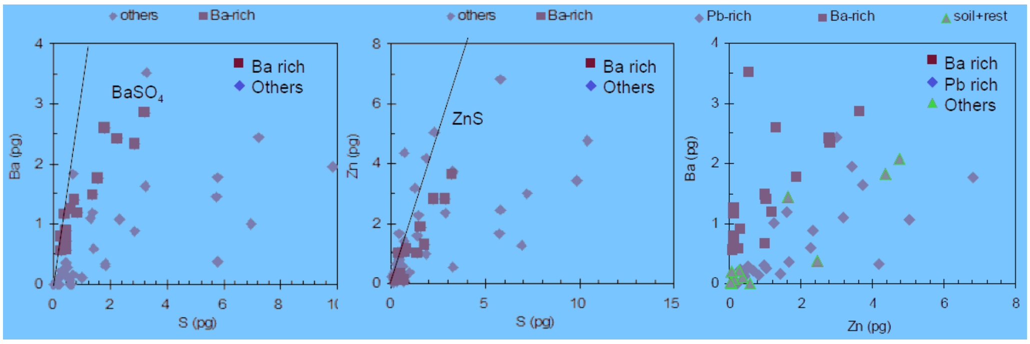

Figure 2. Correlation among Ba, Zn and S concentrations in individual particles.

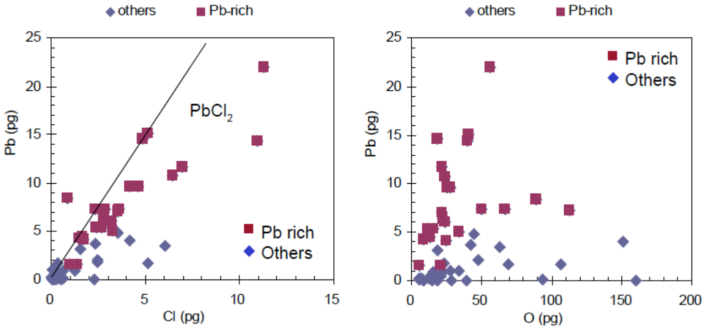

Figure 3. Correlation among Pb, Cl and O.

V. 4. Recent Application of Tohoku Microbeam System

Matsuyama S.[1], Ishii K.[1], Yamazaki H.[1], Kikuchi Y.[1], Inomata K.[1], Watanabe Y.[1], Ishizaki A.[1], Oyama R.[1], Kawamura Y.[1], Yamaguchi T.[1], Momose G.[1], Nagakura M.[1], Takahashi M.[1], and Kamiya T.[2]

[1]Department of quantum science and energy engineering, Tohoku University
[2]Takasaki Advanced Radiation Research Institute, Japan Atomic Energy Agency

Introduction

High energy ion microbeam is a powerful analytical tool by combining various ion beam analysis techniques such as PIXE, RBS, STIM and SEM1-3) and is also attractive as a direct lithographic technique. A microbeam system was constructed at the Tohoku University Dynamitron laboratory for biological applications in a sub-micron resolution. The first purpose is to develop a 3D micron CT, where microbeam is used as a monoenergetic point X-ray source. The second is to develop microbeam analysis system for biological samples. The microbeam line was installed in July 2002 and optimization of the system has been performed. A measured beam spot size of 0.4×0.4 μm^2 at a beam current of 20 pA is currently being obtained. This paper describes recent applications of Tohoku microbeam system.

Microbeam and analysis system

The microbeam system was designed to achieve sub-micron beam sizes and was developed in collaboration with a domestic company (Tokin Machinery Corporation)4). The system is connected to the 4.5 MV Dynamitron accelerator at Tohoku University. To achieve sub-micron beam seizes, a high resolution energy analysis system is installed upstream of the microbeam line. The microbeam line is composed of a quadrupole doublet, three slits systems of microslits (MS), divergence-defining slits (DS) and baffle slits (BS). These components are mounted on a heavy rigid support with vibration isolation. The microslits (MS) define the object size and are composed of two wedge-shaped slits. The divergence-defining slits (DS) define beam divergence into the quadrupole doublet and placed 3 m downstream of the MS. As for the quadrupole magnet, the bore radius is 5 mm and dimensions of the yoke are 60 mm long×220 mm outside diameter. An iron piece of the magnet with poles and yoke was cut as one body using a computer numerically controlled machine to reduce mechanical irregularities causing sextupole contamination4). The demagnification factors are 9.2 and 35.4. The focused microbeam is scanned across a target by using an electrostatic beam scanner.

The target chamber is a rectangular box and applicable to either in-vacuum or in-air analysis without changing the main body. For multimodal analysis, two X-ray detectors and three charged particle detectors can be mounted simultaneously5-7). For 3D micron CT, a CCD, a rotating sample stage and a target to produce X-rays are also mounted on this chamber8-10).

Recent application of the microbeam system

The microbeam analysis system at Tohoku University is routinely applied to various fields. Typical applications are presented.

Aerosol study

Elemental analysis of atmospheric aerosol is useful for source identification and for study of its formation mechanism. These studies were carried out by analyzing bulk samples thereby averaging over many single particles. Therefore, analysis of single aerosol particles is superior to bulk analysis. Our system can quantify single aerosol particles containing from hydrogen to heavy metals and reveal chemical composition of these particles8). The microbeam system was applied to the analysis of yellow sand dust particles. These particles were impacted on a thin polycarbonate film developed for this purpose. Yellow sand dust particles from the Asian continent sometimes cause turbid conditions in Japan especially in spring. Typical elemental images of yellow sand dust particles are shown in Fig. 10.

The elemental distribution of Al is similar the one of Si and Oxygen, originating mainly from soil dust of Alumino-Silicate particles. Distribution of hydrogen is clearly seen and equal to the one of Ca. These particles are sometimes deformed by mixing with anthropogenic aerosols. Then the system will be useful to study these deformation processes.

Cell analysis

An in-air simultaneous PIXE, RBS and a consecutive STIM analysis is a powerful tool for analysis of single cell and tissue section in biological and biomedical research. We have developed an in-air micro-PIXE system in collaboration with the Japan Atomic Energy Agency (JAEA), Takasaki[11,12) and has applied to various kind of cells[13-15). Our in-air analysis system is also focused on this purpose[7). While in-air analysis reduces the damage during beam irradiation[16), morphological change has occasionally occurred by beam irradiation, and cell thickness or density is reduced to ~60 % of the initial value[7). In this case, density of the cell should be monitored simultaneously with analysis and correction of X-ray self absorption should be done according to irradiation dose. On/off-axis STIM enables to perform simultaneous density imaging in PIXE and RBS analysis. Figure 12 showselemental maps of cells and density map measured by the new in-air system. Distributions of P, S, Cl and K elements are clearly seen and correspond to the density. Changes in cell density during the beam irradiation can be monitored and will be effective in cell analysis.

Proton beam writing

Proton beam writing was realized by scanning the microbeam with a corresponding scanning pattern translated from a bitmap file. He spacing between pattern to pattern was made by moving the beam at the fastest speed of the beam scanner. Details of the system will be written elsewhere. Typical pattern written on a Mylar film is shown in Fig. 13. While this pattern was written before removing the field contamination from the annular detector, shape of Japan Island are clearly seen. We are planning to use this technique for an efficient analysis by combining STIM image.

3D-micron CT

3D micron CT is composed of a point X-ray source, a rotating sample stage and a high-speed X-ray CCD camera. The details of the 3D micron CT and applications are written precisely in refs 9, 10, 11. Microbeam is used as a monoenergetic μ X-ray source by bombarding pure metals. 2D transmission data are obtained by rotating the sample encapsulated in a micron tube. 3D images were reconstructed from the obtained transmission data. 3D images of living ant's head were obtained by this system with the spatial resolution of 6 μm. Typical CT image of ant's head is shown in Fig. 14. Since our micron CT uses monoenergetic low energy X-rays, contrast of the image for small insects is superior to that of other CT system. Furthermore, our system can easily change X-ray energy to get better contrast depending on the elements contained in the insects. This system can measure small insects of ~2 mm *in-vivo* and will be useful in the biological field.

Conclusion

A microbeam system was constructed at the Tohoku University Dynamitron laboratory and optimization of the system has been carried out. Minimum beam spot size of the microbeam was saturated at 1.5×1.5 μm^2 by parasitic field contamination. This parasitic field contamination was ascribed to the tungsten carbide slits and the annular Si surface barrier detector in the case of RBS analysis. By replacing these components, the parasitic field contaminations of the system were greatly reduced, which was confirmed by the grid shadow method, and the performance of the microbeam system was improved. Minimum beam spot size of 0.4×0.4 μm^2 at a beam current of several ten pA is being obtained which is the optimum expected from the accelerator performance. The results obtained by the grid-shadow method show that a beam spot size less than 0.4 μm can be obtained in the low current range.

For an easy tuning and an operation of the microbeam system, the human-machine interface of the control system has been developed based on the user participatory design concept. The operational log of a skilled operator has been utilized to realize the HMI, which is user-friendly and has higher usability both for novice and experienced users. The new HMI has been favorably accepted by the users and is utilized in routine operations.

While improving the microbeam system, simultaneous in-air/vacuum PIXE, RBS, SEM and STIM analysis and 3D micron CT are developed and are now being applied to biology and other fields.

Acknowledgement

This study was partly supported by Grant-in-Aid for Scientific Research (S) No. 13852017, Grant-in-Aid for Scientific Research (B) No. 18360450, Grant-in-Aid for Scientific Research (C) No. 16560731 and Grant-in-Aid for Scientific Research in Priority Areas under Grant No.14048213 from the Ministry of Education, Culture, Sports, Science and Technology, Japan. The authors would like to thank Prof. Jamieson D. N., the

University of Melbourne, for his valuable suggestions and advice in reducing field contaminations and introducing the computer codes PRAM and OXTRACE. The authors would like to acknowledge the assistance of Mr. Sakamoto R. and Fujisawa M. for maintenance and operation of the Dynamitron accelerator. The authors would like to thank Mr. Komatsu K., Nagaya T., and Akama C. for their help in constructing the microbeam and target system.

References

1) Watt F., Grime G. W., Principal and Applications of Highenergy Ion Microbeams, Adam Hilger, Bristol, 1987.
2) Johansson S. A. E., Campbell J. L., Malmqvist K. G., Particle-Induced X-ray Emission Spectrometry (PIXE), John Willey and Sons, N.Y., 1995.
3) Breese M. B. H., Jamieson D. N., King P. J. C. , Materials Analysis using Nuclear Microprobe, John Willey and Sons, N.Y., 1995.
4) Jamieson D. N. and Legge G. J. F., Nucl. Instr. and Meth. B**29** (1987) 544.
5) Matsuyama S., Ishii K., Yamazaki H., Barbotteau Y., Amartivan Ts., Izukawa D., Hotta Mizuma K. K., Abe S., Oishi Y., Rodriguez M., Suzuki A., Sakamoto R., Fujisawa M., Kamiya T., Oikawa M., Arakawa K., Imaseki H., Matsumoto N., Int. J. of PIXE **14**(1&2) (2004) 1.
6) Matsuyama S., Ishii K., Abe S., Ohtsu H., Yamazaki H., Kikuchi Y., Amartivan Ts., Inomata K., Watanabe Y., Ishizaki A., Barbotteau Y., Suzuki A., Yamaguchi T., Momose G. and Imaseki H., Int. J. of PIXE **15** (1&2) (2005) 41.
7) Matsuyama S., Ishii K., Yamazaki H., Kikuchi Y., Amartivan Ts., Abe S., Inomata K., Watanabe Y., Ishizaki A., Oyama R., Kawamura Y., Suzuki A., Momose G., Yamaguchi T. and Imaseki H., Int. J. of PIXE **15** (3&4) (2005) 257.
8) Ishii K., Matsuyama S., Yamazaki H., Watanabe Y., Yamaguchi T., Momose G., Amartaivan Ts., Suzuki A., Kikuchi Y. and Galster W., Int. J. of PIXE **15** (3&4) (2005) 111.
9) Ishii K., Matsuyama S., Yamazaki H., Watanabe Y., Kawamura Y., Yamaguchi T., Momose G., Kikuchi Y., Terakawa A. and Galster W., Nucl. Instr. and Meth., **A571** (2007) 64.
10) Ishii K., Matsuyama S., Watanabe Y., Kawamura Y., Yamaguchi T., Oyama R., Momose G., Ishizaki A., Yamazaki H., and Kikuchi Y., Nucl. Instr. and Meth.,**B249** (2006) 726.
11) Matsuyama S., Ishii K., Sugimoto A., Satoh T., Goto K., Yamazaki H., Iwasaki S., Murozono K., Inoue J., Hamano T., Yokota S., Sakai T., Kamiya T. and Tanaka R., Int. J. of PIXE **8** (2&3) (1998) 203.
12) Sakai T., Hamano T., Hirao T., Kamiya T., Murozono K., Inoue J., Matsuyama S., Iwasaki S., Ishii K., Nucl. Instr. and Meth., B**136-138** (1998) 390.
13) Ishii K., Sugimoto A., Tanaka A., Satoh T., Matsuyama S., Yamazaki H., Akama C., Amartiva T., Endoh H., Oishi Y., Yuki H., Sugihara S., Satoh M., Kamiya T., Sakai T., Arakawa K., Saidoh M. and Oikawa S., Nucl. Instr. and Meth., B**181** (2001) 448.
14) Sugimoto A., Ishii K., Matsuyama S., Satoh T., Goto K., Yamazaki H. and Akama C., Int. J. of PIXE **9** (3&4) (1999) 151.
15) Tanaka A., Ishii K., Komori Y., Matsuyama S., Satoh T., Goto K., Yamazaki H. and Akama C., Int. J. of PIXE **12** (3&4) (2002) 79.

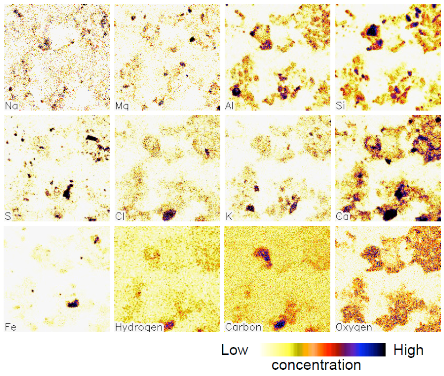

Figure 1. Elemental maps of yellow sand dust particles.

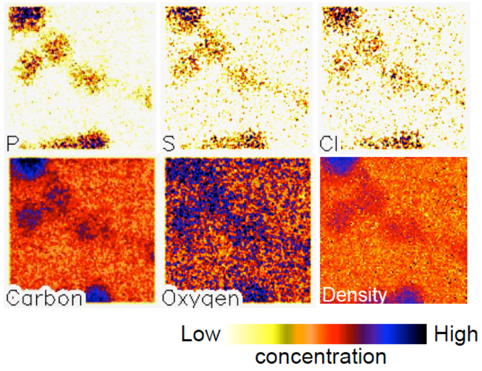

Figure 2. Elemental maps and density distribution of cells.

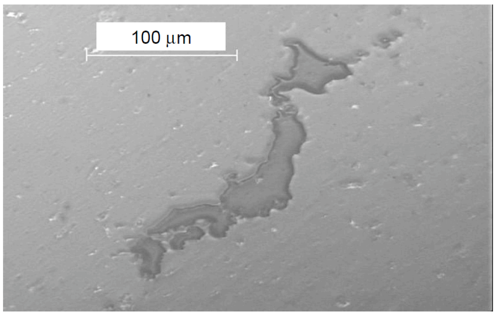

Figure 3. Optical image of pattern written by mictrobeams.

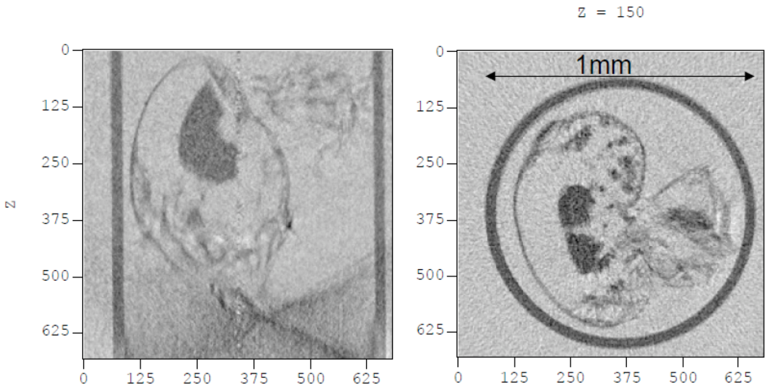

Figure 4. Cross sectional view of ant's head.

V. 5. Improvement of The Performance of Tohoku Microbeam System

Matsuyama S.[1]*, Ishii K.*[1]*, Tsuboi S.*[1]*, Hashimoto Y.*[1]*, Kawamura Y.*[1]*, Yamanaka K.*[1]*,*
Watanabe M.[1]*, Ohkura S.*[1]*, Fujikawa M.*[1]*, Catella G.*[1]*, Fujiki K.*[1]*, Hatori Y.*[1]*,*
Hamada N.[1]*, Fujiwara M.*[1]*, Kikuchi Y.*[1]*, and Yamazaki H.*[2]

[1]*Department of Quantum Science and Energy Engineering, Tohoku University*
[2]*Cyclotron and Radioisotope Center, Tohoku University*

Introduction

High-energy ion microbeams are versatile tools for analyses in a microscopic region[1-3]. A microbeam system was installed at Dynamitron laboratory at Tohoku University in July 2002 for biological applications with sub-micrometer resolution[4]. Beam spot of 0.4×0.4 μm^2 at a beam current of several tens of pA has been produced[5]. The analysis system has also been developed and is applicable to simultaneous in-air/in-vacuum PIXE, RBS, SE, and STIM analyses[6,7], and 3D μ-CT[8-10]. In our set-up, μ-PIXE/RBS analyses demand beam currents of ca. 100 pA, which restricts the spatial resolution to around 1×1 μm^2. Recently, higher spatial resolution down to several hundred nm is required in aerosol studies. In in-vivo 3D imaging using 3D PIXE-μ-CT, we faced two problems: the reconstructed image was blurred due to the movements of the specimen and the long measurement time of several hours weakened the specimen. Thus beam currents higher than several hundred pA are required in 3D PIXE-μ-CT applications. Beam brightness must be increased to meet these requirements. In the previous study, the terminal equipment and an acceleration tube of the Dynamitron accelerator were upgraded. However obtained beam brightness is lower than expected and than that of previous system. As for microbeam system, parasitic field contamination should be eliminated to obtain submicron resolution. While the parasitic field contamination of the system was greatly reduced in the previous study, contamination of the skew sextupole field of ca. 0.1% was still remaining. While the effect of sextupole contamination could be reduced by reducing a half divergence into the quadrupole lenses, which also reduces beam current and is undesirable in our purpose.

In this study, optimization and modification of the ion source and microbeam system were performed to improve the performance.

Improvement of the System

Ion Source

The terminal equipment comprises a duoplasmatron ion source along with an extractor, an Einzel lens, an ExB filter, a pulsing system, and a gap lens, which were provided by National Electrostatics Corporation (NEC), USA. Technical details of the system were presented in previous paper11). The ion source is expected to produce ca. 10 mA H_1^+ beams, with beam emittance of 2.1 mm· mrad· $MeV^{1/2}$ (specification). Both values are better than those of the previous ion source. However, beam brightness after passing the energy analyzing system was 0.44 $pA \cdot \mu m^{-2} \cdot mrad^{-2} \cdot MeV^{-1}$ for H_1^+ beams at half divergence of 0.07 mrad, which was lower than expected and than those of the previous ion source.

In the installation of the system, the ion source was modified to achieve longer lifetime, which is the most important property for an ion source used in the single-ended machine. Figure 1 shows the duoplasmatron ion source and anode aperture assemblies. A LaB_6 filament (C2B, Denka Co. Ltd.) was used instead of an uncoated tungsten filament (0.9 mm diameter) supplied from NEC. A 0.1-mm-diameter anode aperture assembly (expansion cup) made of soft magnetic iron was replaced by different one with 0.3-mm-diameter anode aperture insert made of tungsten (Fig. 1(a)). Outer diameters of the insert are 9.5 mm and 8 mm for source and extractor sides, respectively. The shape and dimension of the assembly are identical to those of original design except for diameter of the aperture. Lower performance might be related to these modifications. Ion beams are extracted through an anode aperture of the duoplasmatron ion source. Shape and diameter of the anode aperture affects beam property. The anode aperture also has functions to shield magnetic field from the source and to close magnetic circuit. Since outer diameters of the previous anode aperture insert were 8 mm and 9.5 mm, shielding of the magnetic field might be insufficient. For this reason, outer diameter of the aperture insert was reduced down to 4 mm (Fig. 1(b)).

Microbeam System

The microbeam system was developed in collaboration with Tokin Machinery Corp and was described precisely in previous papers4,5). A high-resolution energy analysis system is installed upstream of the microbeam line. The microbeam line comprises a quadrupole doublet and three slit systems: micro-slit, divergence-defining slit, and baffle slit. The total length of the line is ca. 7 m. The demagnification factors were 35.4 and 9.2 for horizontal and vertical directions, respectively, which were the highest values in our system(5). At fist, parasitic field contamination from microbeam line components, restricted the resolution. In order to reduce parasitic field contamination, some of those components were replaced or redesigned. However sextupole field contamination superimposed onto the quadrupole field in the horizontal focusing was still remaining. The rigid support of the line made of steel and beam ducts made by stainless steel (SUS304) might be the source. Since the distance between beam line and the rigid support is ca. 25 cm, magnetic field contamination from the support might be dipole and will not affects beam sizes. Strong multipole field contamination from a stainless beam duct (SUS316, outer diameter 10 mm) was reported(12). In our system, the minimum diameter of the beam ducts from micro-slit to baffle-slit is ca. 60 mm and might not cause multipole contamination. However, diameter of the beam ducts from baffle-slit to the target chamber was rather small and might cause multipole contamination. While a beam duct in the quadrupole doublet is the smallest diameter and is made of aluminum, other parts are made of stainless steel (SUS304). Especially, a beam scanner camber was made of stainless steel and was asymmetric design. The outer diameter was 52 mm. The beam scanner chamber was redesigned and was made by aluminum. The chamber was cut as one body from a single aluminum piece to reduce volume. Thus, the demagnification factors are further improved to 40.8 and 9.8 for horizontal and vertical directions, respectively. A bypass line made by stainless steel, which had been used to reduce pressure in the target chamber, laid in parallel to the beam line on the quadrupole doublet. The bypass line was also removed. Realignment of the line was carried out. The target chamber sunk 1.5 mm, which resulted from the increase of mass of analysis system.

The micro-slit comprises two wedge-shaped slits supplied from Technisches Büro S. Fischer, Germany, which were made from 4-mm-diameter and 15 mm long tungsten carbide cylinders whose spacing was increasing linearly from 0–150 μm. Aluminum body of the micro-slit was eroded after several high-current experiments. In order to withstand heat loading to the micro-slit in the high current application, it was redesigned. The diameter of tungsten carbide cylinders set to 5 mm. Pre-slits and a part of the casing were made of tantalum. To extend beam size range from 0 to 6 μm, the spacing is adjustable from 0 to

250 μm corresponding to a longitudinal motion of 0-24 mm.

Performance

Beam brightness

The beam brightness is of primary importance to focus the beam down to sub-micrometer scale with sufficient beam current and has to be measured after passing through the energy analysis system. Then the system's beam brightness was estimated from the target current measurement in the microbeam with the micro-slit opening fixed and divergence defining slit one varied. The micro-slit widths were set at 74×14 μm^2, which correspond to beam spot size of 1.5×1.5 μm^2. Slit opening of the analyzing system was set at 0.6 mm, which is the conventional opening in the analysis mode. Energy resolution of the analyzing system is estimated to be 2.0×10^{-4} ⊿P/P. Figure 2 shows the measured beam brightness before and after modifications. The beam brightness after changing the anode aperture is 0.5 $pA\cdot\mu m^{-2}\cdot mrad^{-2}\cdot MeV^{-1}$ at a half divergence of 0.2 mrad and is 1.6 times higher than before.

As for the microbeam line, the beam brightness became 1.0 $pA\cdot\mu m^{-2}\cdot mrad^{-2}\cdot MeV^{-1}$ at a half divergence of 0.2 mrad and 1.7 times higher than that of the previous ion source. Considering the brightness and the magnification, obtainable target current will be 200 and 900 pA for beam spot sizes of 1.0×1.0 and 2.0×2.0 μm^2, respectively. Normal beam brightness at a half divergence of 0.07 mrad is 1.6 $pA\cdot\mu m^{-2}\cdot mrad^{-2}\cdot MeV^{-1}$ which is only 1.6 times higher than that at a half divergence of 0.2 mrad. It means that the beam intensity distribution in the phase space is uniform.

The ion source and the anode aperture have worked more than 2800 and 1800 hrs, respectively, without changing beam properties and are still running. The modification of the source meets both the lifetime and the performance. However, the brightness is still lower than that expected from the source. Because the anode aperture diameter also affects the brightness, aperture optimization should be done.

Field contamination

In the grid shadow method, the beam is focused on the image plane, where a fine mesh grid is placed, by a single quadrupole lens and casts shadow pattern on a scintillator downstream[14,15]. The shadow pattern is influenced strongly by lens aberration and parasitic field contaminations of the microbeam system. Geometry of shadow pattern measurement was the same as the previous measurements^5). In this measurement, we set the divergence to ±0.35 mrad, which is the largest acceptance of the microbeam line and smaller than that from the accelerator. Figure 3 shows the measured grid shadow patterns for the two quadrupole lenses with a 3 MeV proton beam. The measured shadow patterns are straight and are not deformed. Since the minimum detectable limit corresponds to approximately 0.05% for sextupole field contamination superimposed onto the quadrupole field^5) calculated by the beam optics computer codes, PRAM and OXTRACE^3), field contamination is less than 0.1%. In the previous study, it was suspected that the cancellation of excitation current of the quadrupole is not perfect^5). In this study, no modification was made to the quadrupole. Therefore, the contamination came from the beam scanner and a part of beam line. The Tohoku microbeam system has a capability to focus the beam down as theoretical even in the large half divergence into the quadrupole.

Beam Size

The beam spot size was obtained by fitting the measured line profiles of X-rays from the Au mesh (2000 lines/inch)^6). Slit opening of the analyzing system was set at 0.6 mm and the half divergence was set at 0.2 mrad, which is the conventional opening in the analysis mode. Beam spot sizes diminished concomitant with the object slit sizes and were saturated with ca. 500×500 nm^2, which might be the effect of chromatic aberration.

Figure 4 shows typical example of secondary electron image of carbon steel oxidized under dynamic condition^16). MS widths were set at 20×5 μm^2, which correspond to beam spot size of 0.5×0.5 μm^2 at the half divergence of 0.2 mrad. Changes in secondary electron intensities along grain boundary are clearly seen. From the comparison with the marker indicated in the figure, the spatial resolution is ca. 0.5×0.5 μm^2 and consistent with the estimation. Simultaneous PIXE/RBS analysis could be done.

In the 3D PIXE-μ-CT experiments, beam current of several hundred pA are routinely obtained with the beam spot sizes of ca. 2×2 μm^2 and *in-vivo* 3D imaging is realized. These results will be presented elsewhere.

Conclusions

In order to improve the performance of Tohoku microbeam system, optimization and modification of the ion source and microbeam system were performed. The anode aperture of the duoplasmatron ion source was redesigned and installed. The object slits of the microbeam line was redesigned to withstand higher beam current. The parasitic field contamination of the system was reduced down to less than 0.05% by replacing the beam scanner and a part of beam duct. The beam brightness of the system was 1.0 pA·μm^{-2}·mrad^{-2}·MeV^{-1} at the half divergence of 0.2 mrad and was 1.7 times higher than that of the previous ion source. Considering the brightness and the magnification, obtainable target current will be 200 and 900 pA for beam spot sizes of 1×1 and 2×2 μm^2, respectively at the half divergence of 0.2 mrad. The ion source and the anode aperture have worked more than 2800 and 1800 hrs, respectively, without changing beam properties and are still running. The modification of the source meets both the lifetime and the performance. Deformation of MS is completely reduced by the modification even in the beam load of several μA. Both resolution and beam currents are sufficient for our application and Tohoku microbeam system has been operated routinely for simultaneous in-air/in-vacuum PIXE, RBS, SE, and STIM analyses and for *in-vivo* 3D PIXE-μ-CT imaging.

Acknowledgement

The authors would like to acknowledge the assistance of Fujisawa M. for maintenance and operation of the Dynamitron accelerator. The authors would like to thank Mr. Nagaya T. and Komatsu K., for the modification of the accelerator and microbeam system.

References

1) Watt F., Grime G.W., Principal and Applications of High-energy Ion Microbeams, Adam Hilger, Bristol, 1987.
2) Johansson S.A.E., Campbell J.L., Malmqvist K.G., Particle-Induced X-ray Emission Spectrometry (PIXE), John Wiley and Sons, N.Y., 1995.
3) Breese M.B.H., Jamieson D.N., King P.J.C., Materials Analysis using Nuclear Microprobe, John Wiley and Sons, N.Y., 1995.
4) Matsuyama S., Ishii K., Yamazaki H., Sakamoto R., Fujisawa M., Amartaivan Ts., Ohishi Y., Rodriguez M., Suzuki A., Kamiya T., Oikawa M., Arakawa K., Matsumoto N., Nucl. Instr. and Meth. **B 210** (2003) 59.
5) Matsuyama S., Ishii K., Yamazaki H., Kikuchi Y., Inomata K., Watanabe Y., Ishizaki A., Oyama R., Kawamura Y., Yamaguchi T., Momose G., Nagakura Takahashi M.M., Kamiya T., Nucl. Instr. and Meth. **B 260** (2007) 55.
6) Matsuyama S., Ishii K., Yamazaki H., Barbotteau Y., Amartaivan Ts., Izukawa D., Hotta K., Mizuma, K., Abe S., Oishi Y., Rodriguez M., Suzuki A., Sakamoto R., Fujisawa M., Kamiya T., Oikawa M., Arakawa K., Imaseki H., Matsumoto N., Int. J. of PIXE **14** (1&2) (2004) 1.
7) Matsuyama S., Ishii K., Abe S., Ohtsu H., Yamazaki H., Kikuchi Y., Amartaivan Ts., Inomata K., Watanabe Y., Ishizaki A., Barbotteau Y., Suzuki A., Yamaguchi T., Momose G., Imaseki H., Int. J. of PIXE **15** (1&2) (2005) 41.
8) Ishii K., Matsuyama S., Yamazaki H., Watanabe Y., Yamaguchi T., Momose G., Amartaivan Ts., Suzuki A., Kikuchi Y., and Galster W., Int. J. of PIXE **15** (3&4) (2005) 111.
9) Ishii K., Matsuyama S., Yamazaki H., Watanabe Y., Kawamura Y., Yamaguchi T., Momose

G., Kikuchi Y., Terakawa A., Galster W., Nucl. Instr. and Meth. **B 249** (2006) 726.

10) Ishii K., Matsuyama S., Watanabe Y., Kawamura Y., Yamaguchi T., Oyama R., Momose G., Ishizaki A., Yamazaki H., Kikuchi Y., Nucl. Instr. and Meth. **A 571** (2007) 64.
11) Matsuyama S., Ishii K., Fujisawa M., Kawamura Y., Tsuboi S., Yamanaka K., Wtanabe M., Hashimoto Y., Ohkura S., Fujikawa M., Nagaya T., Komatsu K., Yamazaki H., Kikuchi Y., Nucl. Instr. and Meth. **B 267** (2009) 2060.
12) Jamieson D.N., Nucl Instr and Meth. **B 181** (2001) 1.
13) Roland Szymanski, David N. Jamieson, Nucl. Instr. and Meth. **B 130** (1997) 80.
14) Jamieson D.N., Legge G.J.F., Nucl. Instr. and Meth. **B 29** (1987) 544.
15) Jamieson D.N., Zhu J., Mao Y., Lu R., Wang Z., Zhu J., Nucl. Instr. and Meth. **B 104** (1995) 86.
16) Matsuyama S., Ishii K., Fujiwara M., Kikuchi Y., Nakhostin M., Kawamura Y., Watanabe M., Ohkura S., Hashimoto Y., Fujikawa M., Catella G., Fujiki K., Hatori Y., Hamada N., Tanino S., Abe H., Watanabe Y. Yamazaki H., Int. J. of PIXE **19** (1&2) (2009) 61.

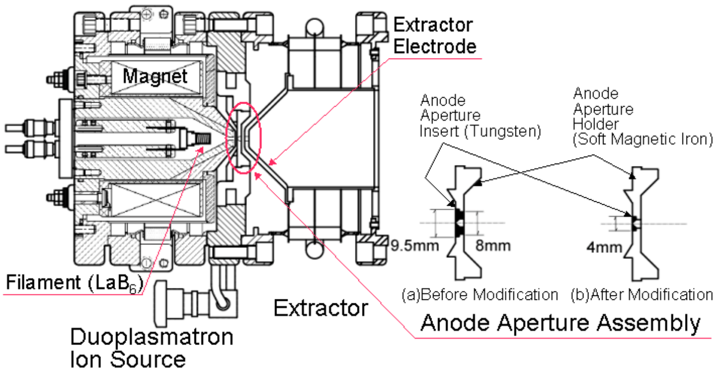

Figure 1. Duoplasmatron Ion Source and Anode Aperture Assembly.

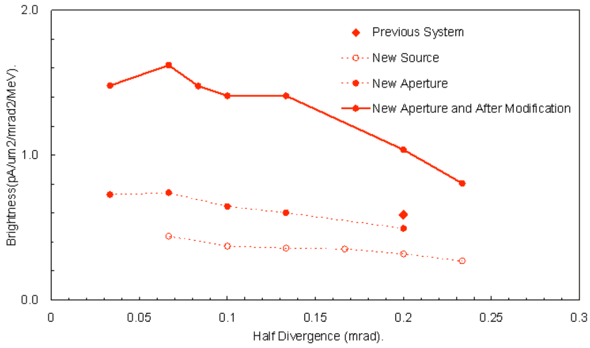

Figure 2. Measured beam brightness.

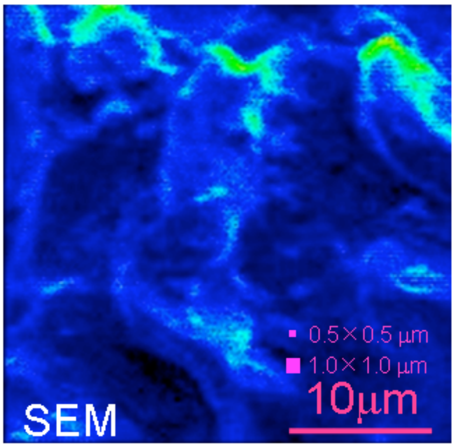

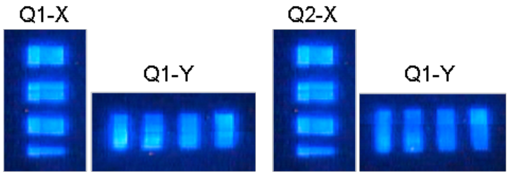

Figure 3. Measured Grid Shadow Pattern.

Figure 4. Secondary Electron Image of Carbon Steel Oxidized under Dynamic Condition.

VI. 1. Development of a Simplified MA Separation Process Using Novel R-BTP Adsorbents – III

Usuda S.[1]*, Kuraoka E.*[1]*, Li Z.*[1]*, Liu R.*[1]*, Xu Y.*[2]*, Kim S.-Y.*[1]*, Wakui Y.*[3]*, Hayashi H.*[3]*,*
Yamazaki H.[1]*, and Ishii K.*[1,2]

[1]*Cyclotron and Radioisotope Center, Tohoku University*
[2]*Graduate School of Engineering, Tohoku University*
[3]*National Institute of Advanced Industrial Science and Technology*

Introduction

For the purpose of minimization of the long-term radiotoxicity and facilitation of the nuclear waste management, numerous efforts have been made for recovery of trivalent minor actinides (MA: Am, Cm *etc.*) from fission products (FP) in the high level radioactive liquid waste (HLLW). Various ligands for extraction process to separate the MA from FP including rare earths (RE) have so far been actively developed1).

As a potential candidate to be used in ≥1 mol/dm^3 [M] HNO_3, new type nitrogen-donor ligands, R-BTP (BTP: 2,6-bis-(5,6-dialkyl-1,2,4-triazin-3-yl)-pyridine, R: alkyl group)2) are widely noticed because the ligands showed high extraction selectivity for Am(III) over RE(III). In addition, the ligands consist of C, H, O and N, which are combustible after use up. Recently, Ekberg *et al.*3) reviewed various nitrogen-donor ligands for extraction and separation of MA(III) from RE(III) and pointed out that the R-BTP solvent extraction system exhibited excellent property mentioned above while the system had slow kinetic rate and stability weakness towards radiolysis and chemical degradation.

In order to overcome the demerits of solvent extraction and to accelerate the merits of R-BTP extractants, an alternative technology of extraction chromatography has been proposed, which uses a minimal organic solvent in compact equipment. Kuraoka (Wei) *et al.* have synthesized several R-BTP/SiO_2-P extraction adsorbents with different alkyl groups, and investigated the fundamental properties4-10). It was found that separation property and stability of the R-BTP adsorbents depended on the structure of alkyls, *i.e.*, number of carbons and different branched chain. Separation factors between Am(III) and Eu(III) (up to ≈100) are relatively high in the case of normal R-BTP adsorbents with straight 3~7 carbon chain[8,9]. On the other hand, the branched R-BTP adsorbent is more stable than normal R-BTP ones in ≤3 M HNO_3 solution[6,8].

The objective of this work is to establish a simplified MA separation process by using single column packed with a new type of R-BTP adsorbents. In the fiscal years (FY) 2008 and 2009, *iso*hexyl-BTP (R: 4-methylpentyl) (see Fig. 1) and *iso*heptyl-BTP (R: 3-methylhexyl) adsorbents were synthesized as novel R-BTP ones, and their fundamental adsorption/desorption properties for MA(III) and main FP and chemical/radiolytic stability were evaluated by batch experiments[11,12].

In the FY 2010, *cy*heptyl-BTP (R: 2-cyclopentylethyl) and tolyl-BTP (2,6-bis(1-p-tolyl-1H-tetrazol-5-yl)pyridine) adsorbents were additionally prepared, and the properties and stability were investigated and compared among 4 types of R-BTP adsorbents. Then, the simplified MA separation process was concretely proposed by evaluation of column experiments using the most promising R-BTP adsorbent under temperature control.

Experimental

As the novel R-BTP adsorbents, *iso*hexyl-, *iso*heptyl-, *cy*heptyl-BTP and tolyl-BTP adsorbents were prepared by impregnating the respective R-BTP ligands (or extractants) into the macroporous silica/polymer composite support (SiO_2-P particles)[5-10].

Adsorption and desorption properties were evaluated by batch method. The former was obtained by measuring distribution coefficient, K_d[11]. The concentration (or radioactivity) of ^{241}Am, which is one of typical MA nuclides, and simulated FP (Cs, Sr, Zr, Mo, Pd, *etc.*) including RE (Y, Ce, Nd, Eu, Dy, *etc.*) in solution was analyzed by γ-ray spectrometry, ICP-AES (inductively coupled plasma–atomic emission spectrometry), *etc.*

Radiolytic stability of the adsorbents were examined under relatively low dose rate (35~40 Gy/h) contacting with various concentrations of HNO_3 solution by irradiating γ-rays from ^{60}Co. Leakage of R-BTP extractants, degradation evalution and thermal stability of the adsorbents under γ-ray irradiation were examined by TOC (total organic carbon analysis), and TG-DTA (thermogravimetry-differential thermal analysis).

Separation behaviors of Am from the simulated FP was evaluated using by a glass column with a glass jacket to maintain constant temperature (25 and 50 °C), which was packed with a weighed amount of the adsorbent (4~5 g). Elution curves were drawn from weight of effluent versus the ratio of C (metal concentration in effluent) to C_0 (metal concentration in initial solution).

Results and Discussion

(1) Fundamental properties of the synthesized R-BTP adsorbents

Appearance, chemical structure and bonding of the synthesized R-BTP/SiO_2-P adsorbents were verified by analyzing the adsorbents as products, R-BTP ligands (extractants) and SiO_2-P particles as ingredients by SEM (scanning electron microscopy), FT-IR (Fourier transform infrared spectrophotometry), NMR (nuclear magnetic resonance spectroscopy) and/or HPLC (high performance liquid chromatography). The respective extractants had almost the same purity (97~99%). Thermal decomposition properties of the R-BTP adsorbents bore some resemblance to each other. Table 1 shows weight composition of the adsorbents obtained by TG-DTA. The weight percentage of all extractants was 33~34%, and such high content results in sufficient adsorption capacity for target ions.

(2) Adsorption and desorption properties of Am and main FP

Figure 2 shows comparison among the K_d values of 0.1 mM RE(III) onto *iso*hexyl-, *iso*heptyl- and *cy*heptyl-BTP adsorbents in 3 M HNO_3. Trace amounts of Dy(III) had dominantly higher K_d value onto *iso*hexyl-BTP/SiO_2-P adsorbent than the other RE[11]. While *iso*heptyl- and *cy*heptyl-BTP adsorbents also gave unique tendency that middle-to-heavier RE(III) had rather high K_d values, tolyl-BTP adsorbent had no adsorbabilty for RE except for pH region. Table 2 shows the K_d of Am and *SF*(Am/Eu) for the respective adsorbents. Adsorbability of Am and separation property between Am and RE seemed to be excellent especially for *iso*hexyl- and *iso*heptyl-BTP adsorbents and the highest K_d (Am) value was observed for *iso*hexyl-BTP adsorbent. In addition, the K_d values of Am were much higher than those of the simulated FP except Pd, which had dominantly high value onto the adsorbents.

On the other hand, adsorption kinetic rate with 3 M HNO_3 solution and desorption kinetic rate with H_2O at 25°C were extremely slow, especially for *iso*heptyl- and *cy*heptyl-BTP adsorbents. Figure 3 shows the effects of contact time on desorption with H_2O from several RE(III) ions loaded *iso*hexyl-BTP adsorbent at 50°C. Since the desorption kinetic rate of the ions at 50°C was more rapid than that at 25°C, effective elution of the ions from the column packed with the adsorbent will be expected at the elevated temperature.

(3) Radiolytic and chemical stability of R-BTP adsorbents

The radiolytic and chemical stability of R-BTP adsorbents were evaluated by comparing the adsorbability of RE and leached amounts of the R-BTP ligands between the irradiated and non-irradiated absorbents, contacting with 0.01~3 M HNO_3 solution, under 30~120 kGy dose up to about 120 d.

Unfortunately, except for a case of the irradiated *iso*hexyl-BTP adsorbent in 0.01 M HNO_3 solution, all the K_d values decreased with increasing γ-ray dose and concentration of HNO_3. For non-irradiated *iso*hexyl-BTP adsorbent, however, the K_d values of RE (Eu, Gd and Dy) were steadily maintained at an equilibrium state even in 3 M HNO_3 solution within 20 d11), the adsorbent must be resistant to the acidic solution.

Concerning leakage of the R-BTP ligands from irradiated absorbents, their leached amounts were increased by several to several ten times with irradiated dose/contact time and HNO_3 concentration compared with non-irradiated R-BTP adsorbents. The leakage was less than 0.1% (10~25 ppm) at 25°C and 0.3% (20~50 ppm) at 50°C.

(4) Evaluation of single-column separation between Am and FP

From the above results, the *iso*hexyl-BTP adsorbent was selected as the most promising one for single-column separation of MA(III) from FP13). In the column experiment at 25ºC, Am was separated from not only Cs, Sr, Zr, Mo, Ru, Rh, *etc*. but also light RE with 3 M HNO_3 solution. However, recovery yield of Am with H_2O was extremely low (14%) probably due to the slow desorption rate. Since the pH values immediately increased at eluting Am with H_2O, some hydrolysis of Am nitrate may be occurring at 25ºC14,15). On the other hand, in the column experiment at 50ºC, the recovery yield of Am with H_2O was much improved (≈70%) principally due to the rapid desorption kinetic rate.

These results enabled us to evaluate successful separation of Am from FP by charging feed solution and washing FP in 3 M HNO_3 at 25ºC and then by eluting Am with H_2O at 50ºC as shown in Fig. 413). From this figure, scheme for single-column separation of MA(III) under temperature control could be proposed as “a simplified separation process of trivalent MA” as shown in Fig. 5. The use of 3 M HNO_3 at 25ºC for feed and washing are expected to diminish radiolytic and chemical damage for the absorbent due to elimination of ^{137}Cs and ^{90}Sr at an early separation stage. The leakage of *iso*hexyl-BTP extractant at 50ºC was about twice as high as that at 25ºC and the total amount of the leaked extractant was less than 0.5%.

For more effective separation of Am from middle and heavy RE, enough washing with HNO_3 (larger quantity and/or lower concentration) is required and for more complete recovery of Am retained the column, complex agents such as DTPA may be necessary as an eluting solution14-16). Since Pd was strongly adsorbed in the column, it may be recovered with 0.1 M thiourea (CH_4N_2S) solution at 50°C12).

Conclusions

With the objective of direct recovering MA(III) from FP in HLLW, four types of silica-based R-BTP adsorbents for extraction chromatography were synthesized. Then, establishment of the simplified MA separation process by using the adsorbents was challenged and the intended objective was achieved in principle.

From viewpoints of the separation of MA(III) from main FP including RE(III) and stability of the adsorbents, the *iso*hexyl-BTP adsorbent was selected as the most promising R-BTP one. Consequently, the simplified separation process was successfully demonstrated by evaluation of column experiments using *iso*hexyl-BTP adsorbent under temperature control between 25 and 50°C.

In actual HLLW, small amounts of other actinides such as U, Pu and Np may exist and the optimum separation of MA including such actinides should be considered. As future work, the process needs to be demonstrated for the actual HLLW. In addition, development of more endurable adsorbents against severe radiolysis should be pursued.

Acknowledgments

A part of this study is the results of “Development of a Simplified MA Separation Process Using Novel R-BTP Adsorbents” carried out under the Strategic Promotion Program for Basic Nuclear Research by the Ministry of Education, Culture, Sports, Science and Technology of Japan (MEXT).

References

1) Van Hecke K., et al., SCK·CEN-BLD-1030 (2006).
2) Kolarik Z., et al., Solv. Extr. Ion Exch. **17** (1999) 23.
3) Ekberg K., et al., Radiochim. Acta **96** (2008) 225.

4) Wei Y.Z., et al., Proceedings of 16th Pacific Basin Nuclear Conference (16PBNC), Aomori, Japan, Oct. 13-18, 2008, Paper ID P16P 1033.
5) Zhang A., et al., J. Radioanal. Nucl. Chem. **274** (2007) 455.
6) Hoshi H., et al., J. Alloys Comp. **408-412** (2006) 1274.
7) Wei Y.Z., et al., *ibid*. **374** (2004) 447.
8) Wei Y.Z., et al., J. Nucl. Sci. Technol. **Suppl.3** (2002) 761.
9) Wei Y.Z., et al., *ibid*., **37** (2000) 1108.
10) Wei Y.Z., et al., Nucl. Technol. **132** (2000) 413.
11) Usuda S., et al., J. Ion Exchange **21** (2010) 35.
12) Liu R., et al., J. Radioanal. Nucl. Chem. **292** (2012) 537.
13) Usuda S., et al., J. Nucl. Sci. Technol. **49** (2012) 334.
14) Sano Y., et al., Actinides 2009 (IOP Publishing Ltd) (2010) 1.
15) Surugaya N., et al., ACS Symposium Series **1046** (2010) 131.
16) Matsumura T., et al., J. Nucl. Sci. Technol. **48** (2011) 855.

Table 1. Weight composition of the R- BTP adsorbents obtained by TG-DTA.

Adsorbents (R-BTP/SiO_2-P)	H_2O [%]	R-BTP extractants [%]	SDB polymer [%]	SiO_2 particles [%]
*iso*hexyl-BTP	1.0	33.2	15.0	50.8
*iso*heptyl-BTP	0.7	34.1	14.9	50.3
*cy*heptyl-BTP	1.1	34.2	14.8	49.9
tolyl-BTP*	0.7	35.0	15.7	48.7

Atmosphere gas: O_2, gas flow rate: 30 mL/min, temperature elevating rate: 1ºC/min (*2ºC/min).

Table 2. Distribution coefficients (K_d) of Am and separation factors (*SF*) between Am and Eu onto R-BTP adsorbents in 3 M HNO_3 at 25ºC.

Adsorbents (R-BTP/SiO_2-P)	K_d (Am) (mL/g)	*SF* (Am/Eu)
*iso*hexyl-BTP	8,500	≈2,200
*iso*heptyl-BTP	5,800	$>10^3$
*cy*heptyl-BTP	980	≈230
tolyl-BTP*	0	−

Resin: 0.5 g, HNO_3: 10 mL, contact time: 3 h.

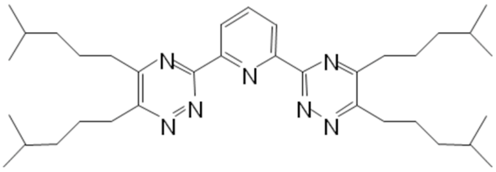

Figure 1. Schematic structure of *iso*hexyl-BTP ligands (2,6-bis(5,6-bis(4-methylpentyl)-1,2,4-triazin-3-yl)pyridine).

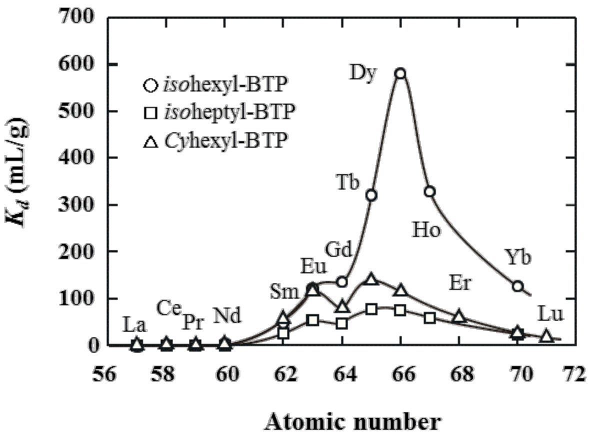

Figure 2. Distribution coefficients (K_d) of RE onto R-BTP adsorbents in 3 M HNO_3 solution (0.1 mM RE(III), phase ratio: 0.25 g/10 cm^3, contact time: 72 h, temperature: 20 ºC).

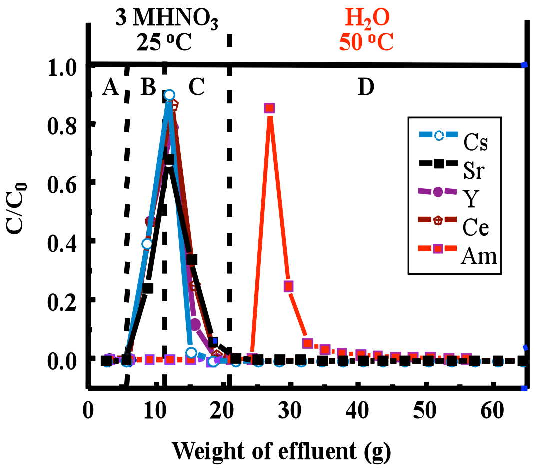

Figure 4. Estimated elution curves of Am and some FP using *iso*hexyl-BTP/SiO_2-P adsorbent under temperature control

(A: dead volume, B: feed soln., C: washing soln., D: eluting soln., flow rate: 0.25 mL/min).

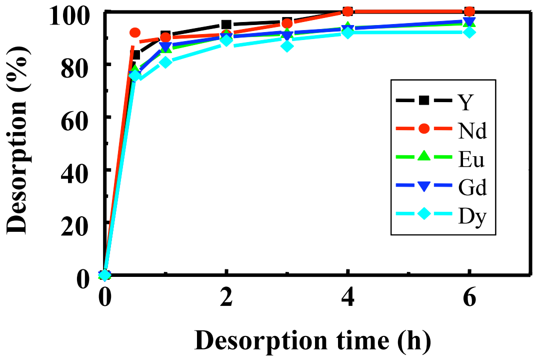

Figure 3. Effects of act time on desorption with H_2O fromcont RE loaded *iso*hexyl-BTP adsorbent at 50ºC

(adsorption conditions: 1 mM RE(III), 3 M HNO_3, 50ºC, 5 h).

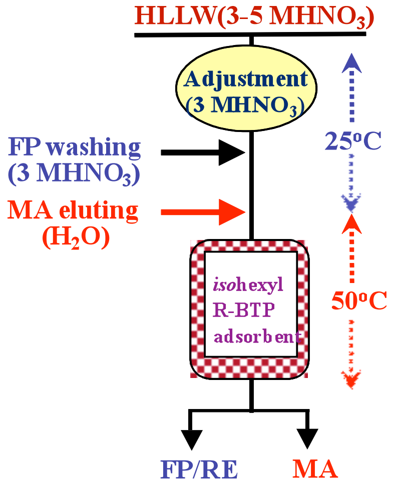

Figure 5. Single-column separation of MA(III) under temperature control (Simplified MA(III) separation process).

(**FP**: Cs, Sr, RE, Zr, Mo, etc., **RE**: Y, La, Ce, Pr, Nd, Sm, Eu etc., **MA**: Am, Cm)

VI. 2. Study on Selective Separation and Recovery of Cesium and Strontium from High-level Liquid Waste (HLLW)

Kim S.-Y.[1]*, Wu Y.*[1]*, Tozawa D.*[2]*, Ito T.*[2]*, Y Xu.*[1]*, Hitomi K.*[1]*, Tada T.*[1]*,*
Yamazaki H.[1]*, and Ishii K.*[2]

[1]*Cyclotoron and Radioisotope Center, Tohoku University*
[2]*Graduate School of Engineering, Tohoku University*

Introduction

The heat-generated nuclides, ^{137}Cs and ^{90}Sr, having half-lives of about 30 years exhibit high radioactivity and heat generation, and large amounts of Cs(I) and Sr(II) group are contained in high-level liquid waste (HLLW)1). Therefore, selective separation of ^{137}Cs and ^{90}Sr from HLLW is an important environmental issue for nuclear waste management. In addition, the purified Cs(I) and Sr(II) are expected for the reuse as radiation and heat sources in the field of medicine and industry. The liquid-liquid solvent extraction method for partitioning Cs(I) and Sr(II) has been actively studied. In the liquid-liquid solvent extraction process such as CSSX, SREX and FPEX2~4), the supramolecular recognition agents are well known to have selective extractability to Cs(I) and Sr(II)5~9). 1,3-[(2,4-Diethylheptylethoxy) oxy]-2,4-crown-6-calix[4]arene (calix[4]arene-R14), a kind of supramolecular recognition composite, shows a high selectivity toward Cs(I) and excellent radiation stability. The calix[4]arene-R14 compound is composed of chemical bonding of a calix[4]arene and an 18-crown-6 by phenolic oxgen and polyether chain. It has the ability to extract Cs(I) due to the effective complexion of Cs(I) with the hydrophilic crown ether and high selectively of calix[4]arene for Cs(I), such as a good match between the cavity of calix[4]arene and ionic radius of Cs(I) ion, π-bonding interaction with the arene groups, etc10). 4,4',(5')-Di(tert-butylcyclohex-ano)-18-crown-6 (DtBuCH18C6), a microcyclic crown ether, has an excellent extraction ability and selectivity for Sr(II). It has the ability to extract Sr(II) due to the effective 1:1 complexion of Sr(II) with the hydrophilic crown ether11), and a good match between the cavity of crown ether and ionic radius of Sr(II) ion. In order to utilize these extraxtants having high affinity for Cs(I) and

Sr(II), the extraction chromatography has been proposed, which has many advantages such as a small amount of organic waste and compact equipment. Recently, an impregnation method for extraction chromatography has been proposed to immobilize the organic solvents into the porous silica/polymer composite support (SiO_2-P particles)[12,13].

The SiO_2-P support is a kind of inorganic material, which prepared by impregnation the copolymer inside the macroporous SiO_2 substrate. Impregnation the extractans onto SiO_2-P has a number of advantages such as mechanical strength, strong acid and radiation resistance, and ease of solid-liquid separation by simple equipments. Thus, the impregnation of the extractans onto SiO_2-P support seems to be one of the most prominent techniques for the practical extraction chromatography operation.

In this study, we have attempted to loaded the calix[4]arene-R14, DtBuCH18C6 and their modifier, 1-dodecanol, into SiO_2-P ((calix[4]+Dodec)/SiO_2-P, (DtBuCh18C6+Dodec)/SiO_2-P) for the selective separation of Cs(I) and Sr(II) from HLLW. The present paper deals with the preparation of 2 kinds of supramolecular recognition absorbents, characterization and evaluation of their adsorption abilities.

Experimental

Materials

Calix[4]arene-R14 and DtBuCH18C6 were purchased from Sigma-Aldrich Chemical Co. Other chemicals such as $CsNO_3$, $Sr(NO_3)_2$, $Ba(NO_3)_2$, $RE(NO_3)_3\cdot 6H_2O$ (RE = La, Ce, Nd, Sm, and Gd) were reagent grade supplied by Kanto Chemical Co. Ruthenium nitrosyl nitrate solution (1.5wt%), rhodium nitrate solution (10wt%) and palladium nitrate solution (10wt%) were purchased from Sigma-Aldrich Chemical Co.

Determination of Distribution Coefficient

The distribution of metal ions were estimated by batch method. An aqueous solution (4 cm^3) containing 5 mM metal ions was contacted with 0.2 g of (calix[4]+Dodec)/SiO_2-P or (DtBuCH18C6+Dodec)/SiO_2-P at 25±1°C up to 5 h, which was found to be sufficient for attaining equilibrium. The distribution coefficient(K_d) are defined as,

$$K_d = (C_o - C_f)/C_f \times (V/m), (cm^3 g^{-1}) \qquad (1)$$

where C_o and C_f denote metal ions concentration (mM) in the aqueous phase before and after adsorption, respectively; V (cm^3) indicates the volume of the aqueous phase and m (g) is the weight of the dry absorbent.

Column Operation

The column was prepared by packing the (calix[4]+Dodec)/SiO_2-P or (DtBuCH18C6+Dodec)/SiO_2-P in a glass column with thermostatic water jacket. The simulated high-level liquid waste (SHLLW) was passed through the column. Here, the concentration of HNO_3 in SHLLW was adjusted to 3 M. Elution of the column was carried out by flowing 3 M HNO_3 and H_2O solution as eluent.

Results and Discussion

Effect of HNO_3 concentration on K_d

Figure 1 shows adsorption ability of (calix[4] + Dodec)/SiO_2-P for various metal ions, Cs(I), Sr(II), Ru(III), Rh(III), Pd(II), La(III), Ce(III), Nd(III), Sm(III), Gd(III), Zr(IV) and Mo(VI) at different concentrations of HNO_3 up to 8 M. As for Cs(I), the K_d value tended to increase with increasing HNO_3 concentration of 0.1 ~ 4 M HNO_3 and relatively large K_d value above 90 cm^3/g was obtained around 4 M HNO_3. This effect is due to the extraction of an ion-pair species according to the following related reaction (Eq. 2), indicating that the availability of higher amount of nitrate ion for the ion-pair formation. On the other hand, the K_d of Cs(I) tended to gradually decrease above 4 M HNO_3. This indicated that at higher HNO_3 concentration, the adsorption was governed by solvent extraction of nitric acid with crown ether function group of Calix[4]arene-R14 (Eq. 3). In contrast, the K_d values for Sr(II), Ru(III), Rh(III), Pd(II), La(III), Ce(III), Nd(III), Sm(III), Gd(III), Zr(IV) and Mo(VI)) were considerably low in the range of 0.1 ~ 8 M HNO_3. The reason might be due to the unmatched size between these metals and calixarene cavity of calix[4]arene-R14.

$$Cs^{+}_{(aq)} + NO_3^{-}{}_{(aq)} + Calix[4]_{(org.)} \rightleftarrows [Cs\cdot Calix[4]\cdot NO_3]_{(org.)} \quad (2)$$

$$HNO_{3(aq)} + Calix[4]_{(org.)} \rightleftarrows [Calix[4]\cdot HNO_3]_{(org.)} \quad (3)$$

The K_d value of metal ions for (DtBuCH18C6 + Dodec)/SiO_2-P was obtained at different HNO_3 concentrations of 0.1 ~ 4 M. As can be seen, the K_d value of Sr(II) increased with the HNO_3 concentration, and deceased above 3 M HNO_3. These indicate that the adsorption of Sr(II) on (DtBuCH18C6 + Dodec)/SiO_2-P was governed by solvent extraction of DtBuCH18C6 with Sr(II) (Eq. 4) and HNO_3 (Eq. 5). The K_d values of other metal ions were lower than 10 cm^3/g, these also was realized by the unmatched size between these metals and cavity of DtBuCH18C6.

$$Sr^{2+}_{(aq)} + NO_{3\,(aq)}^{-} + DtBuCH18C6_{(org.)} \rightleftarrows [Sr(NO_3)_2 \cdot DtBuCH18C6]_{(org.)} \quad (4)$$

$$HNO_{3(aq)} + DtBuCH18C6_{(org.)} \rightleftarrows [DtBuCH18C6_{(org.)} \cdot HNO_{3(aq)}] \quad (5)$$

Chromatographic Separation

Figure 2 shows the chromatograms of Cs(I) separation from SHLLW using (calix[4]+Dodec) /SiO_2-P packed column. Figure 2 illustrates the chromatogram of Cs(I), alkaline earth metals (Sr(II), Ba(II)), platinum group metals(Ru(III), Rh(III), Pd(II)), rare earth metals (La(III), Ce(III), Nd(III), Sm(III), Gd(III)), Zr(IV) and Mo(VI). It was shown that a well-resolved chromatogram was obtained. Most of metal ions except Cs(I) were readily breakthrough the column and effectively eluted with 3 M HNO_3. These metal ions adsorption behaviors were similar to that of batch experimental, indicating that the adsorption of Cs(I) was not affected by existence of Sr(II), Ba(II), Ru(III), Rh(III), Pd(II), La(III), Ce(III), Nd(III), Sm(III), Gd(III), Zr(IV) and Mo(VI) in the SHLLW. After washing with distilled water, the Cs(I) adsorbed on (Calix[4]+Dodec)/SiO_2-P was gently eluted from the column with the increasing pH value. The chromatogram of Cs(I) showed slight tailing and a large retention volume. Here, the elution of Cs(I) was due to the dissociation of ion-pair in such low concentrated NO_3^- solution, resulted in reversing the extraction of Cs(I) (Eq. 2). In addition, the regeneration of (calix[4]+Dodec)/SiO_2-P can be carried out by washing with distilled water. The elution behaviors of rare earth metals were similar to the divalent metals and platinum group metals.

Figure 3 showes the chromatograms of Sr(II) separation from SHLLW using (DtBuCH18C6 + Dodec) /SiO_2-P packed column. Figure 3 illustrated the chromatogram of Sr(II), Ba(II), Ru(III), Rh(III) , Pd(II), Ce(III), Nd(III), Sm(III), Gd(III), Zr(IV) and Mo(VI). Most of metal ions excepted Ba(II) can be separated from Sr(II) by flowing 3 M HNO_3. On the other hand, Sr(II) and Ba(II) were selectively absorbed onto the (DtBuCH18C6 + Dodec) /SiO_2-P, and then efficiently eluted by washing with H_2O.

These findings indicated that the selectively separation of Cs(I) and Sr(II) from HLLW can be performed as following steps: at first, the HLLW is passed through the (calix[4]+ Dodec) /SiO_2-P packed column; then the residual fraction is flushed down the (DtBuCH18C6 + Dodec) /SiO_2-P packed column. (Fig. 4)

Conclutions

The adsorption of Cs(I) onto (calix[4]+Dodec)/SiO_2-P was fairly fast in the initial stage and reached equilibrium within 1 h. The K_d value for Cs(I) was increased with increasing HNO_3 concentration and had a maximum at around 4 M HNO_3. The K_d values for Sr(II), Ba(II), Ru(III), Rh(III), Pd(II), La(III), Ce(III), Nd(III), Sm(III), Gd(III), Zr(IV) and Mo(VI)) were considerably low at 0.1 ~ 8 M HNO_3. The separation of Cs(I) from SHLLW was accomplished using the columns packed with (Calix[4]+Dodec)/SiO_2-P. The Cs(I) ions adsorbed on the top of the column were chromatographically eluted with distilled water. (DtBuCH18C6+Dodec) /SiO_2-P exhibited relatively large K_d values around 1.5×10^2 cm^3/g at the range of 2 ~ 3 M HNO_3. The other metal ions, Ba(II), Ru(III), Rh(III), Pd(II), La(III), Ce(III), Nd(III), Sm(III), Gd(III), Zr(IV) and Mo(VI) showed almost no adsorption on (DtBuCH18C6+Dedec)/SiO_2-P. The Sr(II) was successfully separated from SHLLW by using the (DtBuCH18C6+Dodec) /SiO_2-P pack column.

The results suggested that the (calix[4]+Dodec)/SiO_2-P and (DtBuCH18C6+Dodec) /SiO_2-P were effective for selective separation and recovery of Cs(I) and Sr(II) from HLLW, and the proposed process was feasible for practical application.

References

1) Ando Y., Takano H., JAERI-Research 99-004 (1999).
2) Leonard R.A., Aase S.B., Arafat H.A., et al., Solv. Extr. Ion Exch. **21** (2003) 505.
3) Horwitz E.P., Dietz M.L., Fisher D.E., Solv. Extr. Ion Exch. **9** (1991) 1.
4) Riddle C.L., Baker J.D., Law J.D., et al., Solv. Extr. Ion Exch. **23** (2005) 449.
5) Dozol J.F., Simon N., lamare V., et al., Sep. Sci. Technol. **34** (1999) 877.
6) Sachleben R.A., Bonnesen P.V., Descazeaud T., et al., Solvent Extr. Ion Exch. **17** (1999) 1445.
7) Horwitz E.P., Dietz M.L., Fisher D.E., Solv. Extr. Ion Exch. **8** (1990) 199.
8) Kumar A., Mohapatra P.K., Pathak P.N., Manchanda V.K., Talanta **45** (1997) 387.
9) Raut D. R., Mohapatra P. K., Manchanda V. K., Radiochim.Acta **97** (2009) 565.
10) Asfari Z., Wenger S., Vicens J., J. Inclusion Phenom. Mol. Recognit. Chem. **19** (1994) 137.
11) Dietz M.L., Horwitz E.P., Chiarizia R., et al., Proc. of Int. Solv. Exta. Conf. **3** (1993) 1587.
12) Wei Y.Z., Kumagai M., Takashima Y., et al., Nucl. Technol. **132** (2000) 413.
13) Zhang A.Y., Xiao C.L., Liu Y.H., et al., J. Porous. Mater. **17** (2010) 153.

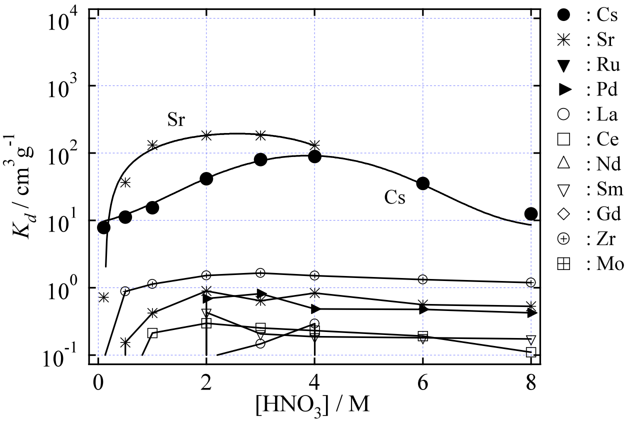

Figure 1. Effects of HNO_3 concentration on K_d of different metal ions by (Calix[4]+Dodec)/SiO_2-P and (DtBuCH18C6+Dodec)/SiO_2-P.

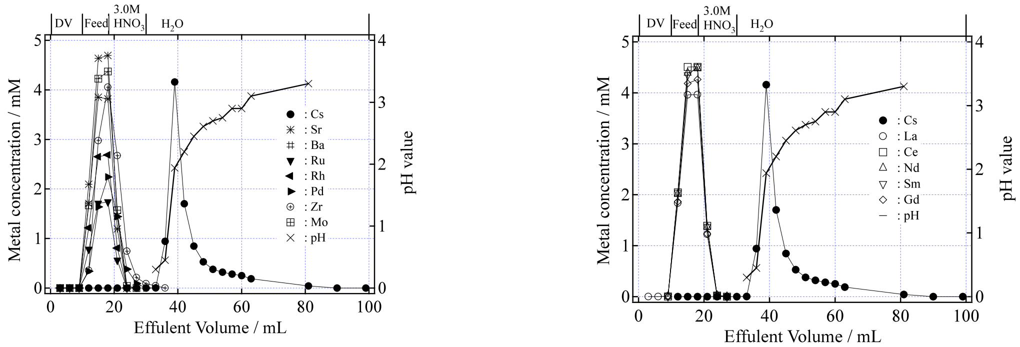

Figure 2. Chromatographic separation of SHLLW through (Calix[4]+Dodec)/SiO_2-P column.

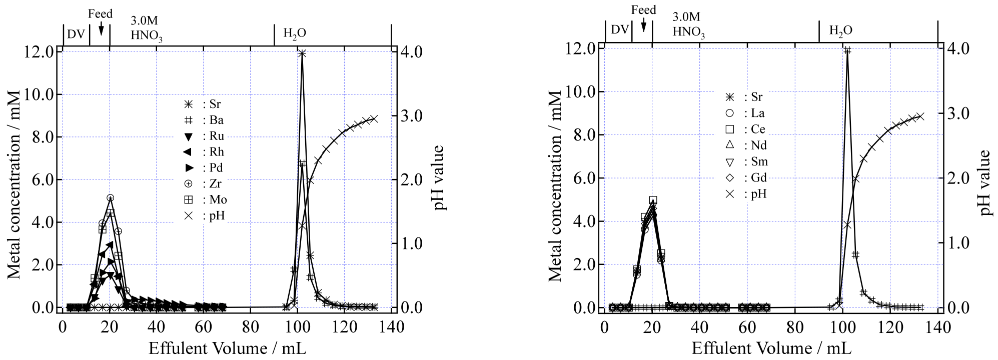

Figure 3. Chromatog (DtBuCH18C6+Dodec) /SiO_2-P column.

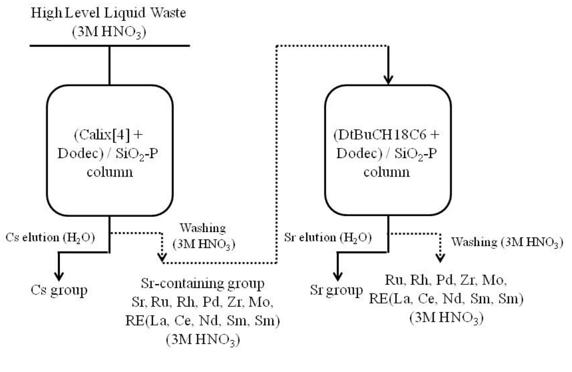

Figure 4. Concept of Cs and Sr separation process.

VI. 3. Study on Adsorption Behavior of Trivalent Rare Earths onto a Macroporous Silica-Based TODGA Adsorbent from High Level Liquid Waste

Xu Y.[1]*, Kuraoka E.*[1]*, Usuda S.*[1]*, Kim S. Y.*[1]*, Hitomi K.*[1]*, Tada T.*[1]*,*
Yamazaki H.[1]*, and Ishii K.*[2]

[1]*Cyclotoron and Radioisotope Center, Tohoku University*
[2]*Graduate School of Engineering, Tohoku University*

Introduction

Nuclear power is believed to play an important role for long-term energy security and global warming prevention in the 21st century. On the other hand, to ensure a sustainable development of nuclear energy in the future, it is necessary to establish a closed nuclear fuel cycle to save uranium resource and minimize radioactive waste accumulation. However the elements which contribute most to the long term radiotoxicity in high level liquid waste (HLLW) are the minor actinides (MA=Am, Cm, etc.) after a few hundred years. The purpose of this study is to separate MA from HLLW, especially the separation of trivalent MA from the rare earths (REs) is a key step that remains to be solved owing to the chemical similarity1-3). The study of adsorption behavior of trivalent RE onto TODGA adsorbent is one of important studies in the designed two-column separation process.

This study is carried out based on the two-column separation method as illustrated in Fig. 1, which contains two main separation steps. Two columns packed with silica-based TODGA (N,N,N',N'-tetraoctyl-3-oxapentane-1,5-diamide) adsorbent and R-BTP (BTP: 2,6-bis-(5,6-dialkyl-1,2,4-triazine-3-yl)-pyridine, R: alkyl group) adsorbent are utilized, respectively, for chromatographic separation of the elements through selective adsorption and elution procedures. The structural formula of TODGA is shown in Fig. 24,5). Compared to solvent extraction, extraction chromatography has many attractive advantages, such as no or very limited organic diluent utilization, compact equipment and less waste accumulation6).

As a part work of this process, currently work focused on the first column and a silica-based TODGA adsorbent (TODGA/SiO_2-P) was prepared by impregnating TODGA into the porous silica/polymer composite particles (SiO_2-P). Adsorption behavior of RE from simulated HLLW solution was investigated.

Experimental

The reagents $Y(NO_3)_3 \cdot 6H_2O$, $Nd(NO_3)_3 \cdot 6H_2O$, $Eu(NO_3)_3 \cdot 6H_2O$ and HNO_3 solution used are analytical grade. The chelating agent TODGA is an available commercial product with purity higher than 99%.

Adsorption behavior of RE ions onto adsorbent were examined by batch method, a weighed quantity of dry TODGA/SiO_2-P adsorbent was mixed into a 10 cm^3 glass flask with 5 cm^3 metal ions solution and shaken at 160 rpm for different contact time using a thermostatic bath shaker. After the phase separation through vacuum filtration, concentrations of metal ions in the liquid phase were determined by ICP-AES (Shimadzu ICPS-7510). The evaluated parameters distribution coefficient (K_d, cm^3/g) and adsorbed amount (Q, mmol/g) were calculated as follows:

$$K_d = \frac{(C_0 - C_e)}{C_e} \times \frac{V}{m} \qquad (1)$$

$$Q = \frac{V}{m} \times \frac{(C_0 - C_f)}{M} \qquad (2)$$

where, the C_0 and C_f denote the concentrations of metal ions before and after adsorption in the liquid phase in *ppm*, C_e denotes the concentrations of metal ion after reaching an equilibrium state in the liquid phase in *ppm*, *m* and *V* denote the weight of dry TODGA/SiO_2-P adsorbent in *g* and the volume of the liquid phase in cm^3, respectively, and *M* denotes the molecular weight of metal ion elements.

Results and discussion

To investigate the adsorption behavior of some typical RE, adsorption experiments using TODGA/SiO_2-P adsorbent were carried out for three kinds of trivalent RE, Y(III), Nd(III) and Eu(III) in 3 M HNO_3 solution under different contact times and temperatures. Effect of contact time on the adsorbed amount of the RE(III) are illustrated in Fig. 3 at 298 K. As can be seen in Fig. 3 the adsorption of Y(III) on TODGA/SiO_2-P adsorbent was evidently higher than that of other two RE(III) ions and the adsorption ability of these three RE(III) ions onto the adsorbent was: Y(III) > Eu(III) > Nd(III). At the beginning of adsorption, the Q of Y(III) for the adsorbent markedly increased with contact time and then reached an equilibrium state around 3 h. On the other hand, the Q values of Nd(III) and Eu(III) were smaller than Y(III) but achieved equilibrium state in a short time (within 30 min). Such great difference in adsorption amount for the same RE elements is rarely found and the mechanism needs to be investigated further.

In temperature experiments, the Y(III) exhibited a strong adsorption onto the adsorbent in the batch experiments at 288 K, 298 K, 308 K and 323 K. In the whole adsorption process, a notable phenomenon is that with the increase of temperature, the adsorption rate of Y(III) which can be evaluated by the time reaching equilibrium state increased, but the Q values in equilibrium state decreased regularly. In order to explain this influence of temperature on adsorption equilibrium of Y(III) towards TODGA/SiO_2-P adsorbent, the standard enthalpy change of Y(III) in the adsorption reaction can be correlated with the distribution coefficient by the van't Hoff equation as:

$$\ln K_d = -\frac{\Delta H^0}{R} \times \frac{1}{T} + C \qquad (3)$$

where $\triangle H^0$ is the standard enthalpy change in $J{\cdot}mol^{-1}$, T is the absolute temperature at which the reaction proceeds in Kelvin, R is the gas constant (i.e. 8.314 $J{\cdot}mol^{-1}{\cdot}K^{-1}$), C is a constant, and K_d is the distribution coefficient on equilibrium state defined as Eq. (1).

The fitted line is shown in Fig. 4, the value of the standard enthalpy change of Y(III) in this adsorption reaction was determined to be -2.49 $kJ{\cdot}mol^{-1}$ from the slope in the line of $\ln K_d$ versus T^{-1}, which indicates that the adsorption process is an exothermic reaction, therefore lower temperature resulted in a stronger adsorption.

As two important thermodynamic parameters, the Gibbs free energy change (G^0) and the standard entropy (S^0), were calculated by the following equation:

$$\ln K_d = \Delta S^0/\mathrm{R} - \Delta H^0 / \mathrm{RT} \qquad (4)$$

$$\Delta G^0 = \Delta H^0 - \mathrm{T}\Delta S^0 \qquad (5)$$

The above obtained thermodynamic parameters (ΔG^0, ΔH^0, ΔS^0) for the adsorption of Y(III) onto TODGA/SiO_2-P adsorbent are presented in Table 1. The ΔG^0 is a fundamental criterion of spontaneity, this adsorption reactions occur spontaneously at a given temperature if ΔG^0 is a negative quantity[7,8].

Figure 5 shows the explanation of Y(III) adsorption onto TODGA adsorbent by the following Langmuir isotherm adsorption equation:

$$\frac{1}{Q}=\frac{1}{k_nQ_{\max}}\times\frac{1}{[Y^{3+}]}+\frac{1}{Q_{\max}} \tag{6}$$

where Q denotes the adsorbed amount, Q_{max} denotes the maximum adsorption capacity, and K_n denotes the adsorption equilibrium constant of Y(III) onto TODGA adsorbent.

A plot of 1/Q versus 1/[Y^{3+}] is shown in Fig. 5 and the experimental results can be expressed as:

$$\frac{1}{Q}=\frac{0.03}{[\mathrm{Y}^{3+}]}+5.9 \tag{7}$$

with a correlation coefficient of 0.99. From the slope of the resulting straight line and its intercept, the maximum adsorption capacity (Q_{max}) of TODGA/SiO_2-P for Y(III) and the equilibrium constant of the adsorption reaction (k_n) were determined to be 0.16 mmol/g (14 mg/g) and 208 M^{-1}, respectively. This results obtained showed that this adsorption process could be expressed by Langmuir monomolecular layer adsorption mode.

Conclusions

In batch experiments, the adsorption of Y(III) on TODGA/SiO_2-P adsorbent was evidently higher than that of other two RE(III) ions and the adsorption ability of these three RE(III) ions onto the adsorbent was: Y(III) > Eu(III) > Nd(III). The thermodynamic parameters (ΔG^0, ΔH^0, ΔS^0) for the adsorption of Y(III) onto TODGA adsorbent were calculated and the adsorption process of Y(III) with TODGA adsorbent could be expressed by Langmuir mono-molecular layer adsorption mode.

References

1) Magill J., Berthou V., Haas D., et al., Nucl. Ener. **42** (2003) 263.
2) Nash K.L., Barrans R.E., Chiarizia R., et al., Solv. Extr. Ion Exch. **18** (2000) 605.
3) Zhang A., Kuraoka E., Kumagai M., European Polymer J., **43** (2007) 529.
4) Wei Y., Hoshi H., Kumagai M., Asakura T., Morita Y., J. Alloys Comp. **374** (2004) 447.
5) Zhu Z., Sasaki Y., Suzuki H., et al., Anal. Chem. Acta **527** (2004) 163.
6) Wei Y., Kumagai M., Takashima Y., Nucl. Technol., **132** (2000) 413.
7) El-Kamash A.M., J. Hazard. Mater. **151** (2008) 432.
8) Nilchi A., Saberi R., Moradi M., et al., J. Radioanal Nucl. Chem., DOI 10.1007/s 10967-011-1455-6.

Table 1. Values of the thermodynamic parameters for the adsorption of Y (III) ions onto TODAG adsorbent.

Temperature (K)	K_c	ΔG^0 (kJ/mol)	ΔH^0 (kJ/mol)	ΔS^0 (J/mol·K)
288	3.33	-2.88	-2.49	1.36
298	3.30	-2.96		
308	3.17	-2.95		
323	3.01	-2.96		

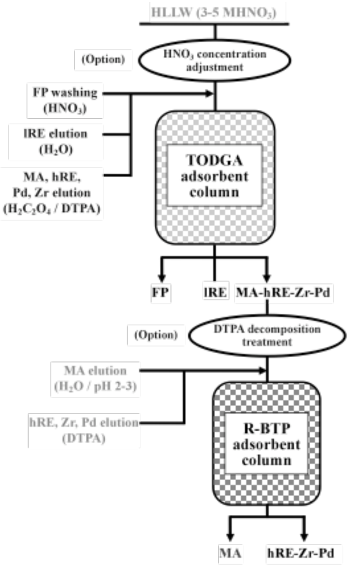

Figure 1.　Flowsheet of two-column separation method by extraction chromatography.

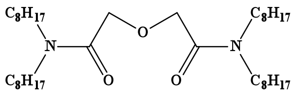

Figure 2.　Molecular structure of TODGA (N,N,N’,N’-tetraoctyl-3-oxapentane-1,5-diamide).

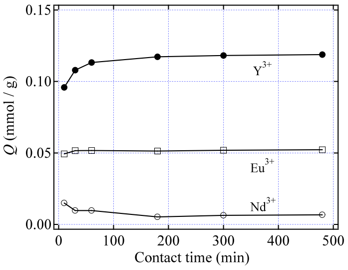

Figure 3.　Effect of contact time on Q of RE(III) at 298 K

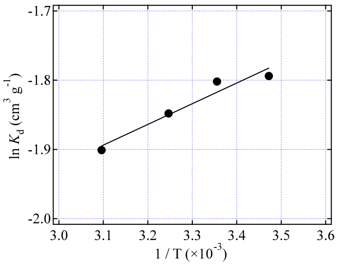

Figure 4.　Relationship between K_d of Y(III) and T^{-1}.

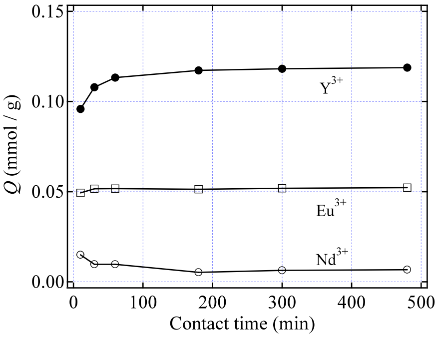

Figure 5.　Langmuri isotherm adsorption equation of Y(III) onto TODGA

VII. 1. Microfluidic Radiofluorination Using Electrochemically Concentrated [^{18}F]Fluoride

Wong R.[1], Iwata R.[1], Furumoto S.[1,2], Saiki H.[3], Ishikawa Y.[1], and Ozeki E.[3]

[1]*Cyclotoron and Radioisotope Center, Tohoku University*
[2]*Graduate School of Medicine, Tohoku University*
[3]*Technology Research Laboratory, Shimadzu Corporation*

Microfluidics is the science of the containment and flow of liquids on a microscale level. This generally means the handling of liquids on a nanoliter to microliter range using suitable platforms that are typically micro structured. Touted benefits from conducting experiments on such interfaces are numerous, including better heat exchange, better reaction kinetics, less wastage of reagents, shorter reaction times and most importantly similar if not better reaction yields. Previous attempts at microfluidic radiosyntheses of PET tracers had been stifled by the issue of ^{18}F supply that, ideally, should be sufficiently concentrated at a suitable volume for immediate use during the radio-labeling procedure. Conventional ^{18}F-labeled probe production is generally tedious, time-consuming and remains a significant limiting factor towards effective application of microfluidics in this field.

The recent introduction of rapid transfer of [^{18}F]fluoride from water to an anhydrous solvent by means of electrochemical concentration1) addresses this problem and is a significant step towards practical applications of microfluidics in the field of PET radiochemistry. In order to demonstrate the usefulness of this electrochemically concentrated [^{18}F]fluoride, nucleophilic ^{18}F-substitution reactions through radiosynthesis of [^{18}F]FDG, [^{18}F]FMISO, [^{18}F]flumazenil, and [^{18}F]fluoromethyl bromide were carried out in a microfluidic reaction flow cell and effects of reaction time, temperature, precursor concentration and reaction solvent on the ^{18}F-substitution yields were investigated.

The microfluidic reaction flow cell is made entirely out of quartz glass to minimize solvent compatibility issues. It has two inlets for the addition of the precursor solution and the reactive [^{18}F]fluoride solution and one outlet for product collection. The cell has a flow channel 200 μm wide and 150 μm deep, and two volume capacities of 30 μL and 100 μL depending on the length of its channel.

Reactive [^{18}F]fluoride was prepared according to the previously reported literature1). The entire microfluidic module consists of two customized platforms each for the placement of the [^{18}F]fluoride concentration chip and the microfluidic reaction flow cell. This is accompanied by various syringe valves and pumps for the containment and flow of the various reagents during the labeling process (Fig. 1). The entire module is controlled through dedicated software on a computer.

^{18}F-Fluorination yields for the four ^{18}F-labeled compounds under optimized conditions were 98% for protected [^{18}F]FDG, 80% for protected [^{18}F]FMISO, 20% for [^{18}F]flumazenil and 60% for [^{18}F]fluoromethyl bromide. These were all comparable to or higher than those obtained by conventional means. Yields were found to be predominantly affected by precursor concentration, type of reaction solvent as well as temperature (Fig. 2). In this study it is clearly demonstrated that microfluidic radiosynthesis is a powerful tool for effectively reducing synthesis times and especially for increasing radiochemical yields of products labile at high temperatures.

Reference

1) Saiki H., et al., Appl. Radiat. Isot. **68** (2010) 1073.

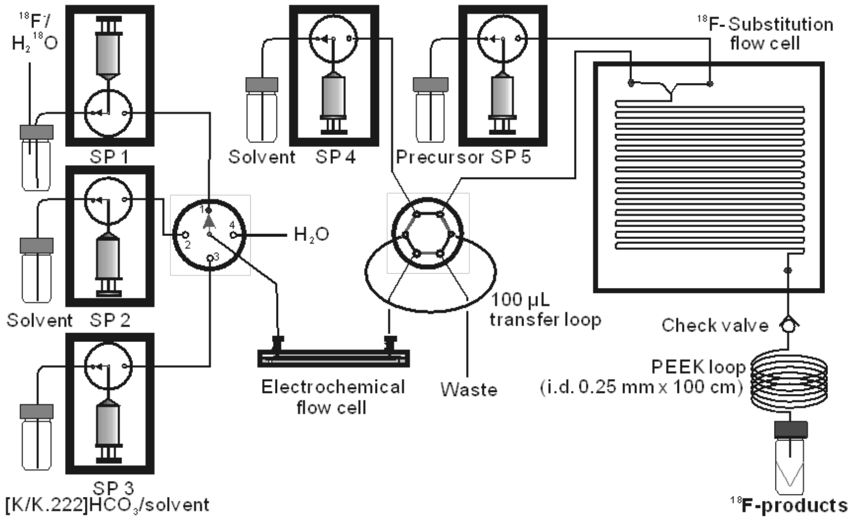

Figure 1. Microfluidic module.

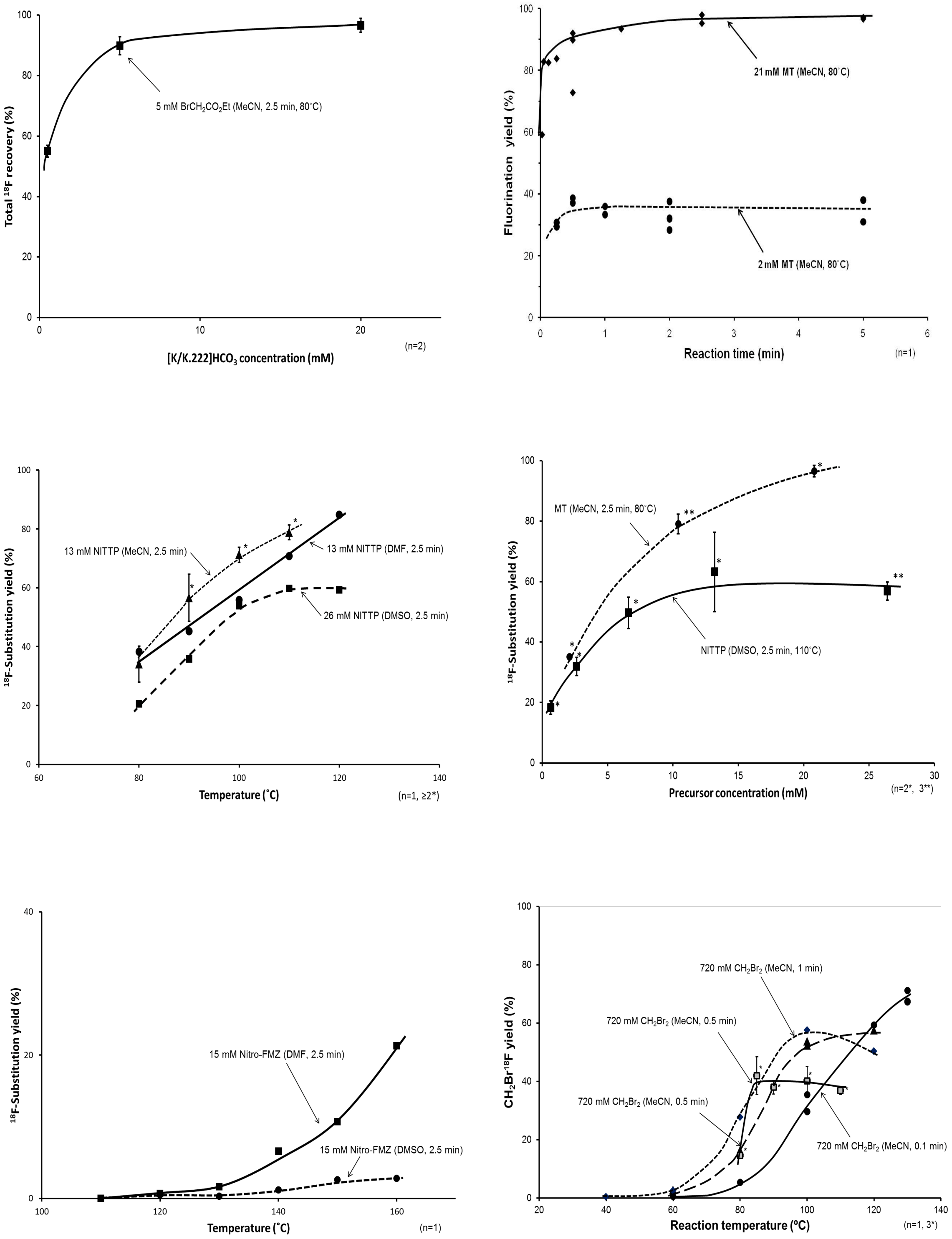

Figure 2. Effects of precursor concentration, reaction solvent and temperature on ^{18}F-substitution yields.

VIII. 1 PET Imaging in Cardiac Amyloidosis with [^{11}C]BF-227

Furukawa K.[1], Ikeda S.[2], Okamura M.[3], Tashiro M.[4], Tomita N.[1], Furumoto S.[3], Iwata R.[5], Yanai K.[3], Kudo Y.[6], and Arai H.[1]

[1]Department of Geriatrics and Gerontology, Division of Brain Sciences, Institute of Development, Aging and Cancer, Tohoku University
[2]Department of Medicine (Neurology & Rheumatology), Shinshu University School of Medicine
[3]Department of Pharmacology, Tohoku University Graduate School of Medicine
[4]Division of Cyclotron Nuclear Medicine, Cyclotron And Radioisotope Center, Tohoku University
[5]Division of Radiopharmaceutical Chemistry, Cyclotron And Radioisotope Center, Tohoku University
[6]Department of NeuroImaging Research, Innovation New Biomedical Engineering Center, Tohoku University

We report the case of a thirty two year old man who had suffered from orthostatic syncope and body weight loss since he was 27 years old. As years passed by, he also showed muscle weakness and abnormal sensations in both legs, hyporeflexia in four limbs, and autonomic failure (impotence, urinary & fecal incontinence, and edema in lower limbs) suggesting the presence of peripheral somatic and autonomic polyneuropathy. His mother, mother's father, and mother's paternal aunt also had similar symptoms to him. Both the sensory nerve action potential and the sensory nerve conduction velocity (NCV) of his rt. sural nerve were low (1.26 mV and 47.2 m/s, respectively) and the motor NCV of his rt. tibial nerve was 41.1 m/s (normal >45 m/s). A DNA test on him disclosed a missense mutation in the transthyretin (TTR) gene (Ser50Arg), which is relatively rare in familial TTR-related systemic amyloidosis1,2). TTR-immunoreactive amyloid deposition was demonstrated in the biopsied gastroduodenal mucosa (Fig. 1). Echocardiography showed a markedly thickened ventricular wall (thickness of interventricular septum: 22.3 mm (normal < 12 mm)) with normal wall motion (fractional shortening: 37.6% (normal: 28~42%)) indicating that he also had cardiac amyloidosis (Fig. 2A). Contrast magnetic resonance imaging3) revealed focal late gadolinium enhancement in the thickened ventricular wall (Fig. 2B). He was treated with orthotopic live-donor liver transplantation when he was 31 years old to alleviate and prevent exacerbation of his neuronal and cardiac symptoms. His condition including the neurological disability gradually improved and he started to work again at 10 months after liver transplantation.

In order to visualize amyloid deposition in the myocardium he underwent a cardiac PET study with [^{11}C]BF-227 that sensitively and specifically binds to aggregated amyloid fibrils[4)]. The PET images revealed significantly robust retention of [^{11}C]BF-227 in the heart of the patient compared to the normal control (Fig. 3). His biopsy specimens from the duodenum also showed higher signals of [^{11}C]BF-227 compared to the normal control (Fig. 1C, D). The present result provides evidence that our amyloid-specific PET tracer, [^{11}C]BF-227, can successfully detect amyloid deposition in the heart. Several molecules have been investigated to visualize cardiac amyloidosis, such as ^{99m}Tc-aprotinin and ^{99m}Tc-labeledled phosphate derivatives[2)]. None of the previous tracers, however, could specifically bind to aggregated amyloid which forms a b-pleated sheet structure. In any of the amyloidgenic disorders such as TTR-related systemic amyloidosis and Alzheimer's disease, it is surmised that the monomer of the amyloid protein itself is not very toxic, while misfolded oligomers could cause damage to human organs[1-4)]. It is, therefore, truly important to detect the accumulation of real amyloid fibrils for early and accurate diagnosis of amyloidosis. To our knowledge, this is the first report showing the usefulness of a b-pleated sheet structure-specific PET in investing visceral organ amyloidosis. This study was reported in "Circulation" in 2012[5)].

References

1) Ikeda S., Nakazato M., Ando Y., Sobue G., Neurology **58** (2002) 1001.
2) Rapezzi C., Quarta C.C., Riva L., Longhi S., Gallelli I., Lorenzini M., Ciliberti P., Biagini E., Salvi F., Branzi A., Nat. Rev. Cardiol. **7** (2010) 398.
3) Vogelsberg H., Mahrholdt H., Deluigi C.C., Yilmaz A., Kispert Eva M., Greulich S., Klingel K., Kandolf R., Sechtem U., J. Am. Coll. Cardiol. **s51** (2008) 1022.
4) Furukawa K., Okamura N., Tashiro M., Waragai M., Furumoto S., Iwata R., Yanai K., Kudo Y., Arai H., J. Neurol. **257** (2010) 721.
5) Furukawa K., Ikeda S., Okamura N., Tashiro M., Tomita N., Furumoto S., Iwata R., Yanai K., Kudo Y., Arai H., Circulation **125** (2012) 556.

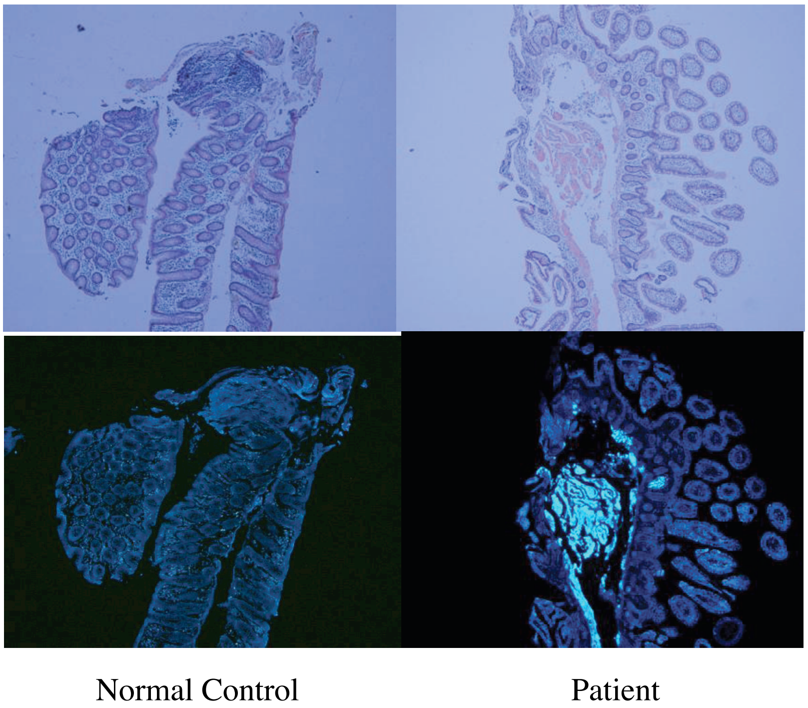
Normal Control
Patient

Figure 1. Detection of amyloid deposition in the intestines. Congo red (upper left, upper right) and BF-227 (lower left, lower right) clearly detect transthyretin in the submucosal space of the small intestine of the patient.

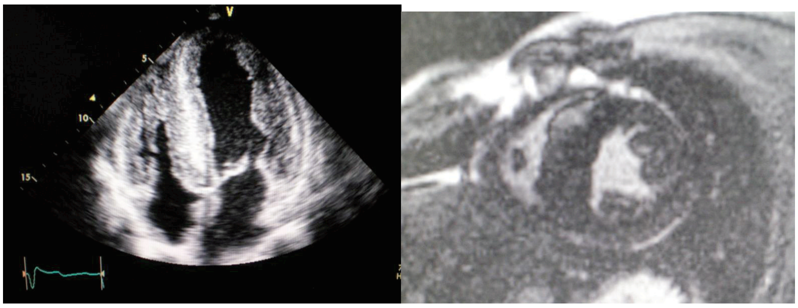

Figure 2. (Left) Echocardiographic finding. Four chamber views show symmetrical thickening of ventricular walls and septum with hyperrefractile myocardial echo (the so-called granular sparkling appearance). (Right) Contrast magnetic resonance imaging with gadolinium. Focal late gadolinium enhancement is visible.

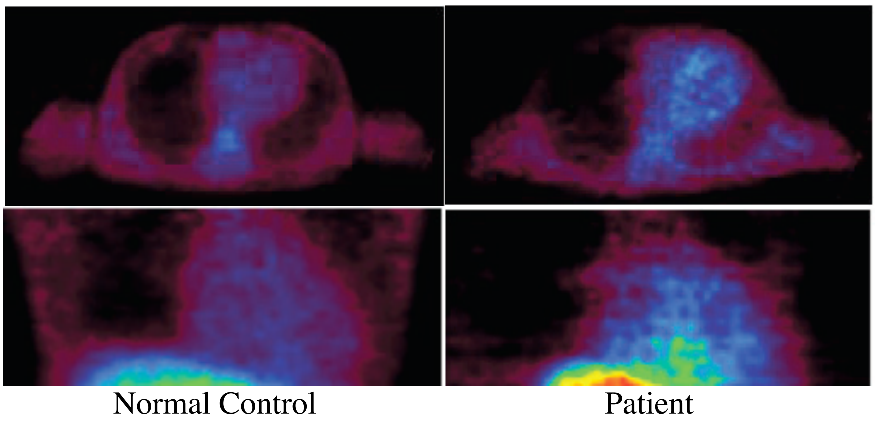
Normal Control
Patient

Figure 3. [^{11}C]BF-227-PET succeeds in visualization of amyloid deposition in the heart. Axial and coronal images are in the upper figures and the lower figures, respectively.

VIII. 2. Neural Basis of Pleasant and Unpleasant Emotions Induced by Social Reputation

Ito A.[1], Fujii T.[1], Ueno A.[1], Koseki Y.[1], Tashiro M.[2], and Mori E.[1]

[1]Department of Behavioral Neurology and Cognitive Neuroscience,
Tohoku University Graduate School of Medicine
[2]Division of Cyclotron Nuclear Medicine, Cyclotron and Radioisotope Center,
Tohoku University

The field of neuroscience has embraced emotion as an important research area[1,2)]. Recent studies have delineated the neural correlates of pleasant and unpleasant emotions induced by "social" stimuli that are relevant to complex social interactions such as reputation from others. These studies have raised the possibility that different neural networks support the processing of stimuli with pleasant and unpleasant emotions. However, it remains to be elucidated. The main purpose of the present study was to identify brain regions involved in the processing of pleasant and unpleasant emotions induced by positive and negative social reputations from others.

Sixteen male volunteers with no history of neurological or psychiatric disease participated in this study (mean age 21.7 years, range 20-25 years). Each experimental stimulus presented during PET scanning consisted of a face photograph in monochrome and a word representing a social reputation in white letters (Fig. 1). During PET scanning, the subjects were asked to rate the pleasantness of each stimulus under the following four conditions: (a) a positive/like (PL) condition in which subjects were given 'positive' reputations by one of two classmates whom the subjects 'liked', (b) a negative/like (NL) condition in which subjects were given 'negative' reputations by one of two classmates whom the subjects 'liked', (c) a positive/dislike (PD) condition in which subjects were given 'positive' reputations by one of two classmates whom the subjects 'disliked', and (d) a negative/dislike (ND) condition in which subjects were given 'negative' reputations by one of two classmates whom the subjects 'disliked' (Fig. 1). Subjects were told to imagine that a sentence including an adjective presented below the face photograph was the social reputation from the person to the subject.

Regional cerebral blood flow (rCBF) was measured with PET (SET2400W Shimadzu, Kyoto, Japan; FWHM = 4.0 mm) using ^{15}O-labeled water (approximately 180 MBq for each injection). A transmission scan was followed by the experiment, and these data were used to obtain corrected emission images. A T1-weighted MRI (3T) was obtained on a separate occasion for coregistration in spatial preprocessing. The PET data were analyzed with statistical parametric mapping (SPM8) (Wellcome Department of Imaging Neuroscience, London, UK). Contrast of the main effect of each voxel was assessed using t-statistics, resulting in a statistical image. The threshold of significance was set at $p<0.001$ (uncorrected for multiple comparisons) with an extent threshold of 10 contiguous voxels.

To investigate the neural correlates of the processing of positive social reputations, the effect of a positive emotional valence of social reputation [(PL + PD) - (NL + ND)] was calculated. This analysis revealed significant activation in the orbitofrontal cortex (Fig. 2A). Next, we investigate the effect of a negative emotional valence of social reputation [(NL + ND) - (PL+ PD)]. This analysis revealed significant activation in the amygdala (Fig. 2B).

We found that the orbitofrontal cortex was activated by positive reputations relative to negative reputations. The orbitofrontal cortex is associated with reward processing and hedonic experiences3,4). The present findings are also consistent with the findings of a recent study showing that being liked activates reward-related regions including the ventromedial prefrontal cortex5).

We also found that the amygdala was activated by negative reputations relative to positive reputations. The present results are consistent with the study by Kim et al. showing that amygdala activity was associated with imagining derogatory appraisals6). The results of Kim et al. and the present study suggest that amygdala activity is associated with the processing of not only typical experimental stimuli, such as pictures or words, but also stimuli related to social interactions including reputation from others.

References

1) LeDoux J.E., Annu. Rev. Neurosci. **23** (2000) 155.
2) Ito A., Fujii T., Ueno A., Koseki Y., Tashiro M., Mori E., Neuroreport **22** (2011) 679.
3) Kringelbach M.L., Nat. Rev. Neurosci. **6** (2005) 691.
4) London E.D., Ernst M., Grant S., Bonson K., Weinstein A., Cereb. Cortex **10** (2000) 334.
5) Davey C.G., Allen N.B., Harrison B.J., Dwyer D.B., Yucel M., Hum. Brain Mapp. **31** (2010) 660.
6) Kim J.W., Choi E.A., Kim J.J., Jeong B.S., Kim S.E., Ki S.W., Neurosci. Lett. **446** (2008) 1.

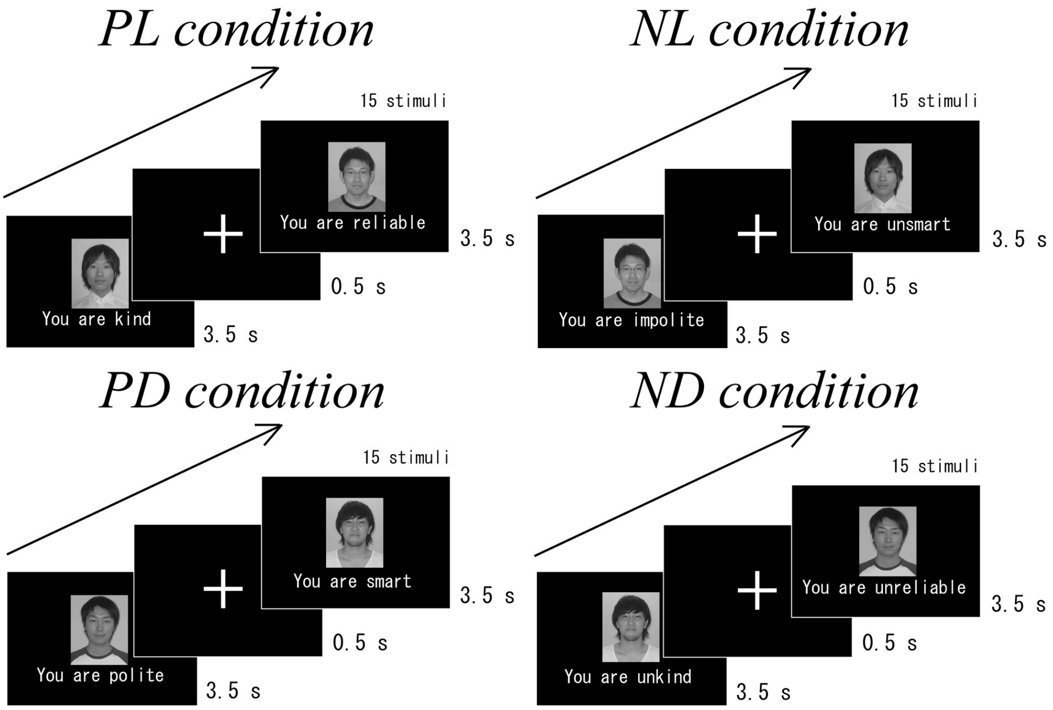

Figure 1. Schematic drawing of the four experimental conditions in the present study. These four conditions were varied as a function of the emotional valence of social reputation (positive vs. negative) and the likability of the person (like vs. dislike). PL, positive/like; PD, positive/dislike; NL, negative/like; ND, negative/dislike.

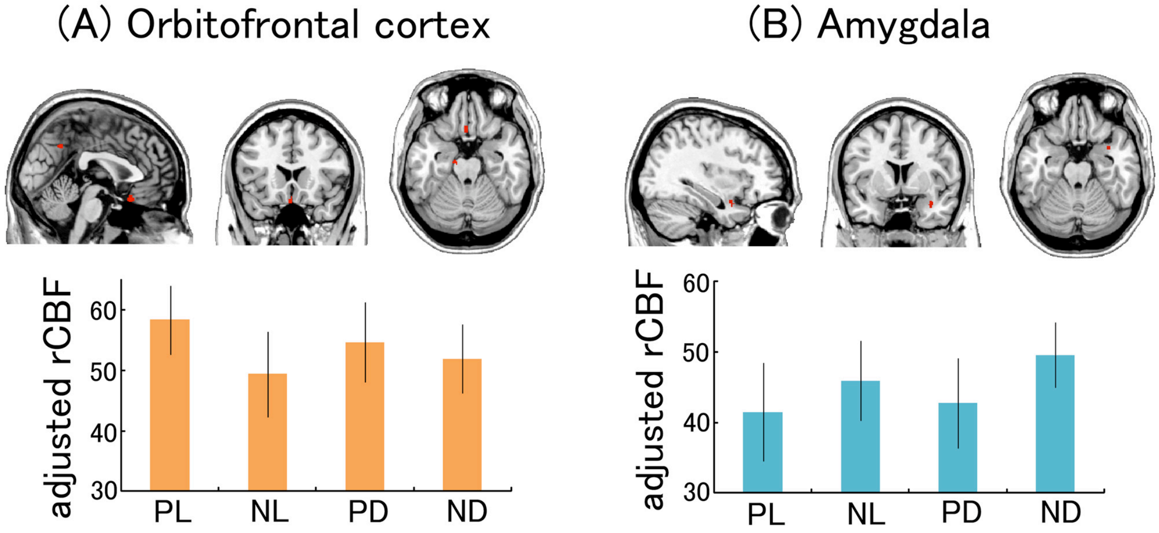

Figure 2. (A) Patterns of rCBF in the orbitofrontal cortex during the four conditions. The activation map was obtained as the main effect of the positive emotional valence of social reputation (positive > negative) in the SPM whole-brain analysis. (B) Patterns of rCBF in the right amygdala during the four conditions.

VIII. 3. Simultaneous Measurement of Regional Cerebral Blood Flow Changes Using [^{15}O]H_2O-PET and Functional Near-Infrared Spectroscopy (fNIRS): A Pilot Study

Tashiro M.[1]*, Hiraoka K.*[1]*, Watanuki S.*[1]*, Ishikawa Y.*[2]*, Miyake M.*[1]*, Masud MM.*[1]*, Ishikawa A.*[3]*,*
Inoue Y.[3]*, and Yanai K.*[1]

[1]*Divisions of Cyclotron Nuclear Medicine, Cyclotron And Radioisotope Center, Tohoku University*
[2]*Division of Radiopharmaceutical Chemistry, Cyclotron And Radioisotope Center, Tohoku University*
[3]*R&D department, Medical Systems Division, Shimadzu Corporation*

Introduction

We can use positron emission tomography (PET) as a methodology of functional neuroimaging to measure the cerebral metabolic rate of glucose (CMRglc), cerebral blood flow (CBF) and transmitter-receptor interaction, etc. (Fig. 1). In order to measure the CMRglc, a radioactive analogue of glucose, [^{18}F]fluorodeoxyglucose ([^{18}F]FDG) is used. In certain activated brain regions, the demand for glucose and oxygen may increase due to the increased regional brain energy metabolism, resulting in the dilatation of cerebral capillaries. This capillary dilatation can be observed as an increased regional CBF (rCBF). The rCBF can be measured using PET and radio-labeled water ([^{15}O]H_2O) (Fig. 1). Recently, however, other radiation-free methods such as functional magnetic resonance imaging (fMRI) and functional near-infrared light spectroscopy (fNIRS) have also been applied to the measurement of rCBF (Fig. 1). In addition, in the human brain, neurotransmitters can manifest their potent effects even with very small amounts. Activities of neurotransmitters can also manifest their effects even in very small amounts. It is not easy to visualize the actions of neurotransmitters in the living human brain without using a highly sensitive technique such as PET (Fig. 1)1).

Though the PET method is still in active use for measuring CMRglc and for evaluating neurotransmission function, PET measurement of rCBF has been almost replaced by fMRI and fNIRS. The most important disadvantage of PET would be its low temporal resolution. Therefore, the combination of PET and fMRI or fNIRS would make sense2-5).

Materials and Methods

One healthy volunteer man was scanned using both fNIRS and [^{15}O]H_2O PET for evaluation of regional cerebral blood flow changes. fNIRS device use here was OMM-3000 (Shimadzu Co., Ltd., Kyoto, Japan: Fig. 2) and PET scanner used here was SET-2400W (Shimadzu Co., Ltd., Kyoto, Japan). Three conditions such as 1) resting, 2) word generation task in which outputs were vocalized (Word Voice), and 3) not vocalized (Word Silent). Statistical examination was done using single subject conditions & covariates menu to produce the contrast "Word silent – resting" and "Word Voice – resting" for both fNIRS and PET data (Fig. 3).

Results

In the result of PET data, there was a trend for more activation in the left frontal region in both Word Silent and Word Voice tasks. However, in the results of fNIRS data, there was a trend for more activation of the left frontal region in Word Voice task, but not in Word Silent task. Rather prominent activation was observed in the right hemisphere of Word Silent task, that was finally judged as an artifact (Fig. 3).

Discussion

While some findings were commonly observed in the fNIRS and PET, the findings were not the same. It seemed to be reasonable that the left hemisphere demonstrated the trend for more activation in Word Voice task both in fNIRS and PET. Using the current system, it was hard to directly compare the location of statistical peaks in fNIRS and PET because the fNIRS images and PET images were normalized differently. For the better coregistration, a digitizer system should be introduced.

Acknowledgements

This pilot study was partly supported the grant-in-aids from the Ministry of Health, Welfare and Labor for Amyloid imaging, JST grant for education and research for molecular imaging. The authors thank to all the staffs of Cyclotron and Radioisotope Center, Tohoku University, for the operation of cyclotron and patients care.

References

1) Tashiro., et al., Annals of nanoBME **4** (2010) 91.
2) Hoshi Y., et al., Neurosci. Lett. **172** (1994) 129.

3) Villringer K., et al., Adv. Exp. Med. Biol. **413** (1997) 149.
4) Rostrup E., et al., Brain Res. **954** (2002) 183.
5) Vas A., et al., J. Neurol. Sci. **203** (2002) 259.

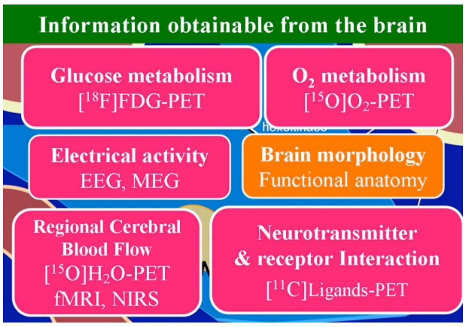

Information obtainable from the brain

Glucose metabolism
[^{18}F]FDG-PET

O_2 metabolism
[^{15}O]O_2-PET

Electrical activity
EEG, MEG

Brain morphology
Functional anatomy

Regional Cerebral Blood Flow
[^{15}O]H_2O-PET
fMRI, NIRS

Neurotransmitter & receptor Interaction
[^{11}C]Ligands-PET

Figure 1. Information available from the living human brain. The most important energy resource of the human brain is glucose. Oxygen is necessary for glucose metabolism. These substances are supplied by the blood stream. Brain regions with increased activity are accompanied by increased regional cerebral blood flow. Information regarding glucose and oxygen metabolism can be obtained using PET. (Reproduced from the reference 1)

Figure 2. A NIRS device, OMM-3000 (Shimadzu, Co. Ltd., Kyoto, Japan), currently being used at CYRIC, Tohoku University.

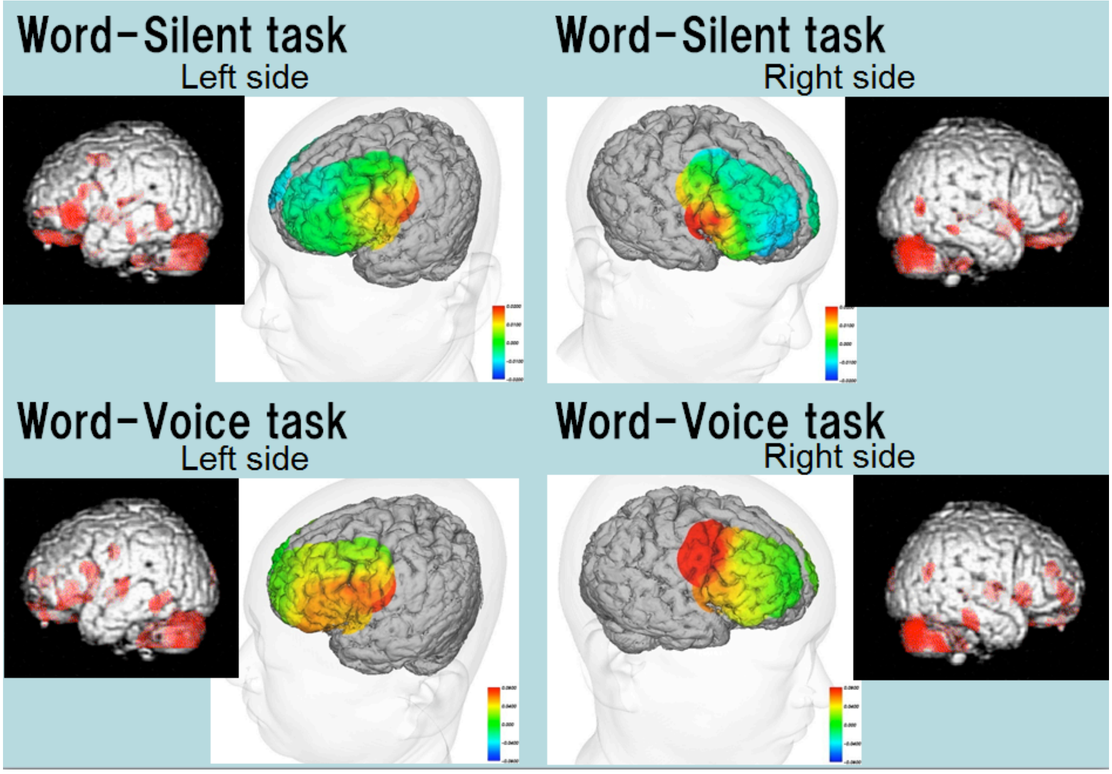

Figure 3. Regional activation pattern of NIRS and PET with [^{15}O]H_2O in the left and right hemispheres (sides) of the brain separately.

VIII. 4. Donepezil Binding to Acetylcholinesterase and Response to Donepezil Therapy in Parkinson's Disease Dementia: [5-^{11}C-*methoxy*]Donepezil-PET Study

Hiraoka K.[1]*, Okamura N.*[2]*, Funaki Y.*[3]*, Hayashi A.*[4]*, Tashiro M.*[1]*, Hisanaga K.*[5]*,*
Fujii T.[4]*, A Takeda.*[6]*, Yanai K.*[2]*, Iwata R.*[3]*, and Mori E.*[4]

[1]*Cyclotron And Radioisotope Center, Tohoku University*
[2]*Department of Pharmacology, Graduate School of Medicine Tohoku University*
[3]*Division of Radiopharmaceutical Chemistry, Cyclotron and Radioisotope Center, Tohoku University,*
[4]*Department of Behavioral Neurology and Cognitive Neuroscience, Graduate School of Medicine Tohoku University*
[5]*Departments of Neurology and Clinical Research, Miyagi National Hospital*
[6]*Department of Neurology, Tohoku University Graduate School of Medicine*

The cholinergic system is one of the most crucial neurotransmitter systems in the brain and is implicated in dementia. The activities of both choline acetyltransferase, which catalyzes acetylcholine synthesis, and acetylcholinesterase (AChE), which degrades brain acetylcholine, are reported to be decreased in the neocortex and hippocampus in Alzheimer's disease (AD) and Parkinson's disease with dementia (PDD), and this decreased activity correlates with the severity of cognitive impairment. Moreover, loss of cholinergic neurons in the nucleus basalis of Meynert has been reported in the brains of AD and PDD patients. On the basis of these pathological findings, reversible AChE inhibitors have been used to potentiate cholinergic neurotransmission, with the aim of improving cognitive function. Currently, several AChE inhibitors are prescribed to patients with dementia. Among them, donepezil hydrochloride has proven effective in ameliorating the cognitive impairment of demented patients.

[5-^{11}C-methoxy]Donepezil ([^{11}C]donepezil) was developed for the in vivo visualization of donepezil binding to AChE and cholinergic imaging using positron emission tomography (PET)1). An animal study by Funaki et al.2) and a pilot study by Okamura et al.3), which applied [^{11}C]donepezil-PET to AD patients, showed that [^{11}C]donepezil holds promise as a potential agent for imaging AChE in vivo using PET. To exploit the use of [^{11}C]donepezil-PET in clinical research, the kinetic analysis of

[^{11}C]donepezil was established using dynamic 60-min PET scans acquired after intravenous injection of [^{11}C]donepezil in 6 healthy subjects$^{3)}$.

Subsequently, we applied donepezil-PET imaging to PDD patients. Twelve patients with PDD (9 men, 3 women; mean age ± SD, 69.8 ± 6.4 years) and 13 healthy control subjects matched for age, sex, and education (10 men, 3 women; mean age ± SD, 69.5±6.7 years) were enrolled. The patients met the diagnosis of PD according to the diagnostic criteria of the UK PD Society Brain Bank, based on clinical, laboratory, and radiological findings. To select subjects with dementia, patients with a score of 1 or above on at least one of the sub-items of the Clinical Dementia Rating (CDR) were included in this study. For patients with Parkinson's disease with dementia, daily administration of donepezil was started after [^{11}C]donepezil-PET imaging and continued for 3 months. At baseline and after 3 months of donepezil therapy, cognitive function was evaluated. The Ethics Committee of Tohoku University School of Medicine approved the study protocol, and written informed consent was obtained from all healthy subjects and from patients or their family members.

Radiosynthesis of the [^{11}C]donepezil and the PET procedures used are described elsewhere$^{1,3)}$. The acquired PET and metabolite-corrected blood data were analyzed using the software PMOD (PMOD Technologies) and parametric 3D maps of total distribution volume (tDV) in the brain were generated using the classical Logan plot. Images were analyzed using SPM8 (Wellcome Department of Cognitive Neurology) and ImageJ 1.42q (National Institutes of Health, Bethesda, MD).

The tDVs of the total cerebral cortices were estimated using a semi-automatic method. Axial 3D magnetic resonance images were obtained for anatomical reference, which were segmented into gray and white matter using the prior probability templates of SPM8. The total cerebral cortices in the probability maps of the gray matter were extracted by tracing with a manually driven mouse cursor on ImageJ and then co-registered with the tDV images. The co-registered images were used as a mask of the cerebral cortices, and were projected onto the tDV images of each subject to extract the cerebral cortices. Finally, the mean tDV value of the cerebral cortices was calculated. A two-tailed t-test was used for group comparison with statistical significance set at $p < 0.05$.

A between-group comparison examining the difference in tDV values at voxel level was performed using analysis of covariance (ANCOVA) with the software SPM8, with sex, age, and education as covariates in an explorative analysis covering the whole brain without any a-priori hypothesis. Statistical significance was set at $p < 0.005$ without correction for multiple comparisons, and cluster extent threshold was 100 voxels.

The mean tDVs of the cerebral cortices in the PDD group were significantly lower, showing a mean decrease rate of 22.7%, than those of the control group (PDD, 7.9±2.2; NC, 10.2± 2.7). In the SPM analysis, the PDD group exhibited a widespread tDV reduction as compared with the control group (Fig. 1). The mean total distribution volume of the patients with PDD was significantly correlated with improvement of visuoperceptual function after 3 months of donepezil therapy (Table 1).

The use of [^{11}C]donepezil-PET in the present clinical study of PDD revealed that AChE in the cerebral cortices was decreased. Among previous studies of cholinergic PET imaging utilizing radiolabeled acetylcholine analogues, such as [^{11}C]PMP, Hilker et al4). and Bohnen et al5). found a 20.0-29.7% and a 10.7-12.9% reduction in cortical acetylcholinesterase activity in Parkinson's disease with and without dementia, respectively, compared with normal subjects. The reduction rate of the mean tDV value of the cerebral cortices in the PDD group in the present study was similar to that of cortical acetylcholinesterase activity reported in these previous studies. Voxel-by-voxel analysis using SPM8 revealed a global reduction in acetylcholinesterase density in the brains of PDD patients, similar to the results of previous studies. The results also suggested that donepezil therapy is more effective in patients with less decrease in acetylcholinesterase, which indicates relative preservation of the cholinergic system.

References

1) Funaki Y., Kato M., Iwata R., et al., J. Pharmacol. Sci. **91** (2003) 105.
2) Okamura N., Funaki Y., Tashiro M., Kato M., Ishikawa Y., Maruyama M., Ishikawa H., Meguro K., Iwata R., Yanai K., Br. J. Clin. Pharmacol. **65** (2008) 472.
3) Neuroimage **46** (2009) 616.
4) Hilker R., Thomas A., Klein J., Weisenbach S., Kalbe E., Burghaus L., Jacobs A.H., Herholz K., Heiss W.D., Neurology **65** (2005)1716.
5) Bohnen N., Kaufer D., Ivanco L., Lopresti B., Koeppe R., Davis J., Mathis C.A., Moore R.Y., DeKosky S.T., Arch. Neurol.**60** (2003)1745.

Table 1. Correlation matrix contrasting mean distribution volume of the cerebral cortices against the change in the cognitive tests after 3-month donepezil therapy.

	change			
	MMSE	digit span (WAIS-R)	fluency	TMT-A
correlation coefficient	-0.207	-0.036	0.165	0.116
P	0.593	0.928	0.672	0.827

	change			
	recall task (ADAS)	recognition TASK (ADAS)	visuoperceptual test	NPI
correlation coefficient	-0.406	0.207	0.837	-0.091
P	0.278	0.594	0.005	0.817

MMSE=MIni-MentalState Fxamination; WAIS-R=Wechsler Adalt Intelligence Scale-Revised; TMT-A=Trail-Making Tesst-A: ADAS=Alzhheimer's Disease Assessment Scale;NPI= Neuropsychiatric Inventory

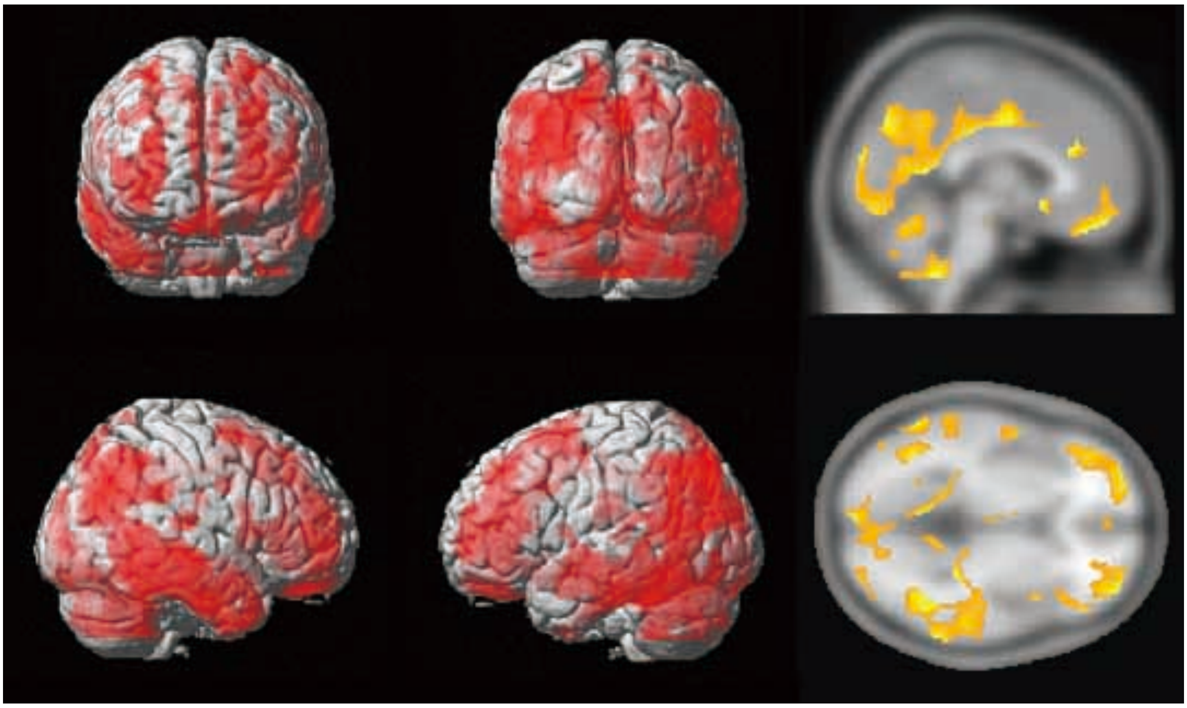

Figure 1. Statistical parametric maps of a significant decrease in [^{11}C]donepezil distribution volume in the PDD group as compared with the normal control group ($p_{\text{uncorrected}}$ <0.005).

VIII. 5. Medical Imaging and Scientific Visualization

Tashiro M.[1]*, Narashima T.*[2]*, Hiraoka K.*[1]*, Yanai K.*[1,3]*, Nagami F.*[3]

[1]*Divisions of Cyclotron Nuclear Medicine, Cyclotron And Radioisotope Center, Tohoku University*
[2]*Tane+1 LLC, New York, United States,*
[3]*Tohoku University Graduate School of Medicine*

Introduction

Modern medical imaging technology has been greatly advanced in the last several decades based on the rapid advancement of engineering and information sciences. In recent years, three-dimensional imaging has become a vital tool in medical diagnosis and treatment planning. Scientific visualization techniques may include whole biomedical imaging methods such as X-ray computed tomography (CT), magnetic resonance imaging (MRI), positron emission tomography (PET), single photon emission computed tomography (SPECT), near-infrared spectroscopy (NIRS), topographic electroencephalography (EEG), magnetoencephalography (MEG), mammography and ultrasonography (US). More invasive methods such as gastroscopy, colonoscopy, laparoscopy and bronchoscopy would be also a part of medical visualization techniques. Biomedical visualization at cellular level may cover histological and pathological examination using light microscopy and electron microscopy, etc. At the CYRIC, great emphasis has been put on the promotion of molecular and functional imaging research using PET. In addition, professional education on molecular and functional imaging has been done for students of master's and doctoral courses based on the framework of "Molecular Imaging Educational Course" of Tohoku University, Graduate school of Medicine, in collaboration to other faculties such as Graduate Schools of Engineering, Pharmaceutical Sciences, Dentistry, Medical Engineering(1).

Although the biomedical imaging is a part of scientific visualization, the actual field of scientific visualization has been recognized as a much broader field including computer graphics, simulation, infographics, scientific/biomedical illustration, movie and animation. Not only the movie and animation for scientific education but also scientific art works are also parts of scientific visualization. This broader scientific visualization has been an essential part of effective communication between researchers and the society, especially in promoting the general public's understanding of scientific research outputs. This trend has been getting much more intense especially after the East Japan Earthquake and Fukushima Daiichi Nuclear Plant Accident in 2011. It has been said, however, Japanese educational system has not put much emphasis on this field in contrast to the situation in other western countries.

History and Current Situation of Education in The World

History of education on scientific/biomedical visualization/illustration is already long in western countries, especially, in the United States. In the late 1890s, a German artist, Max Broedel started working as a medical illustrator for notable investigators such as Harvey Cushing (a neurosurgeon) and William Halstead (a neurosurgeon) at Johns Hopkins University, Baltimore2). In 1911, he established the first academic department of medical illustration in the School of Medicine of the Johns Hopkins University3). The department has continued to train many medical illustrators until now. And it is said that his graduates have founded a number of other academic programs across the world3). Currently, there are many educational programs of scientific/biomedical visualization in North America. Representative programs are running at University of Toronto4), Toronto, Canada, and at Georgia Health Science University, University of Illinois, University of Texas, California State University, etc.

Current Situation of Education in Japan

To the best of authors' knowledge, there has been no official university educational course in Japan. At Tohoku University, first in Japan, the "1st Scientific Illustration Summer School" was held in 2010 in collaboration with Department of Biomedical Communications, University of Toronto, and the "2nd Scientific Illustration Summer School" was held in 2011 in collaboration with Department of Art as applied to Medicine, Johns Hopkins University, mainly by the effort of F. Nagami of Tohoku University, Graduate School of Medicine, and T. Narashima of Tane+1 LLC, USA5). T. Narashima is a professional scientific illustrator who has been contributing for many scientific journals such as Science and Scientific American, as well as textbooks of physiology, biochemistry, molecular biology (Fig. 1).

In the fall of 2011, "Scientific illustration Exhibition in Sendai 2011" was additionally held in Tohoku University at a book café of Tohoku University COOP (November 23 to 25th, 2011), where a few hundreds of illustrative works were exhibited. These were professional works by graduates of Johns Hopkins University and University of Toronto, as well as the works by participants to the 2 summer schools in Sendai (Fig. 2 and 3). A special seminar on "scientific/biomedical visualization/illustration" was also held on November 24th in collaboration with global COE program (Global Nano-Biomedical Engineering Education and Research Network Centre)[6) and Molecular Imaging Educational Program of Graduate School of Medicine, Tohoku University (Fig. 4)[1). Many students and professors visited the exhibition (estimated to be more than a thousand visitors). Many young researchers and professors participated in the special seminar and had a hot discussion. It seems that not a few researchers have already had been interested in scientific/biomedical illustration and have understood the importance of this interdisciplinary field.

The authors hope that an official university course on scientific/biomedical visualization/illustration will be started in near future in Japan as well.

References

1) http://www.miec.umin.jp/
2) Ranice W.Crosby, John Cody, (1991). Max Brödel: The Man Who Put Art Into Medicine. Berlin: Springer.
3) http://www.hopkinsmedicine.org/medart/
4) http://www.bmc.med.utoronto.ca/bmc/index.php
5) http://www.taneplus1.com/
6) http://www.nanobme.org/en/index.html
7) Frontiers in biology. Cellular membranes. Science **258** (1992) 861.
8) Principles of Human Physiology. 1st Ed. by William J. Germann and Cindy L. Stanfield.
9) Benjamin-Cummings Publishing Company. 2002.

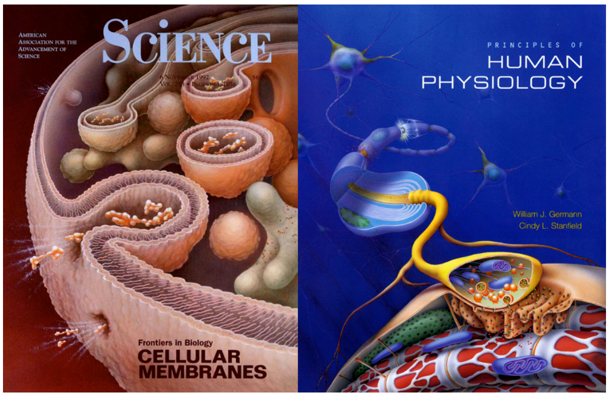

Figure 1. Sophisticated scientific/biomedical illustrations by Mr. Tomo Narashima, a professional illustrator. A cover illustration for a special issue of “Science” journal on cellular membranes (LEFT), and a cover illustration for a renowned medical textbook “Principles of Human Physiology” (RIGHT). Reproduced by the courtesy of Mr. Tomo Narashima.

Figure 2. Landscape of "Scientific illustration Exhibition 2012 in Sendai” held in Tohoku University at a book café "BOOOK" of Tohoku University COOP. Many artworks were exhibited by courtesy of John's Hopkins University, University of Toronto and Tane+1 LLC. Photo by Ms. Y. Sato.

Figure 3. A scene of "Scientific illustration Exhibition 2011 in Sendai”. Discussion between a visitor and Mr. Tomo Narashima, an scientific illustrator in USA, in front of a medical illustrative work by one of students of "2nd Scientific Illustration Summer School in Sendai 2011" during a guided tour of the exhibition (November 24th). Photo by Ms. Y. Sato.

Figure 4. A scene of seminar on scientific/biomedical visualization/illustration (in Japanese). The speaker was Mr. Tomo Narashima, an scientific illustrator who have a great number of contributions to many well-known scientific journals such as Science and Scientific American, and many biomedical textbooks. He visited CYRIC on November 24th. Photo by Ms. Y. Sato.

IX. 1. Beginners Training for Safe Handling of Radiation and Radioisotopes in Tohoku University

Yamazaki H., Baba M., Miyata T., Ohtomo K., Mayama F., and Yuki H.

Cyclotron and Radioisotope Center, Tohoku University

During 2010, the beginners training for safe handling of radiation and radioisotopes in Tohoku University was conducted in three courses as usual: 1) Radiation and Isotopes, 2) X-ray Machines and Electron Microscope, and 3) Synchrotron Radiation (SOR). The training was held twice a year, in May and November, under the help for lectures and practice from various departments and research institutes of the university.

During 2011, only the training for "X-ray machines and electron microscopes" was held twice a year, in July and November. The trainings for "Radiation and Radioisotopes" and "Synchrotron Radiation" were held only once a year, in November, owing to the Tohoku Region Pacific Coast Earthquake.

Lectures in English which were started in November of 2002 were continued for students and/or researchers who are not so familiar with Japanese language, by using PC projector and text of copies of view graphs (English class). The membership of the English class is almost constant as shown later.

The training for "Radiation and Radioisotopes" is for persons who use unshielded radioisotopes and accelerators, and has been conducted from 1977. The contents of lectures and practices are shown in Table 1. The departments or institutes to which trainees belong and the distributions of trainees are shown in Table 2 and Table 3.

The training for "X-ray machines and electron microscopes" started at the end of 1983. The training is scheduled at the same time as that for "Radiation and Radioisotopes". In this course, only lectures are given with no practice. The contents of lectures are shown in Table 4. The departments or institutes to which trainees belong and the distributions of trainees are shown in Table 5 and Table 6.

The training for "Synchrotron Radiation" began at the end of 1995. The contents of the lectures are the same as those of the "Radiation and Radioisotopes" but no practice. The departments or institutes to which trainees belong and the distributions of trainees are shown in Table 7 and Table 8.

Table 1. Contents of the lectures and practices for "Radiation and Radioisotopes" in 2010 and 2011.

Lectures (one day)	Hours
Introduction to radiation	0.5
Effects of radiation on human	1.0
Radiation physics and measurements	1.0
Chemistry of radioisotopes	1.0
Radiological protection ordinance including video	1.5
Safe handling of radioisotopes	1.5

Practices (one day)	Hours
Treatment of unsealed radioactive solution	4.0
Measurement of surface contamination and decontamination	1.0
Measurement of gamma-rays and beta-rays	2.0

Table 2. Distribution of trainees for “Radiation and Radioisotopes” in 2010.

Department	Staff	Student	Total	English class
CYRIC	1	8	9	2
Medicine	15	56	71	1
Dentistry	2	23	25	0
Pharmacy	0	45	45	3
Science	3	38	41	11
Engineering	7	103	110	6
Agriculture	2	57	59	0
Research Institutes	8	91	99	9
The others	0	0	0	0
Total	38	421	459	32

Table 3. Distribution of trainees for “Radiation and Radioisotopes” in 2011.

Department	Staff	Student	Total	English class
CYRIC	0	9	9	0
Medicine	4	23	27	1
Dentistry	2	11	13	0
Pharmacy	0	45	45	3
Science	1	25	26	5
Engineering	6	84	90	10
Agriculture	1	12	13	1
Research Institutes	11	61	72	4
The others	0	0	0	0
Total	26	271	297	22

Table 4. Contents of the lectures for “X-ray machines and Electron microscopes” in 2010 and 2011.

Lectures (one day)	Hours
Safe handling of X-ray machines	1.5
Radiological protection ordinance	0.5
Video for safe handling of radiation and radioisotopes	0.5

Table 5. Distribution of trainees for “X-ray machines and Electron microscopes” in 2010.

Department	Staff	Student	Total	English class
CYRIC	0	0	0	0
Medicine	3	5	8	0
Dentistry	0	1	1	0
Pharmacy	1	2	3	0
Science	4	31	35	7
Engineering	10	132	142	9
Agriculture	0	0	0	0
Research Institutes	39	114	153	31
The others	0	0	0	0
Total	57	285	342	47

Table 6. Distribution of trainees for “X-ray machines and Electron microscopes” in 2011.

Department	Staff	Student	Total	English class
CYRIC	0	0	0	0
Medicine	0	11	11	0
Dentistry	0	4	4	0
Pharmacy	1	3	4	0
Science	3	30	33	3
Engineering	9	133	142	0
Agriculture	1	0	1	0
Research Institutes	33	88	121	15
The others	0	0	0	0
Total	47	269	316	18

Table 7. Distribution of trainees for “Synchrotron radiation” in 2010.

Department	Staff	Student	Total	English class
CYRIC	0	0	0	0
Medicine	0	0	0	0
Dentistry	0	0	0	0
Pharmacy	0	0	0	0
Science	0	8	8	1
Engineering	4	24	28	2
Agriculture	0	0	0	0
Research Institutes	6	39	45	10
The others	0	0	0	0
Total	10	71	81	13

Table 8. Distribution of trainees for “Synchrotron radiation” in 2011.

Department	Staff	Student	Total	English class
CYRIC	0	0	0	0
Medicine	0	0	0	0
Dentistry	0	1	1	0
Pharmacy	1	0	1	0
Science	0	6	6	0
Engineering	0	5	5	0
Agriculture	0	0	0	0
Research Institutes	7	15	22	13
The others	0	0	0	0
Total	8	27	35	13

IX. 2. Radiation Protection and Management

Yuki H.[1]*, Miyata T.*[1]*, Ohtomo K.*[1]*, Yamazaki H.*[1]*, Baba M.*[1]*, and Nakae H.*[2]

[1]*Cyclotron and Radioisotope Center, Tohoku University*
[2]*Japan Environment Research Co., Ltd.*

(1) Overview

In the fiscal year of 2010, research and education in CYRIC were conducted as active as usual before the Tohoku Region Pacific Coast Earthquake.

Because of the earthquake, various facilities in CYRIC were damaged, and the utilization of RI was stopped.

(2) Unsealed radio nuclides used in CYRIC

The species and amounts of unsealed radio nuclides handled in CYRIC during the fiscal year of 2010 are summarized in Table 1. The table includes the isotopes produced by the cyclotron as well as those purchased from the Japan Radio Isotope Association or taken over from other radioisotope institutes.

(3) Radiation exposure dose of individual worker

The exposure doses of the workers in CYRIC during 2010 are given in Table 2. The doses were sufficiently lower than the legal dose limits.

(4) Radiation monitoring of the workplace

Radiation dose rates inside and outside of the controlled areas in CYRIC were monitored periodically and occasionally when needed. They were generally below the legal dose limits although there are several “hot spots” in mSv/hr range like slits or beam stopper of the 930 cyclotron and so on. Surface contamination levels of the floors inside the controlled areas were also measured with a smear method and a survey meter method. They were under the legal regulation levels.

(5) Wastes management

The radioactive wastes were delivered to the Japan Radio Isotope Association in the fiscal year of 2010.

The concentration of radioisotopes in the air released from the stack after filtration was monitored with stack gas monitors. The values of concentration were well below the legal regulation levels.

The radioactive water was stocked in the tanks at least for 3 days and then released to the sewerage after confirming that the concentration was lower than the legal regulation levels.

Radioactive organic scintillator waste was treated periodically by the incinerator.

Table 1. Unsealed radioisotopes used in each building of CYRIC during the fiscal year of 2010.

(a) Cyclotron Building (kBq)

Group1,2		Group 3		Group4	
		^{11}C	504,158,300.000	^{18}F	1,124,703,800.000
Total	0	Total	504,158,300.000	Total	1,124,703,800.000

(b) Radio-isotope Building (kBq)

Group 2		Group 3		Group4	
^{125}I	442,950.840	^{11}C	9,538,600.000	^{14}C	1,853.700
		^{28}Mg	1,000.000	^{18}F	369,785,400.000
		^{32}P	326,420.900	^{3}H	17,048.600
		^{124}I	651,712.840		
Total	442,950.840	Total	10,517,733.740	Total	369,804,302.300

(c) Research Building (kBq)

Group1,2		Group 3		Group 4	
		^{11}C	6,364,000.000	^{18}F	13,978,600.000
		^{15}O	5,180,000.000		
Total	0	Total	11,544,000.000	Total	13,978,600.000

Table 2. Occupational radiation exposures at CYRIC during the fiscal year of 2010.

Dose range (mSv)	Number of individuals
No measurable exposure	39
0.0 - 1.0	7
1.0 - 2.0	4
2.0 - 3.0	0
3.0 - 4.0	0
4.0 - 5.0	2
Total number of persons monitored	52

X. PUBLICATIONS

[781] Electrochemical concentration of no-carrier-added [^{18}F]fluoride from [^{18}O]water in a disposable microfluidic cell for radiosynthesis of 18F-labeled radiopharmaceuticals.
H. Saiki, R. Iwata, H. Nakanishi, R. Wong, Y. Ishikawa, S. Furumoto, R. Yamahara, K. Sakamoto, E. Ozeki.
Appl. Radiat. Isot., **68** (2010) 1703-0708.

[782] Long-term performance evaluation of positron emission tomography: analysis and proposal of a maintenance protocol for long-term utilization
S. Watanuki, M. Tashiro, M. Miyake, Y. Ishikawa, M. Itoh, K. Yanai, Y. Sakemi, H. Fukuda, K. Ishii.
Ann. Nucl. Med., **24** (2010) 461-468.

[783] Amyloid PET in mild cognitive impairment and Alzheimer's Disease with BF-227: comparison to FDG-PET.
K. Furukawa, N. Okamura, M. Tashiro, M. Waragai, S. Furumoto, R. Iwata, K. Yanai, Y. Kudo, H. Arai.
J. Neurol., **257** (2010) 721-727.

[784] In vivo visualization of α-synuclein deposition by carbon-11-labelled 2-[2-(2-dimethylaminothiazol-5-yl)ethenyl]-6-[2-(fluoro)ethoxy]benzoxazole positron emission tomography in multiple system atrophy.
A. Kikuchi, A. Takeda, N. Okamura, M. Tashiro, T. Hasegawa, S. Furumoto, M. Kobayashi, N. Sugeno, T. Baba, Y. Miki, F. Mori, K. Wakabayashi, Y. Funaki, R. Iwata, S. Takahashi, H. Fukuda, H. Arai, Y. Kudo, K. Yanai, Y. Itoyama.
Brain, **133** (2010) 1772-1778.

[785] In vivo detection of prion amyloid plaques using [^{11}C]BF-227 PET
N. Okamura, Y. Shiga, S. Furumoto, M. Tashiro, Y. Tsuboi, K. Furukawa, K. Yanai, R. Iwata, H. Arai, Y. Kudo, Y. Itoyama, K. Doh-ura.
Eur. J. Nucl. Med. Mol. Imaging, **37** (2010) 934-941.

[786] Neural correlates of forgiveness for moral transgressions involving deception.
Akiko Hayashi, Nobuhito Abe, Aya Ueno, Yayoi Shigemune, Etsuro Mori, Manabu Tashiro, Toshikatsu Fujii.
Brain Research, **1332** (2010) 90-99.

[787] Effects of emotion and reward motivation on neural correlates of episodic memory encoding: A PET study.
Y. Shigemune, N. Abe, M. Suzuki, A. Ueno, E. Mori, M. Tashiro, M. Itoh, T. Fujii.
Neuroscience Research, **67** (2010) 72-79.

[788] Function of the shoulder muscles during arm elevation: an assessment using positron emission tomography.
R. Omi, H. Sano, M. Ohnuma, K.N. Kishimoto, S. Watanuki, M. Tashiro, E. Itoi.
J. Anatomy, **216** (2010) 643-649.

[789] Changes in the volumes of the brain and cerebrospinal fluid spaces after shunt surgery in idiopathic normal-pressure hydrocephalus.
K. Hiraoka, H. Yamasaki, M. Takagi, M. Saito, Y. Nishio, O. Iizuka, S. Kanno, H. Kikuchi, T. Kondo, E. Mori.
J. Neurological Sciences, **296**-(2010) 7-12.

[790] Voxel-based analysis of amyloid positron emission tomography probe [^{11}C]BF-227 uptake in mild cognitive impairment and Alzheimer's disease.
H. Shao, N. Okamura, K. Sugi, S. Furumoto, K. Furukawa, M. Tashiro, R. Iwata, H. Matsuda, Y. Kudo, H. Arai, H. Fukuda, K. Yanai.
Dement Geriatr Cogn Disord, **30** (2010) 101-111.

[791] Application of positron emission tomography in physical medicine.
M. Masud, T. Fujimoto, S. Watanuki, M. Miyake, M. Itoh, M. Tashiro.
Mymensingh Med., **19** (2010) 110-115.

[792] Imaging of hypoxic lesions in patients with gliomas by using positron emission tomography with 1-(2-[^{18}F]fluoro-1-[hydroxymethyl]ethoxy)methyl-2-nitroimidazole, a new ^{18}F-labeled 2-nitroimidazole analog.
I. Shibahara, T. Kumabe, M. Kanamori, R. Saito, Y. Sonoda, M. Watanabe, R. Iwata, S. Higano, K. Takanami, Y. Takai, T. Tominaga.
J. Neurosurg., **113** (2010) 358-368.

[793] Evaluation study on properties of a novel R-BTP extraction resin –from a viewpoint of simple separation of minor actinides.
S. Usuda, R. Liu, Y. Wei, Y. Xu, H. Yamazaki, Y. Wakui.
J. Ion Exchange, **21** (2010) 35-40.

[794] Brain activity following esophageal acid infusion using positron emission tomography.
S. Kobayashi, Y. Abe, M. Tashiro, T. Koike, K. Iijima, A. Imatani, S. Ohara, S. Watanabe, S. Fukudo, T. Shimosegawa.
World J. Gastroenterology, **16** (2010) 5481-5489

[795] Next-day residual sedative effect after nighttime administration of an over-the-counter antihistamine sleep aid, diphenhydramine, measured by positron emission tomography.
D. Zhang, M. Tashiro, K. Shibuya, N. Okamura, Y. Funaki, T. Yoshikawa, M. Kato, K. Yanai.
J. Clinical Psychopharmacology, **30** (2010) 694-701.

[796] Right temporal-lobe contribution to the retrieval of family relationships in person identification.
N. Abe, T. Fujii, A. Ueno, Y. Shigemune, M. Suzuki, M. Tashiro, E. Mori.
Neurosci. Lett., **486** (2010) 10-13.

[797] Roles of hypothalamic subgroup histamine and orexin neurons on behavioral responses to sleep deprivation induced by th treadmill method in adolescent rats.
A. Xu, E. Sakurai, A. Kuramasu, J. Zhang, J. Li, N. Okamura, D. Zhang, T. Yoshikawa, T. Watanabe, K. Yanai.
J. Pharmacol. Sci., **114** (2010) 444-453.

[798] Alpha-fluoromethylhistidine, a histamine synthesis inhibitor, inhibits orexin-induced wakefulness in rats.
T. Seki, M.A. Akanmu, M. Matsuura, K. Yanai, K. Honda.
Behavioural Brain Research, **207** (2010) 151-154.

[799] Fluorine-18 radiopharmaceuticals beyond [^{18}F]FDG for use in oncology and neurosciences.
H.H. Coenen, P.H. Elsinga, R. Iwata, M.R. Kilbourn, M.R.A. Pillai, M.G.R. Rajan, H.N. Wagner, J.J. Zaknun.
Nucl. Med. Biol., **37** (2010) 727-740.

[800] Development of an adjustable beam flattening system for modification of passive beam delivery technique in proton therapy.
T.A. Esmaili, A. Terakawa, K. Ishii, H. Yamazaki, S. Matsuyama, Y. Kikuchi, H. Akiyama, K. Koyata, A. Tagawa, Y. Itoh, S. Yasunaga.
Nucl. Instru. Meth., **A 615** (2010) 138-141.

[801] Development of a digital front-end electronics for the CdTe PET systems.
M. Nakhostin, Y. Kikuchi, K. Ishii, S. Matsuyama, H. Yamazaki.
Nucl. Inst. Meth., **614** (2010) 308-312.

[802] Delivery of Na/I symporter gene into skeletal muscle using nanobubbles and ultrasound: visualization of gene expression by PET.
Y. Watanabe, S. Horie, Y. Funaki, Y. Kikuchi, H. Yamazaki, K. Ishii, S. Mori, G. Vassaux, T. Kodama.
J. Nucl. Med., **51** (2010) 951-958

[803] Energy-discriminating gadolinium K-edge X-ray computed tomography system.
H. Matsukiyo, M. Watanabe, E. Sato, A. Osawa, T. Enomoto, J. Nagao, P. Abderyim, K. Aizawa, K. Hitomi, E. Tanaka, H. Mori, T. Kawai, A. Ogawa, K. Takahashi, S. Sato, J. Onagawa.
Jpn. J. Appl. Phys., **49** (2010) 027001.

[804] Digital pulse processing for planar TlBr detectors.
N. Nakhostin, K. Hitomi, K. Ishii, Y. Kikuchi.
Nucl. Instrum. Methods in Phys. Res., **A615** (2010) 242-244.

[805] Demonstration of iodine K-edge imaging by use of an energy-discrimination X-ray computed tomography system with a cadmium telluride detector.
A. Abudurexiti, M. Kameda, E. Sato, P. Abderyim, T. Enomoto, M. Watanabe, K. Hitomi, E. Tanaka, H. Mori, T. Kawai, K. Takahashi, S. Sato, A. Ogawa, J. Onagawa.
Radiol. Phys. Technol., **3** (2010) 127-135.

[806] Energy-discriminating X-ray computed tomography system utilizing a cadmium

telluride detector.
E. Sato, P. Abderyim, T. Enomoto, M. Watanabe, K. Hitomi, K. Takahashi, S. Sato, A. Ogawae, J. Onagawa.
Nucl. Instrum. Methods in Phys. Res. **A619** (2010) 262-265.

[807] Study of activation cross sections of proton induced reactions on barium: Production of ^{131}Ba → ^{131}Cs.
F. Tarkanyi, A. Hermanne, S. Takacs, F. Ditroi, B. Kiraly, H. Yamazaki, M. Baba, A. Mohammadi, A.V. Ignatyuk.
Appl. Rad. Isot., **68** (2010) 1869-1877.

[808] Improvement of the performance of TOHOKU microbeam system.
S. Matsuyama, K. Ishii, S. Tsuboi, Y. Hashimoto, Y. Kawamura, K. Yamanaka, M. Watanabe, S. Ohkura, M. Fujikawa, G. Catella, K. Fujiki, Y. Hatori, N. Hamada, M. Fujiwara, Y. Kikuchi, H. Yamazaki.
Int. J. PIXE, **20** (2010) 11-20.

[809] Improved radiosensitive microcapsules using H_2O_2.
S. Hrada, S. Ehara, K. Ishii, H. Yamazaki, S. Matsuyama, T. Kamiya, T. Sasaki, K. Arakawa, T. Satoh, M. Oikawa.
Int. J. PIXE, **20** (2010) 21-28.

[810] Evaluation of the uptake of CDDP-containing polymeric micelles in single pancreatic cancer cells.
K. Mizuno, M. Uesaka, S. Matsuyama, K. Ishii, H. Yamazaki.
Int. J. PIXE, **20** (2010) 37-44.

[811] Measurement of elemental distributions in mouse brain by using submilli-PIXE camera.
K. Fujiki, S. Matsuyama, K. Ishii, H. Yamazaki, A. Terakawa, Y. Kikuchi, M. Fujiwara, Y. Kawamura, S. Ohkura, M. Fujikawa, G. Catella, Y. Hashimoto, Y. Hatori, N. Hamada, E. Sakurai, K. Yanai.
Int. J. PIXE, **20** (2010) 45-50.

[812] Application of micro-PIXE analysis to investigate trace elements in deciduous teeth enamel.
K. Igari, A. Takahashi, H. Ando, K. Ishi, S. Matsuyama, S. Kawamura, Y. Hashimoto, M. Fujikawa, Y. Itou, Y. Hatori, N. Hamada, H. Yamazaki.
Int. J. PIXE, **20** (2010) 51-56.

[813] PIXE Analysis of individual particles in coal fly ash.
Y. Hatori, S. Matsuyama, K. Ishii, A. Terakawa, Y. Kikuchi, H. Fujikawa, Y. Kawamura, S. Okura, M. Fujikawa, N. Hamada, K. Fujiki, C. Inoue, H. Yamazaki, Y. Hashimoto.
Int. J. PIXE, **20** (2010) 57-62.

[814] PIXE analysis of murine fibrosarcoma tumor for proton therapy combined with the chemotherapeutic agent cisplatin.
A. Terakawa, Y. Ito, K. Ishii, S. Matsuyama, Y. Kikuchi, S. Yasunaga, T. Kawamura, Y. Takahashi, Y. Hatori, N. Hamada, K. Fujiki, H. Yamazaki.
Int. J. PIXE, **20** (2010) 85-92.

[815] PIXE study on arsenic accumulation by a fern (pteris vittata)
H. Yamazaki, K. Ishii, S. Matsuyama, Y. Kikuchi, Y. Kawamura, K. Fujiki, Y. Hatori, N. Hamada, Y. Itoh, A. Fukaya, S. Hiraishi, Y. Miura, M. Hatayama, C. Inoue.
Int. J. PIXE, **20** (2010) 109-118.

[816] Search for a permanent EDM using laser cooled radioactive atom.
Y. Sakemi, K. Harada, T. Hayamizu, M. Itoh, H. Kawamura, S. Liu, H.S. Nataraj, A. Oikawa, M. Saito, T. Sato, H.P. Yoshida, T. Aoki, A. Hatakeyama, T. Murakami, K. Imai, K. Hatanaka, Y. Shimizu, U. Uchida.
J. Phys. Conf. Ser., **302** (2011) 012051.

[817] Search for the α condensed state in ^{16}O.
M. Itoh, T. Takahashi, T. Hayamizu, A. Oikawa, Y. Sakemi, H.P. Yoshida.
Modern Phys. Lett., **A 25** (2011) 1935.

[818] Radiation hardness of optoelectronic components for the optical readout of the ATLAS inner detector.
S. Hou, K. Ishii, M. Itoh, Y. Sakemi, D.S. Su, T.T. Su, P.K. Teng, H.P. Yoshida
Nucl. Instrum. Meth., **A636** (2011) S137-S142.

[819] Complete set of polarization transfer observables for the ^{16}O(p,n)^{16}F reaction at 296 MeV and 0 degrees.
T. Wakasa, M. Okamoto, M. Takaki, M. Dozono, K. Hatanaka, M. Ichimura, T. Noro, H. Okamura, Y. Sakemi
Phys. Rev., **C84** (2011) 014614.

[820] [*N*-methyl-^{11}C]Choline by on-column reaction: a study on [^{11}C]CH$_3$l incorporation and the residual amount of precursor in the product.
A. Bogni, O. Crispu, L. Fugazza, C. Cucchi, L. Laere, R. Iwata, F. Crippa, E. Bombardieri, C. Pascali.
J. Label. Compd. Radiopharm., **54** (2011) 157-162.

[821] Is the midbrain involved in the manifestation of gait disturbance in idiopathic normal-pressure hydrocephalus?
Kotaro Hiraoka, Hiroshi Yamasaki, Masahito Takagi, Makoto Saito, Yoshiyuki Nishio, Osamu Iizuka, Shigenori Kanno, Hirokazu Kikuchi, Etsuro Mori.
J. Neurol., **258** (2011) 820-825.

[822] A modified method of 3D-SSP analysis for amyloid PET imaging using [^{11}C]BF-227.
T. Kaneta, N. Okamura, S. Minoshima, K. Furukawa, M. Tashiro, S. Furumoto, R. Iwata, H. Fukuda, S. Takahashi, K. Yanai, Y. Kudo, H. Arai.
Ann. Nucl. Med., **25** (2011) 732-739.

[823] Brain histamine H1 receptor occupancy of loratadine measured by positron emission topography: comparison of H1 receptor occupancy and proportional impairment ratio.
N. Kubo, M. Senda, Y. Ohsumi, S. Sakamoto, K. Matsumoto, M.Tashiro, N. Okamura, K. Yanai.
Hum. Psychopharmacol., **26** (2011) 133-139.

[824] Positron emission tomography evaluation of sedative properties of antihistamines.
K. Yanai, D. Zhang, M. Tashiro, T. Yoshikawa, F. Naganuma, R. Harada, T. Nakamura, K. Shibuya, N. Okamura.
Expert Opin. Drug Saf., **10** (2011) 613-622.

[825] Neural basis of pleasant and unpleasant emotions induced by social reputation.
A. Ito, T. Fujii, A. Ueno, Y. Koseki, M. Tashiro, E. Mori.
Neuroreport, **22** (2011) 679-683.

[826] Cerebral metabolic changes in men after chiropractic spinal manipulation for neck pain.
M. Tashiro, T. Ogura, M. Masud, S. Watanuki, K. Shibuya, K. Yamaguchi, M. Itoh, H. Fukuda, K. Yanai.
Altern. Ther. Health Med., **17** (2011) 12-17.

[827] Digital pulse processing and electronic noise analysis for improving energy resolutions in planar TlBr detectors.
T. Tada, K. Hitomi, T. Tanaka, Y. Wu, S.-Y. Kim, H. Yamazaki, K. Ishii.
Nucl. Instrum. Methods in Phys. Res., **A638** (2011) 92-95.

[828] Fully automated production of iodine-124 using a vertical beam.
K. Nagatsu, M. Fukada, K. Minegishi, H. Suzuki, T. Fukumura, H. Yamazaki, K. Suzuki.
Appl. Radiat. Isot., **69** (2011) 146-157.

[829] K-Mean clustering algorithm for processing signals from compound semiconductor detectors.
T. Tada, K. Hitomi, Y. Wu, S.-Y. Kim, H. Yamazaki, K. Ishii.
Nucl. Instrum. Methods in Phys. Res., **A659** (2011) 242-246.

[830] Recent development of TlBr gamma-ray detectors.
K. Hitomi, T. Tada, S.-Y. Kim, Y. Wu, T. Tanaka, T. Shoji, H. Yamazaki, K. Ishii.
IEEE Trans. Nucl. Sci., **58** (2011) 1987-1991.

[831] Semiconductor detectors fabricated from TlBr crystals.
K. Hitomi, T. Tada, S.-Y. Kim, Y. Wu, H. Yamazaki, T. Shoji, K. Ishii.
Mater. Res. Soc. Symp. Proc., **1341** (2011) 111-117.

[832] Microbeam analysis of individual particles in indoor working environment.
S. Matsuyama, G. Catella, K. Ishii, A. Terakawa, Y. Kikuchi, Y. Kawamura, S. Ohkura, M. Fujikawa, N. Hamada, K. Fujiki, Y. Hatori, Y. Ito, H. Yamazaki, Y. Hashimoto, M. Zitnik, P. Pelicon, N. Grlj.
X-Ray Spect., **40** (2011) 172-175.

[833] In vivo 3D imaging of Drosophila melanogaster using PIXE-micron-CT.
S. Ohkura, K. Ishii, S. Matsuyama, A. Terakawa, Y. Kikuchi, T. Kawamura, G. Catella, Y. Hashimoto, M. Fujikawa, N. Hamada, K. Fujiki, Y. Hatori, H. Yamazaki.
X-Ray Spect., **40** (2011) 191-193.

[834] PIXE analysis of amurine solid tumor treated with proton therapy combined with cisplatin.

A. Terakawa, K. Ishii, H. Yamazaki, S. Matsuyama, Y. Kikuchi, Y. Ito, A. Tagawa, S. Yasunaga, T. Kawamura, Y. Takahashi, Y. Hatori, N. Hamada, N. Ito, S. Wada, Y. Funaki, K. Sera
X-Ray Spect., **40** (2011) 198-201.

[835] Adsorption characteristics for trivalent rare earths and chemical stability of a silica-based macroporous TODGA adsorbent in HNO_3 solution.
Y. Xu, Y. Wei, R. Liu, S. Usuda, K. Ishii, H. Yamazaki.
J. Nucl. Sci. Tech., **48** (2011) 1-7.

[836] Evaluation study on properties of a macroporous silica-based CMPO extraction resin to be used for minor actinides separation form high level liquid waste.
R. Liu, Y. Wei, D. Tozawa, Y. Xu, S. Usuda, H. Yamazaki, K. Ishii, Y. Sano, Y. Koma.
Nucl. Sci. Tech., **22** (2011) 18-24.

[837] A study on beam flattening based on compact double scatterer applicable to rotational beam irradiation system in the proton therapy facility at CYRIC, Tohoku University.
T.A. Esmaili, A. Terakawa, K. Ishii, H. Yamazaki, S. Matsuyama, Y. Kikuchii, H. Akiyama, K. Koyata, A. Tagawa, Y. Itoh, S. Yasunaga.
Prog. NUCL. Sci. Tech., **1** (2011) 509-512.

[838] Development of a new two-dimensional position-sensitive detection based on resistive charge division and using CdTe detectors for a high-resolution semiconductor-based PET scanning.
K. Ishii, Y. Kikuchi, K. Takahashi, K. Nakamura, S. Matsuyama, A. Terakawa, H. Yamazaki, K. Hitomi.
Nucl. Inst. Meth., **631** (2011) 138-143.

XI. MEMBERS OF COMMITTEE (as of Jan. 1, 2012)

General

(Chairman)	Keizo	Ishii	(Graduate School of Engineering)
	Toshio	Iijima	(Executive Vice President)
	Kazushige	Maeda	(Graduate School of Science)
	Kazuaki	Iwasa	(Graduate School of Science)
	Hozumi	Motohashi	(Graduate School of Medicine)
	Keiichi	Sasaki	(Graduate School of Dentistry)
	Noriyasu	Hirasawa	(Graduate School of Pharmaceutical Sciences)
	Akira	Hasegawa	(Graduate School of Engineering)
	Minoru	Satoh	(Graduate School of Agricultural Science)
	Kazuhiro	Sogawa	(Graduate School of Life Sciences)
	Atsuki	Terakawa	(Graduate School of Biomedical Engineering)
	Hiroaki	Abe	(Institute for Materials Research)
	Hiroshi	Fukuda	(Institute of Development, Aging and Cancer)
	Mihiro	Yanagihara	(Institute of Multidisciplinary Research for Advanced Materials)
	Shoki	Takahashi	(University Hospital)
	Hajime	Shimizu	(Research Center for Electron Photon Science)
	Ren	Iwata	(CYRIC)
	Hiromichi	Yamazaki	(CYRIC)
	Yasuhiro	Sakemi	(CYRIC)
	Tsutomu	Shinozuka	(CYRIC)
	Manabu	Tashiro	(CYRIC)
	Seong-Yun	Kim	(CYRIC)
	Keitaro	Hitomi	(CYRIC)

	Hirokazu	Tamura	(Graduate School of Science)
	Kazuhiko	Yanai	(Graduate School of Medicine)
	Tetsuya	Ono	(Radiation Safety Committee, Research Promotion Council)
	Michio	Niwano	(Radiation Safety Committee, Research Promotion Council)
(Observer)	Hideaki	Ishida	(Head of Administration Office, Graduate School of Information Science)

Cyclotron

(Chairman)	Yasuhiro	Sakemi	(CYRIC)
	Toshio	Kobayashi	(Graduate School of Science)
	Hirokazu	Tamura	(Graduate School of Science)
	Kazushige	Maeda	(Graduate School of Science)
	Kazuaki	Iwasa	(Graduate School of Science)
	Yasushi	Kino	(Graduate School of Science)
	Satoshi	Nakamura	(Graduate School of Science)
	Keizo	Ishii	(Graduate School of Engineering)
	Akira	Hasegawa	(Graduate School of Engineering)
	Atsuki	Terakawa	(Graduate School of Engineering)
	Yuki	Satoh	(Institute for Materials Research)
	Mihiro	Yanagihara	(Institute of Multidisciplinary Research for Advanced Materials)
	Tsutomu	Ohtsuki	(Research Center for Electron Photon Science)
	Ren	Iwata	(CYRIC)
	Hiromichi	Yamazaki	(CYRIC)
	Tsutomu	Shinozuka	(CYRIC)
	Manabu	Tashiro	(CYRIC)
	Takashi	Wakui	(CYRIC)
	Masatoshi	Itoh	(CYRIC)

Radiation Protection and Training of Safe Handling

(Chairman)	Hiromichi	Yamazaki	(CYRIC)
	Naohito	Iwasa	(Graduate School of Science)
	Yoshihiko	Uehara	(Graduate School of Medicine)
	Noriyasu	Hirasawa	(Graduate School of Pharmaceutical Sciences)
	Keizo	Ishii	(Graduate School of Engineering)
	Ikuo	Ikeda	(Graduate School of Agricultural Science)
	Kazumasa	Ohashi	(Graduate School of Life Sciences)
	Tatsuo	Shikama	(Institute for Materials Research)
	Akira	Hiraga	(Institute of Development, Aging and Cancer)
	Kentaro	Takanami	(University Hospital)
	Ren	Iwata	(CYRIC)
	Tsutomu	Shinozuka	(CYRIC)
	Manabu	Tashiro	(CYRIC)

Life Science

(Chairman)	Ren	Iwata	(CYRIC)
	Kazuhiko	Yanai	(Graduate School of Medicine)
	Haruo	Saito	(Graduate School of Medicine)
	Shoki	Takahashi	(Graduate School of Medicine)
	Hozumi	Motohashi	(Graduate School of Medicine)
	Shozo	Furumoto	(Graduate School of Medicine)
	Yukitsuka	Kudo	(Innovation of New Biomedical Engineering Center)
	Keiichi	Sasaki	(Graduate School of Dentistry)
	Masayuki	Seki	(Graduate School Pharmaceutical Sciences)
	Keizo	Ishii	(Graduate School of Engineering)
	Kazuhiko	Nishitani	(Graduate School of Life Science)

	Hiroshi	Fukuda	(Institute of Development, Aging and Cancer)
	Nariyasu	Mano	(University Hospital)
	Hiromichi	Yamazaki	(CYRIC)
	Manabu	Tashiro	(CYRIC)
	Yoshihito	Funaki	(CYRIC)

Prevention of Radiation Hazards

(Chairman)	Hiromichi	Yamazaki	(CYRIC)
	Naohito	Iwasa	(Graduate School of Science)
	Yasushi	Kino	(Graduate School of Science)
	Keizo	Ishii	(Graduate School of Engineering)
	Ren	Iwata	(CYRIC)
	Yasuhiro	Sakemi	(CYRIC)
	Tsutomu	Shinozuka	(CYRIC)
	Manabu	Tashiro	(CYRIC)
	Hideyuki	Yuki	(CYRIC)
	Katsuo	Aizawa	(CYRIC)

Research Program

(Chairman)	Hiromichi	Yamazaki	(CYRIC)
	Hirokazu	Tamura	(Graduate School of Science)
	Kazushige	Maeda	(Graduate School of Science)
	Kimiko	Sekiguchi	(Graduate School of Science)
	Kazuhiko	Yanai	(Graduate School of Medicine)
	Shin	Fukudo	(Graduate School of Medicine)
	Akira	Hasegawa	(Graduate School of Engineering)
	Atsuki	Terakawa	(Graduate School of Engineering)
	Akira	Takahashi	(Graduate School of Medicine)
	Yuki	Satoh	(Institute for Materials Research)
	Hiroshi	Fukuda	(Institute of Development, Aging and Cancer)

	Shoki	Takahashi	(University Hospital)
	Hajime	Shimizu	(Research Center for Electron Photon Science)
	Tsutomu	Ohtsuki	(Research Center for Electron Photon Science)
	Tsutomu	Sekine	(Center for the Advancement of Higher Education)
	Ren	Iwata	(CYRIC)
	Yasuhiro	Sakemi	(CYRIC)
	Tsutomu	Shinozuka	(CYRIC)
	Manabu	Tashiro	(CYRIC)
(Observer)	Takashi	Wakui	(CYRIC
(Observer)	Masatoshi	Itoh	(CYRIC)

XII. STAFF (as of Jan. 1, 2012)

Director Keizo Ishii

Division of Accelerator

Osamu Hashimoto[1]
Tsutomu Shinozuka
Takashi Wakui
Kenji Shimada
Yasuaki Ohmiya[7]
Naoto Takahashi[7]
Jyunya Suzuki[7]
Ken Takahashi[7]

Division of Instrumentations

Yasuhiro Sakemi
Hirokazu Tamura[1]
Hikonojo Orihara[5]
Atsuki Terakawa[3]
Masatoshi Itoh
Kenichi Harada
Hirokazu Kawamura
Hidetomo Yoshida
Huliyar Nataraj
Shingo Hiraishi
Kenichi Shinbo[9]
Tadanobu Toba[9]

Division of Radiopharmaceutical Chemistry

Ren Iwata
Yukitsuka Kudo[4]

Kazutoshi Suzuki5)
Kiichi Ishiwata5)
Shozo Furumoto2)
Yoshihito Funaki
Yoichi Ishikawa

Division of Cyclotron Nuclear Medicine

Kazuhiko Yanai2)
Masatoshi Itoh6)
Keiichiro Yamaguchi5)
Koichiro Kawashima5)
Kazuo Kubota5)
Manabu Tashiro
Miho Shidahara
Kotaro Hiraoka
Shoichi Watanuki
Xuclong Duan
Takeshi Ogura
Mehedi Masud
Kazuko Takeda

Division of Radiation Protection and Safety Control

Hiromichi Yamazaki
Takashi Nakamura5)
Masayuki Hasegawa5)
Mamoru Baba5)
Haruaki Tokuda
Hideyuki Yuki
Kazuhiro Ohtomo
Hirokazu Nakae8)

Division of Nuclear Fuel Science

Etsushu	Kuraoka
Seong-Yun	kim
Yuanlai	Xu

Division of Advanced Radiation Application

Keitaro	Hitomi
Tsutomu	Tada
Masayasu	Miyake
Fujie	Hitomi

Graduate Student and Researcher

Hiroto	Ueno	(Graduate School of Science)
Manami	Takahashi	(Graduate School of Science)
Akihito	Oikawa	(Graduate School of Science)
Tomohiro	Hayamizu	(Graduate School of Science)
Tomoya	Sato	(Graduate School of Science)
Tomohiro	Kato	(Graduate School of Science)
Wong	Rebecca	(Graduate School Pharmaceutical Sciences)
Takeumi	Kawauchi	(Graduate School Pharmaceutical Sciences)
Hiroaki	Itoh	(Graduate School Pharmaceutical Sciences)
Tetsuro	Tago	(Graduate School Pharmaceutical Sciences)
Yuichi	Ito	(Graduate School Pharmaceutical Sciences)
Akihiro	Sugawara	(Graduate School, Division of Medicine)
Akie	Inami	(Graduate School, Division of Medicine)
Tatsuya	Ito	(Graduate School of Engineering)
Seigo	Sato	(Graduate School of Engineering)
Atsuo	Fukaya	(Graduate School of Engineering)
Hiroto	Kawano	(Graduate School of Engineering)
Takahiro	Sasaki	(Graduate School of Engineering)
Kasane	Nakazawa	(Graduate School of Engineering)
Satoshi	Hasegawa	(Graduate School of Engineering)

Office Staff

Hideaki	Ishida
Katsuo	Aizawa
Namiko	Ito
Satoshi	Arao
Kyoko	Fujisawa
Fumiko	Mayama
Chihiro	Saeki
Asami	Sawada
Yukie	Minbuta
Yoshio	Muroi
Kei	Ito
Miki	Yashima
Katsuo	Ibuka
Yuko	Yamashita

1) Graduate School of Science
2) Graduate School of Medicine
3) Graduate School of Engineering
(Graduate School of Biomedical Engineering)
4) Innovation of New Biomedical Engineering Center
5) Visiting Professor
6) Specially-approved visiting professor
7) SUMI-JU Accelerator Service Ltd.
8) Japan Radiation Protection Co., Ltd.
9) Cooperative researcher